Polarization Independent Microphotonic Circuits

by

Michael Robert Watts

Submitted to the Department of Electrical Engineering and Computer Science
in partial fulfillment of the requirements for the degree of

Doctor of Philosophy in Electrical Engineering

at the

MASSACHUSETTS INSTITUTE OF TECHNOLOGY

June 2005

Author .....
Department of Electrical Engineering and Computer Science
May 20, 2005

Certified by .....
Erich P. Ippen
Elihu Thomson Professor of Electrical Engineering
Thesis Supervisor

Certified by .....
Hermann A. Haus
Institute Professor
Thesis Supervisor

Accepted by .....
Arthur C. Smith
Chairman, Department Committee on Graduate Students

[This Page was Intentionally Left Blank]

Polarization Independent Microphotonic Circuits

by

Michael Robert Watts

Submitted to the Department of Electrical Engineering and Computer Science
on May 20, 2005, in partial fulfillment of the
requirements for the degree of
Doctor of Philosophy in Electrical Engineering

Abstract

Microphotonic circuits have been proposed for applications ranging from optical switching and routing to optical logic circuits. However many applications require microphotonic circuits to be polarization independent, a requirement that is difficult to achieve with the high index contrast waveguides needed to form microphotonic devices. Chief among these microphotonic circuits is the optical add/drop multiplexer which requires polarization independence to mate to the standard single-mode fiber forming today's optical networks.

Herein, we present the results of an effort to circumvent the polarization dependence of a microphotonic add/drop multiplexer with an integrated polarization diversity scheme. Rather than attempt to overcome the polarization dependence of the microphotonic devices in the circuit directly, the arbitrary polarization emanating from the fiber is split into orthogonal components, one of which is rotated to enable a single on-chip polarization. The outputs are passed through identical sets of devices and recombined at the output through the reverse process. While at the time of this publication the full polarization diversity scheme has yet to be implemented, the sub-components have demonstrated best-in-class performance, leaving integration as the remaining task. We present the results of a significant effort to design integrated polarization rotators, splitters, and splitter-rotators needed to implement the integrated polarization diversity scheme. Rigorous electromagnetic simulations were used to design these devices along with the microring-resonator based filters used to form the optical add/drop multiplexer microphotonic circuit. These device designs were passed onto fabrication, and the fabricated devices were characterized and the results compared to theoretical predictions. The integrated polarization rotators and splitters demonstrated broadband, low loss, and low cross-talk performance while the integrated polarization splitter-rotators demonstrated equally impressive performance and represent the first demonstrations of a device of this kind. Similarly impressive performance was exhibited by the microring-resonator filters which achieved the deepest through port extinction and largest free-spectral-range of a functioning high order microring-resonator filter.

Thesis Supervisor: Erich P. Ippen
Title: Elihu Thomson Professor of Electrical Engineering

Thesis Supervisor: Hermann A. Haus
Title: Institute Professor

Preface and Acknowledgments

Attaining a PhD in science or engineering, is a singular experience. While all other degrees certify completion by finishing coursework, the PhD requires, through extensive research, the demonstration and often realization of a new concept, device, or system. While intense cousework is also required, the main challenge is maintaining focus in the realm of great uncertainty with an end goal many years away. For me, the learning has been as much about myself as about my field of interest.

I have been fortunate enough to be able to pursue my Ph.D. at the Massachusetts Institute of Technology, a place of great distinction that both encourages and inspires creative thinking. With the support of my advisors, professors Hermann Haus and Erich Ippen, along with some unofficial advisors, professors Franz Kaertner, Henry Smith, Rajeev Ram, and Lionel Kimerling, I have been given the freedom to develop concepts that were initially only faint outlines into working prototypes. Despite the many challenging proposals that I have made, in my years at MIT, I was never told my ideas were too difficult or expensive to realize. Prof. Haus, Prof. Ippen and Prof. Kaertner were always encouraging and Prof. Smith never seemed to fear fabricating a complex structure. When I think of the Massachusetts Institute of Technology, these individuals are what come to mind. It was their support and encouragement that enabled my success as a student.

One of the amazing resources of MIT is its students. I was fortunate enough to be involved in a team project that enabled substantial interaction among some very qualified students. Ideas that I generated were later realized with the help of Minghao Qi and Tymon Barwicz, two of Prof. Smith's students that made the fabrication of complicated structures appear relatively simple. Without their help, my work would have only resulted in paper studies, that while rigorous, would be far less convincing than the working prototypes. And the contributions of these students mark only a portion of the expertise so readily available. I am indebted to both Christina Manolatou and Milos Popovic for code development and Peter Rakich for his measurement expertise.

I am grateful to Pirelli Labs for supporting my doctoral research and to Draper Laboratory for the support they gave me as a master's student. Without these two organizations I would not have been able to pursue my studies at MIT. In particular, I would like to thank Marco Romagnoli for having faith in my ideas that so clearly bucked the industry trend, and Luciano Socci for maintaining a smooth Boston-Milan connection.

To
Charles Dirk, Jacques Govignon, and Hermann Haus

Contents

List of Figures

Chapter 1

Introduction

Over the course of my studies at MIT, the photonics industry has experienced rapid growth, and in the wake of the "Dot-Com Bubble", dramatic decline. During the rapid expansion I witnessed several colleagues of mine start companies with initial rounds of venture funding in the several to tens of millions of dollars. Most of these companies, like most other photonics start-ups during the boom, have since failed with the industry collapse. While the collapse resulted in large measure because the perceived market did not exist, there was also perhaps a more fundamental problem. Most considered the photonics industry to be in a state similar to the electronics industry at the time of the development of the transistor. And while strong parallels exist, in some respects photonics is at an even earlier stage in its development. Soon after the development of the transistor, circuits with tens and even hundreds of transistors were integrated together. And, only a few decades later millions of transistors were integrated in DRAM and microprocessors. In contrast, photonics has yet to even arrive at a common material system. Lasers are made in III-V materials while passive components are made in amorphous dielectrics and crystalline silicon. And, while microphotonic devices and large scale integration have been proposed [1], decades after the first demonstration of a photonic circuit, few circuits have been demonstrated with more than ten integrated optical subcomponents.

The reason behind this extraordinarily slow growth in photonic circuit complexity appears to be that photonics systems are inherently more challenging and complex than their electronic counterparts. In addition to the exotic materials required to efficiently generate and detect light, the tolerances required to make simple passive microphotonic components

are orders of magnitude more stringent than those found in the most demanding electronic applications. It is not uncommon for applications to require dimensions to be controlled to ten parts in a million. As a result, the smaller the device, the more challenging meeting these requirements becomes. Overcoming these challenges is a matter of detailed engineering and process control. To enable large scale integration with the so many varied optical devices required for useful functionality, it is important to develop solutions that are maximally tolerant.

While in the future microphotonic systems will likely have many varied applications, currently, optical communications represent the dominant application of this technology. Since optical networks use single-mode fiber that does not maintain polarization, components in the network must maintain polarization independent performance. Achieving polarization independence in microphotonic devices, while possible, is exceedingly challenging because microphotonic devices require the use of high index contrast waveguides which are innately sensitive to polarization both in propagation and coupling. As a result, one of the factors limiting the adoption of microphotonic circuits is the industry-wide insistence on polarization independence at the device level. Yet, it is only necessary that polarization independence be maintained at the component or chip level. Several years ago, myself and my advisor Hermann Haus decided that the only way microphotonic systems could be employed in polarization independent communication systems was to circumvent their innate polarization sensitivities. Rather than attempt to overcome the polarization dependence of the microphotonic devices in the circuit directly, we proposed splitting the arbitrary polarization emanating from the fiber into orthogonal components, and subsequently rotating one of the outputs to enable a single on-chip polarization. The outputs are passed through identical sets of devices and recombined at the output through the reverse process (Fig. 1-1). Such an approach is referred to as a polarization diversity scheme [2, 3]. What is unique about our approach is the suggestion of performing all of the functionality on-chip. The reason for doing so extends beyond the simple idea of achieving dense integration. The path lengths of the two arms of the polarization diversity scheme must be matched to a small fraction of a bit period to avoid the effects of inter-symbol interference. With the ever increasing bit rates of optical communication systems, the requirement for matching path lengths becomes fairly stringent. At 40 GB/s, matching path lengths to 1/20 of a bit period in an optical fiber corresponds to $\sim 250\,\mu$m, an achievable, but by no means easy

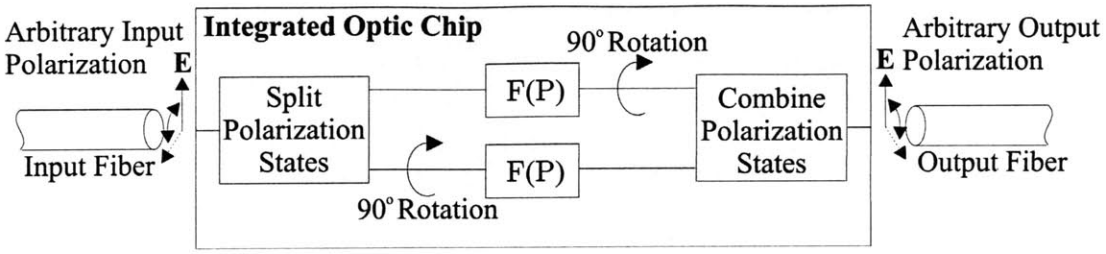

Figure 1-1: Approach for achieving chip-level polarization independence with polarization dependent devices. Here, F(P) represents a device which generally has a polarization P dependent response.

task with bulk components.

While this approach has wide-ranging applications, the microphotonic system for which this approach was developed is a reconfigurable optical add/drop multiplexer (R-OADM). In this chapter, we aim to provide a motivation using R-OADMs in optical networks, the advantages of using microphotonic circuits to form an R-OADM, outline our approach for doing so, and demonstrate the need for the polarization diversity scheme just described to achieve chip-level polarization independence.

1.1 Optical Networks

Optical transmission systems have demonstrated remarkable progress over the quarter century since their inception. Initial systems carried only a single signal per fiber and required the use of electrical regenerators to restore signal fidelity. With only a single optical signal, the bandwidth of initial systems was limited to the electrical bandwidths of the signal generation and detection systems. Optical transmission systems remained in this state until the advent of the erbium fiber amplifier [4], which enabled optical signals to be amplified in the optical domain, allowing many signals of different carrier frequency to traverse a fiber simultaneously in wavelength division multiplexed (WDM) transmission systems. In contrast to regenerator-based systems which required the signals to be separated, detected, and regenerated independently roughly every 25 km, by amplifying in the optical domain all signals could be amplified in parallel making WDM systems economical. As a result, WDM systems have been so successful that multi-terabit long distance transmission systems [5] are now possible, more than enough bandwidth to carry all the voice and data traffic in the

US on a single fiber at the time of this publication.

Yet, while optical transmission systems have made the transition from electrical regenerators to optical amplifiers, optical networks lag behind. At the end of a fiber link, signals are demultiplexed and converted into the electrical domain. The electrical signals are processed, and for signals continuing to a new destination, converted back to the optical domain for transmission down another fiber link. Here again, as many lasers, modulators, and detectors as signals on the fiber are required to regenerate the optical signals. Since long-haul transmission systems have only a small number of termination points or nodes, they are only weakly impacted by the complexity of the node. However, metro-networks require a large number of interconnections and the cost of each interconnection greatly impacts the cost of the network. A strong parallel exists between the development of the optical amplifier for the long-haul transmission system and optical switches on the metro-network. If the signals could be switched in the optical domain, the complexity of the node could be reduced considerably. It is therefore reasonable to suggest that optical switches will impact the network in much the same way as the optical amplifier impacted transmission systems.

Microphotonic systems will likely provide some of the solutions for implementing these optical switches. Our research has been focussed on implementing a particular type of optical switch, a device that is commonly referred to as a reconfigurable optical add / drop multiplexer (R-OADM). The R-OADM is a switch which allows for selectively adding and/or dropping one or more channels without affecting the other signals on the fiber. The importance of a R-OADM becomes immediately apparent by considering a simple ring network. In a ring network, nodes communicate along wavelength based routes. A simple ring network is considered in Fig. 1-2, where λ_m^n refers to a signal transmitted from Node n with wavelength m. In the figure, Node 1 communicates to Node 3 via wavelength 1 while Node 2 communicates to Node 4 via wavelength 2. If the OADMs are reconfigurable, Node 1 can communicate to Node 2, by setting its OADM to add and drop wavelength 1 while Node 3 sets its OADM to add and drop wavelength 2. In this manner addressing and communicating between nodes becomes relatively straightforward and can be achieved without the costly conversion from the optical to electrical domains.

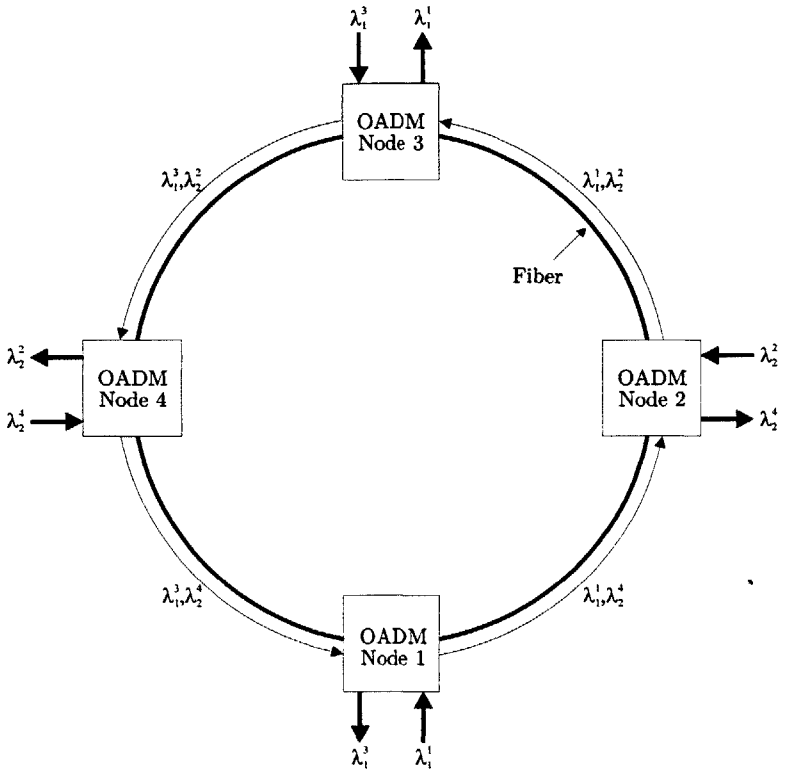

Figure 1-2: A basic ring network architecture utilizing OADMs. R-OADMs enable the addressing of nodes in the ring via wavelength channels.

1.2 Implementing an R-OADM with Resonators

R-OADMs formed from arrayed waveguide gratings (AWGs) are commercially available [6]. However, these devices occupy massive chip areas ($> 10\,\mathrm{cm}^2$) and tend to demonstrate rather poor performance. As a result, they are both expensive and of limited utility. This is in large measure because AWGs first demultiplex all of the channels, switch out the desired channel, and then multiplex all of the signals back onto the transmission system. Each multiplex and demultiplex operation introduces substantial loss making AWG-based R-OADMs a very lossy component to introduce into a network.

It would be highly preferable to operate only on the channel of interest. Resonant structures do just that by offering a natural ability to add/drop a single channel. For this reason, in this project we consider using optical resonators to form an OADM. Much work has previously been done, both in our group, and others on both standing- [7, 8] and traveling-wave resonators [9, 10]. To justify our choice of device, we briefly digress into the

advantages and disadvantages of each type.

Standing-wave resonators generally consist of a pair of imperfect mirror-like structures separated by some distance L (Fig. 1-3). Incident radiation is partially transmitted into the structure do to the incomplete reflection of the mirror facets. The resonance condition for a standing-wave resonator is given by (1.1)

$$2kL + \phi_{M_T} = 2\pi m \tag{1.1}$$

where k is the wavenumber, ϕ_{M_T} is the phase change induced by the mirrors, and m is an integer. The wavenumber can be re-expressed in terms of the wavelength λ [1] and refractive index n (i.e. $k = 2\pi n/\lambda$) to provide an expression for the resonant wavelength λ_m (1.2).

$$\lambda_m = \frac{2Ln}{m - \phi_{M_T}/2\pi} \tag{1.2}$$

When the mirrors do not induce a phase change (i.e. $\phi_{M_T} = 0$), resonance occurs when the cavity length is set to integer multiples of the half wavelength in the medium (i.e. $L = m\lambda/2n$).

Traveling wave resonators obey a condition similar to (1.1) with the exception that the length is not multiplied by 2 since the field propagates around the structure only once (Fig. 1-4). The condition is given by (1.3)

$$kL + \phi_{M_T} = 2\pi m \tag{1.3}$$

with the corresponding expression (1.4) for the resonant wavelength indicating that resonance

$$\lambda_m = \frac{Ln}{m - \phi_{M_T}/2\pi} \tag{1.4}$$

in a traveling wave resonator occurs for integer multiples of a full wavelength in the material (i.e. $L = m\lambda/n$). The resonant frequencies ν_m may be obtained by simply dividing the speed of light c by (1.2) and (1.4) to obtain the standing- and traveling-wave resonant frequencies, respectively.

Standing-wave resonators are especially convenient when implemented in bulk devices.

[1] In this document λ always refers to the vacuum wavelength

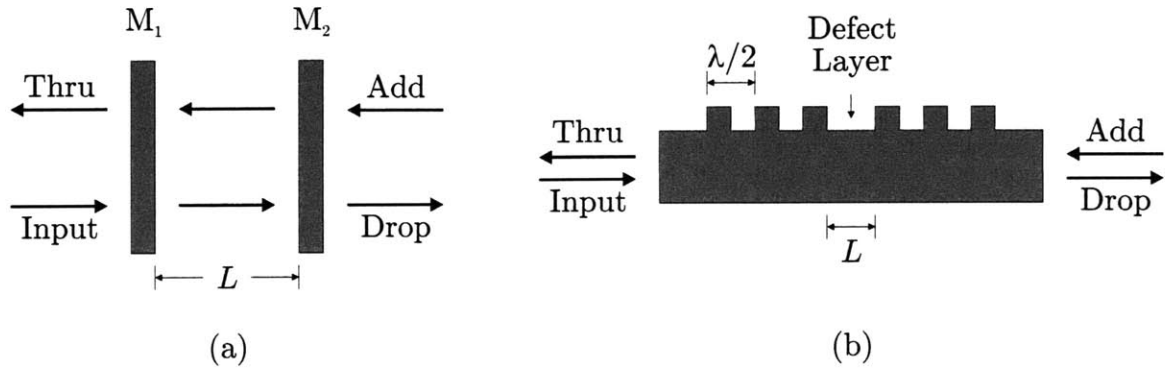

Figure 1-3: (a) Bulk and (b) integrated standing-wave resonators.

Thin film filters are constructed this way and currently dominate the passive filter market. The layer thickness of a thin film device is easy to control and the input and output ports can be easily separated by using a non-normal angle of incidence. However, high quality standing-wave resonators are difficult to construct in integrated form and the input and output ports are not so easily separated as a result of the finite extent of the mode and resulting diffraction. And, although theoretical designs exist that do not radiate [7] (see also Appendix A), most integrated standing-wave resonators suffer from radiation associated with imperfect mode-matching between the layer pairs.

Traveling-wave resonators are cumbersome in bulk form. The most notable practical example is the ring laser gyroscope. However, integrated traveling-wave resonators are relatively easy to construct and offer a natural separation of ports. An isolated resonator is constructed by simply wrapping the waveguide around and closing it upon itself to form a closed loop. Coupling to the resonator is then achieved through evanescent fields by bringing bus waveguides into proximity with the loop. Typically these resonators are formed by simple rings and many examples exist in the literature [9, 10, 1]. Ring-resonators are limited by bend induced radiation. Larger radius rings exhibit higher internal Q's. This places a limit on the separation between resonance orders commonly referred to as the free-spectral-range (FSR) (1.5) that may be achieved with a ring.

$$\mathrm{FSR} = \frac{c}{2\pi R n_g} \tag{1.5}$$

In a network, such as the ring network depicted in Fig. 1-2, the FSR of the OADM

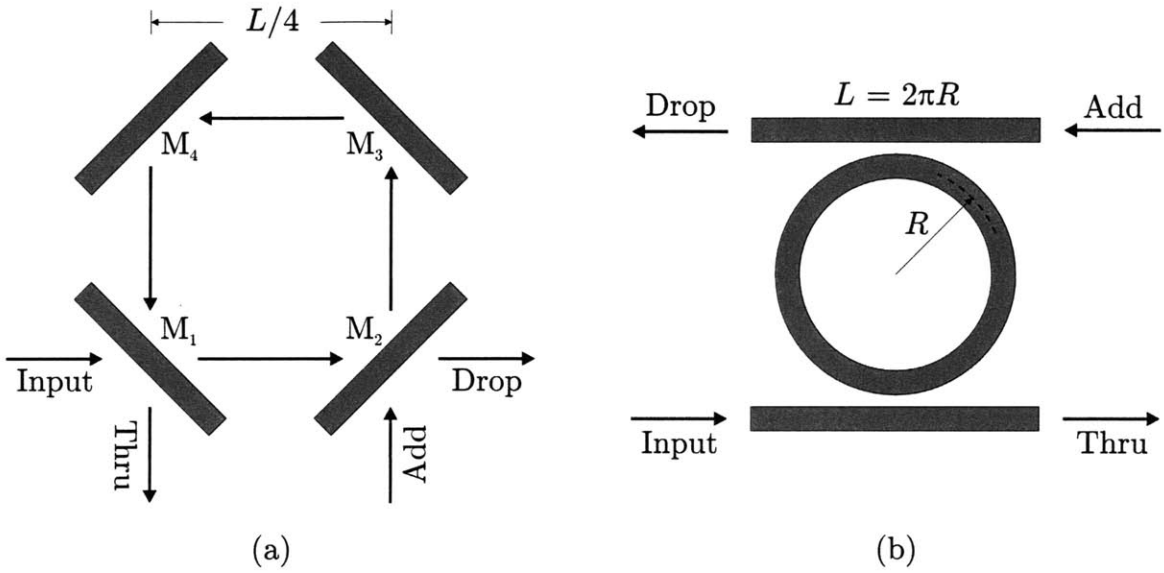

Figure 1-4: (a) Bulk and (b) integrated traveling-wave resonators.

module places a bandwidth limitation on the network. An attempt to use bandwidth beyond the OADM module would result in the inadvertent adding / dropping of aliased channels. This limitation demonstrates the importance of using small resonators, as the size of the resonator directly impacts the usable bandwidth of the network. So while the commonly suggested reason for the need for microphotonic devices is dense integration, the functionality enabled by microphotonic components, is often a more compelling reason. In addition to the large resonator FSRs enabled by the small device dimensions, as will be discussed in Chapter 6, evanescent and thermal tuning mechanisms are possible in micro-systems that are not realistically achievable in bulk systems.

1.3 Polarization Sensitivity of Microring-Resonators

Ring resonators are a particularly simple and convenient resonator implementation that are relatively easily fabricated and provide a natural separation between the input and output ports. The one limitation of the ring-resonator is its FSR which is determined by the ring radius. Unlike standing-wave resonators, the modes in ring-resonators must radiate or the phase fronts of the modes would at some radial distance from the center of the ring propagate at greater than the speed of light c. Thus, the FSR of the ring is ultimately limited by

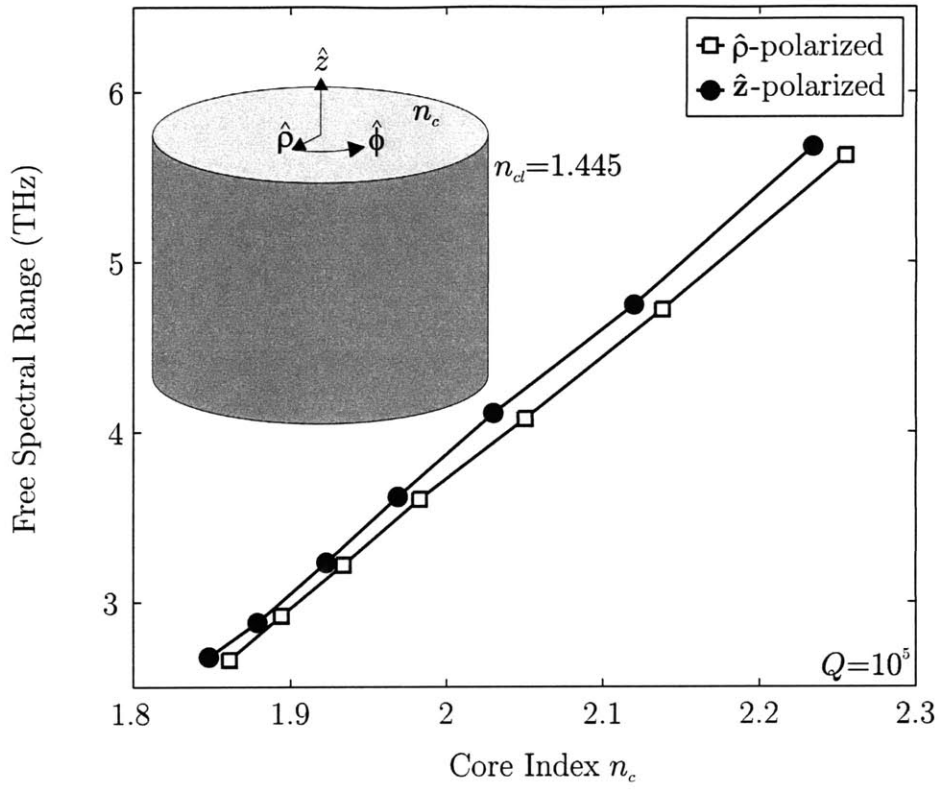

Figure 1-5: The FSR for the $\hat{\rho}$ and $\hat{z}$ polarized whispering gallery modes of a cylinder as a function of core index with the radius adjusted to maintain a constant Q of 10^5. The background index is set to that of silica (1.445).

how well the ring-mode is confined. The more highly confined, the less the evanescent field extends into the radiation zone. A cylindrical modesolver [11] is used to solve for the one-dimensional $\hat{\phi}$-propagating whispering gallery modes of a cylinder to illustrate this point. The FSR as a function of the core index n_c using a cladding index $n_{cl} = 1.445$ is plotted in Fig. 1-5 for both $\hat{\rho}$ and $\hat{z}$ polarized modes, where the radius of the cylinder was adjusted to maintain a constant Q of 10^5. The figure demonstrates a linear relationship between index contrast and FSR. A typical requirement for an OADM is for its FSR to cover the C-band (4.5 THz). To achieve a FSR of 4.5 THz, Fig. 1-5 indicates that a core index of ~ 2.1 is required.

The silicon nitride material system enables indices in the $2 - 2.2$ index range and is compatible with a silica cladding ($n = 1.445$). So, appropriate materials are available. However, use of such a high index contrast increases the polarization sensitivity of the structure. Both the propagation of the mode and coupling between waveguides becomes

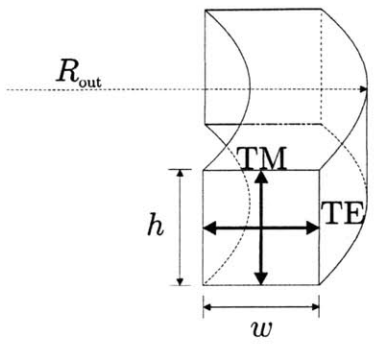

Figure 1-6: Diagram of a square waveguide bent to form ring. The polarization sensitivity of the resonant frequency of a microring resonator formed from a square waveguide with $h = 0.6\,\mu$m, $w = 0.6\,\mu$m, $R_{\text{out}} = 8\,\mu$m, $n_c = 2.2$, and $n_{cl} = 1.445$ is 20 GHz per nanometer change in the waveguide height h. The tolerance in the alignment of the TE and TM filter functions for a typical OADM application is ~ 1 GHz.

polarization dependent as the index contrast is increased. The effect is a result of Gauss' Law for dielectrics ($\nabla \cdot \mathbf{E} = 0$) which imposes different boundary conditions for the two polarizations. A square waveguide bent to form a three-dimensional ring is depicted in Fig. 1-6 to illustrate the effect on propagation. We consider a case with $h = 0.6\mu$m, $w = 0.6\mu$m, $R_{\text{out}} = 8\mu$m, $n_c = 2.2$, and $n_{cl} = 1.445$. The waveguide is symmetric, and so one might expect the modes to be degenerate, however, the bend in the guide breaks the symmetry and degeneracy of the modes. The degeneracy may be restored by a slight adjustment of the guide width or height. However, by varying height of the ring, we determine that the change in the resonant frequencies of the transverse electric (TE) and transverse magnetic (TM) modes due to a change in the layer thickness is $df_{\text{TE}-\text{TM}}/dh = 20\,\text{GHz} / \text{nm}$. Thus, for the resonant frequencies of the orthogonally polarized ring modes to be matched ~ 1 GHz, the layer thickness must be controlled to better than 1 Å across the wafer, a tolerance that is not readily achievable with any current fabrication technology.

Although microring-resonators are innately polarization sensitive, they are relatively easy to fabricate, offer a natural separation of ports, and can be densely integrated. Moreover, coupled microring-resonator filters have demonstrated box-like filter responses [10, 9]. And while we highlighted the polarization sensitivity of microrings, polarization dependent operation is not limited to the microring as all microphotonic devices that utilize strong vertical and/or lateral confinement of the optical mode tend to be polarization sensitive. The importance of using a polarization diversity scheme like the one depicted in Fig. 1-1,

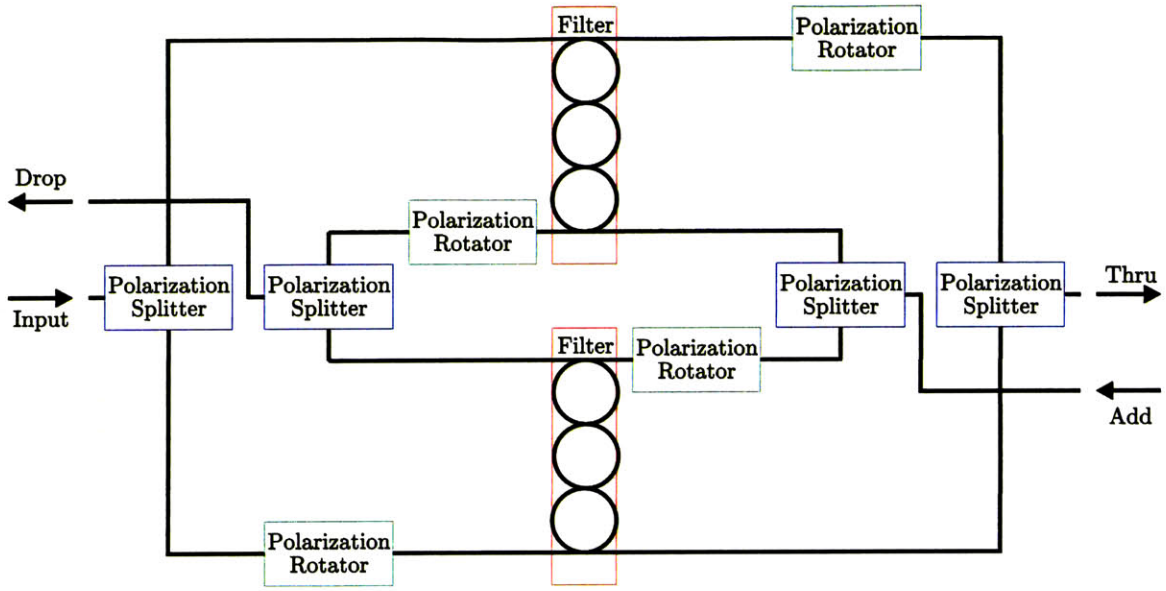

Figure 1-7: The OADM microphotonic circuit used to circumvent the polarization sensitivities of the microring-resonator-based filters to achieve chip-level polarization independene.

should now be clear. Microphotonic devices, such as microring-resonators which enable large scale integration and functionality not possible with bulk systems, cannot be reliably fabricated in a way that enables polarization independence at the device level. Therefore, to implement our OADM, we have chosen microring-resonators to form the filters, and an integrated polarization diversity scheme to circumvent their innate polarization sensitivities. A diagram of the circuit is depicted in Fig. 1-7.

1.4 Summary

Microphotonic circuits offer distinct advantages over bulk and large low index contrast devices. Yet, the progress in microphotonic circuits has been slow in part because of the industry-wide insistence of achieving polarization independence at the device level. As a result of this muted progress, optical networks are in a primitive state with switching and routing generally occurring in the electrical domain and thus requiring a full demultiplex of the optical signals. Microphotonic circuits have the potential to alter this landscape and impact optical networks in much the same way as the erbium fiber impacted optical transmission systems, but doing so requires circumventing the polarization sensitivities of

microphotonic devices.

The development of a polarization independent microphotonic circuit is the focus of this thesis. Rigorous electromagnetic simulations were used to design each of the components (i.e. polarization rotators, polarization splitters, polarization splitter-rotators, and microring-resonator based filters) in the microphotonic circuit of Fig. 1-7. Polarization rotators are the subject of Chapter 2, polarization splitters the subject of Chapter 3, and the fabrication and measurement results of each of these devices and the integrated polarization splitter-rotator, the subject of Chapter 4. In Chapter 5, microring resonator based filter designs are introduced and experimental results presented. In Chapter 6, we conclude by presenting the design for the full OADM microphotonic circuit and present some initial thoughts for reconfiguring the OADM.

Chapter 2

Integrated Polarization Rotators

The development of an integrated polarization diversity scheme began by considering the challenge of rotating polarization states on-chip. Initially, I considered the task of rotating polarization states from a coupled-mode perspective. However, inducing polarization rotation through mode-coupling mechanisms is no easy task. It requires coupling modes with orthogonal principal states of polarization. Coupling must therefore occur through minor field components. Still, several methods for doing so have been proposed [12, 13, 14, 3]. And, a relatively straightforward approach of doing so by coupling orthogonally oriented rectangular waveguides was considered in detail [3]. While the performance of the approach was verified through finite-difference time-domain (FDTD) simulations, the simulations also revealed the innate wavelength dependence of the approach and its inherent fabrication sensitivities. Moreover, these limitations exist in any coupled-mode approach. For complete power transfer, the coupled modes must be phase-matched, and the degree of coupling precisely tuned to the structure length. Since both propagation rate and coupling strength are inherently sensitive to guide dimensions and wavelength, coupled-mode approaches are fabrication intolerant and wavelength sensitive.

Despite the sensitivities of the coupled-mode approaches, without another method for inducing polarization rotation on-chip, fabrication of the coupled orthogonally oriented waveguides was ready to proceed. It was only a suggestion by Hermann Haus that re-directed this effort. He suggested the use of chirality for inducing polarization rotation. While he was referring to chiral materials, it was this critical suggestion that brought on a discussion of using "chiral-like" structures. Structurally chiral waveguides are mode-evolution-based

devices that adiabatically rotate the polarization state of the guided modes. Structures relying on mode-evolution only require mode-coupling be inhibited, a far looser requirement than ensuring it. In this chapter, we demonstrate through rigorous electromagnetic simulations, that relatively short devices of this type can yield broadband low-loss conversion of polarization states with good extinction. While much of this work has been published elsewhere [15, 16, 17, 18], here a more comprehensive discussion is presented.

2.1 Mode-Evolution

In bulk form, a series of waveplates can be stacked together with a slow rotation of the optical axis from plate-to-plate to induce a rotation of the polarization state. In a waveguide, the same effect can be ensured through a twisting or corkscrew-like perturbation (Fig. 2-1). However, such a twisting of the structure causes the modes to both evolve and couple. The

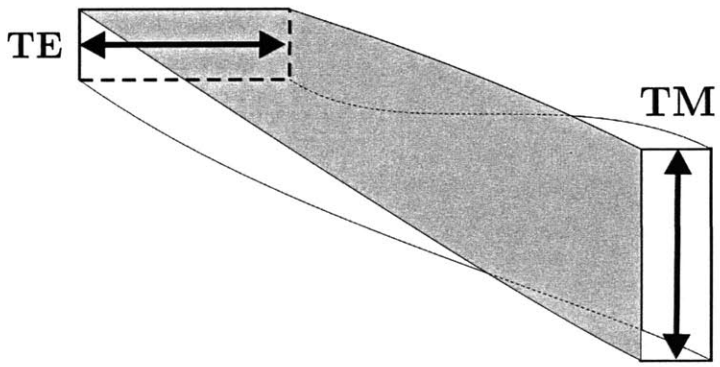

Figure 2-1: A twisted birefringent waveguide. The large aspect ratio causes the guide to be birefringent thereby inhibiting coupling between the TE and TM guided modes and allowing the polarization state to be conserved in spite of the coupling induced by the twist.

coupling limits the device performance. To understand the limitations imposed by the coupling and how best to minimize its impact, it is necessary to consider mode-evolution from an analytical perspective. Since the mode set changes at each cross-section, the evolution of the mode amplitudes $b_m(z)$ is best described by the coupled-local-mode equations [19]

$$\frac{db_m(z)}{dz} + j\beta_m(z)b_m(z) = \sum_n \kappa_{mn}(z)b_n(z) \tag{2.1}$$

where $\beta_m(z)$ is the local propagation constant of mode m, $\kappa_{mn}(z)$ is the local coupling coefficient between modes m and n given by

$$\kappa_{mn}(z) = \frac{\omega}{4\delta\beta(z)} \int_A \mathbf{e}_m^*(x,y,z) \cdot \mathbf{e}_n(x,y,z) \frac{d}{dz}\varepsilon(z) dA, \tag{2.2}$$

$\delta\beta(z) = \beta_m(z) - \beta_n(z)$, and $\mathbf{e}_m, \mathbf{e}_n$ are the normalized modal vector electric field distributions for modes m and n, respectively. In the limit of weak coupling, the terms $\sum_{m \neq n} \kappa_{mn} b_n$ in (2.1) where mode n is the initially excited mode may be dropped as they are necessarily small. The amplitude of mode m is then

$$b_m(z) = b_n(0) e^{-j\int_0^z \beta_m(z')dz'} \int_0^z \kappa_{mn}(z') e^{-j\overline{\delta\beta}(z)z'} dz' \tag{2.3}$$

where $\overline{\delta\beta}(z) = \frac{1}{z}\int_0^z [\beta_n(z') - \beta_m(z')]\, dz'$ is the average difference between the propagation constants. In evolving structures, the coupling coefficient varies slowly and may be replaced by its average and taken out of the integral in (2.3). The power P_m accumulated in mode m is then

$$P_m(z) = 2\,|b_n(0)|^2 \left|\frac{\bar{\kappa}}{\overline{\delta\beta}}\right|^2 \left[1 - \cos(\overline{\delta\beta} z)\right] \tag{2.4}$$

where $\bar{\kappa}(z) = \frac{1}{z}\int_0^z \kappa_{mn}(z')dz'$. According to (2.4) the power lost to a given mode may be minimized by maximizing the ratio $\overline{\delta\beta}$ to $\bar{\kappa}$ for each mode, in effect allowing the modes a chance to de-phase before substantial power exchange takes place. The number of modes with propagation constants similar to the excited mode (i.e. guided modes) should therefore be minimized, and for modes that cannot be cut-off, the difference in their rates of propagation maximized. A large aspect ratio waveguide will ensure greatly differing rates of propagation for the guided modes. Additionally, for an achievable $\overline{\delta\beta}$ the ratio of $\overline{\delta\beta}$ to $\bar{\kappa}$ may always be increased through longer transitions since the coupling coefficient (2.2) is proportional to the rate of change of the dielectric. Both $\overline{\delta\beta}$ and $\bar{\kappa}$ are robust with respect to changes in wavelength and/or dimension. As a result, devices operating on this principle, commonly referred to as mode-evolution, tend to be both inherently broadband and fabrication tolerant.

Polarization maintaining fiber is an example implementation of the device depicted in Fig. 2-1. A slow twist (large ratio of $\overline{\delta\beta}$ to $\bar{\kappa}$) allows for the polarization to rotate with the rotation of the fiber axis while a rapid twist (small ratio of $\overline{\delta\beta}$ to $\bar{\kappa}$) couples the slow and

fast axes of the fiber scrambling the polarization. The birefringence of the fiber inhibits coupling between the modes. So long as the twist is sufficiently slow so as to maintain a large ratio of $\overline{\delta\beta}$ to $\bar{\kappa}$, the polarization state is maintained.

2.2 Three-Layer Polarization Rotators

Since current standard fabrication techniques rely on layered processes, a twisted waveguide (Fig. 2-1) is difficult to implement on an integrated optic chip. Fortunately, it turns out that a good approximation to a twisted waveguide can be achieved rather easily with only a few waveguide core layers. An example structure is depicted in Fig. 2-2. The approximation is achieved by removing material from the upper and lower layers and adding it to the middle layer. The use of three core layers assures symmetry about the axis of rotation which minimizes the perturbation required to achieve rotation of the axis of polarization. The layers are asymmetrically and oppositely tapered providing an effective twist of the waveguide axis. In contrast to a pure twist, the mode set changes, yet a large average difference in the rates of propagation of the guided modes is maintained by the large aspect ratio of the waveguide thereby inhibiting power exchange between the modes.

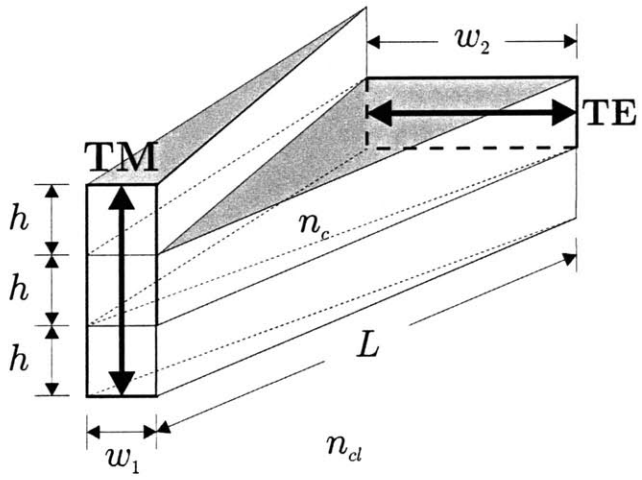

Figure 2-2: A mode-evolution-based polarization rotator that uses three core layer to approximate a twisted waveguide.

The rotation of the axis of polarization may be determined by an examination of the guided modes. We consider an example structure with core and cladding indices of $n_c = 2.2$

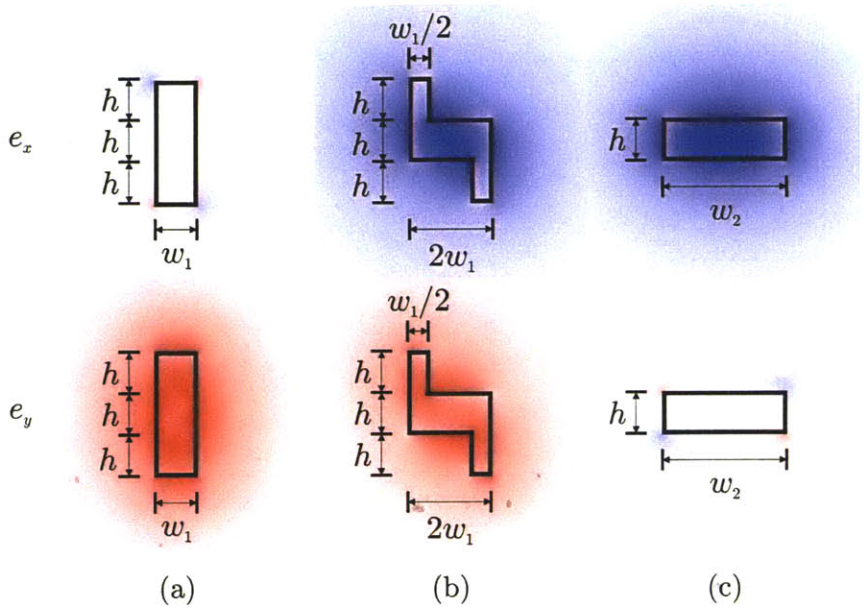

Figure 2-3: The x and y components of the electric field of the fundamental mode of the three-layer rotator depicted in Fig. 2-2 at the (a) beginning, (b) middle, (c) and end of the structure. Here, $h = 0.25\,\mu$m, $w_1 = 0.25\,\mu$m, and $w_2 = 0.75\,\mu$m with the core and cladding indices set to $n_c = 2.2$, and $n_{cl} = 1.445$, respectively. Here, x and y are horizontal and vertical axes, respectively.

and $n_{cl} = 1.445$, respectively. The reasoning for the particular choice of indices will become apparent in Chapter 5, but any index contrast will work. The dimensions are $w_1 = 0.25\,\mu$m, $w_2 = 0.75\,\mu$m and $h = 0.25\,\mu$m and thus the input and output waveguide cross-sections are rotated versions of one another. The modes at the beginning, middle, and end of the structure were calculated with a finite-difference modesolver [20, 11] (see also Appendix B.3) and the e_x and e_y components of the fundamental mode are presented in Fig. 2-3. From the modal field distribution, it is evident that at the beginning the mode is y-polarized, at the middle it is nearly evenly split between the x and y polarizations, and at the end it is x-polarized. From here on horizontal (x-directed) and vertical (y-directed) polarizations will simply be referred to as transverse electric (TE) and transverse magnetic (TM) polarizations, respectively.[†]

Fig. 2-3 demonstrates the evolution of the fundamental mode along the transition. However, whether or not power remains in the fundamental mode may only be determined

[†]This definition is by convention as rectangular dielectric waveguide modes can be neither pure TE nor pure TM.

by propagating the field with a rigorous implementation of Maxwell's equations. Three-dimensional finite-difference time-domain (FDTD) [21] and eigenmode expansion (EME) [22, 23] simulations were used to verify the device performance. Both techniques are rigorous, with the limitation of FDTD being only a result of discretization error and that of EME being the limited mode-set used in the computation. For the FDTD simulations discretizations of $dx = 0.125\,\mu$m and $dy = dz = 0.25\,\mu$m corresponding to $\sim \lambda/80$ and $\sim \lambda/40$ in the material, respectively, were used while EME simulations were performed with only the guided modes. More detailed discussions of the FDTD and EME techniques are presented in Appendices B.1 and B.2.

FDTD and EME simulations were performed as a function of the device length for a wavelength of $\lambda = 1.55\,\mu$m. The results are presented in Fig. 2-4a and indicate that a device length of $100\,\mu$m is sufficient to efficiently induce polarization rotation. The two techniques show strong agreement with the only discrepency arising in the $100\,\mu$m long simulation where the grid induced roughness introduces a small amount of spurious loss in the FDTD simulation. The results support the results of the coupled-local-mode theory presented in the previous section. Since the ratio of $\overline{\delta\beta}$ to $\bar{\kappa}$ determines the device performance and the coupling $\bar{\kappa}$ is inversely proportional to length of the device, the cross-talk exhibits an inverse dependence on device length. Moreover, Fig. 2-4a. confirms the theory that radiation modes have little impact on device performance as the power is almost fully conserved by the fundamental and secondary guided modes.

The wavelength dependence of the $100\,\mu$m long device as determined from a discrete Fourier transform (DFT) taken during the FDTD simulation is presented in Fig. 2-4b. The simulation indicates that the structure exhibits nearly lossless transmission, and almost no wavelength dependence over the 1.45 to $1.75\,\mu$m band. Moreover, while the DFT was only taken over this wavelength range, it is reasonable to assume that the device bandwidth far exceeds this 300 nm band.

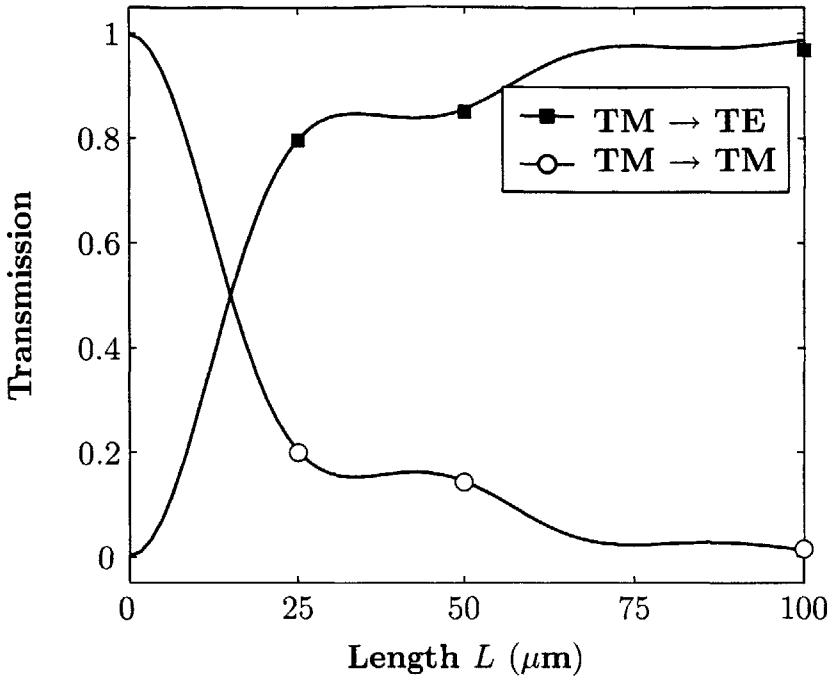

(a)

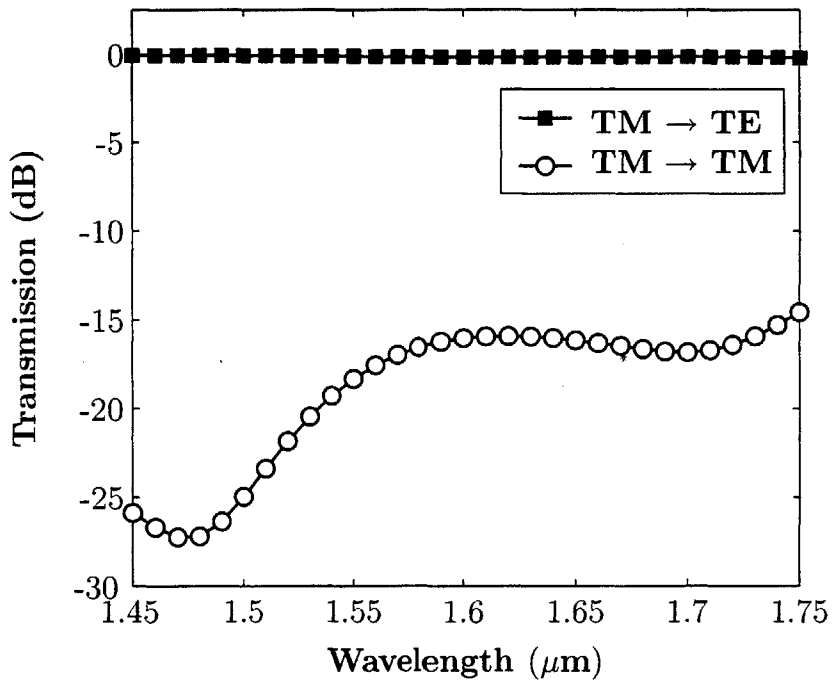

(b)

Figure 2-4: (a) FDTD (marked points) and EME simulations as function of device length for a wavelength of $\lambda = 1.55\,\mu$m, and (b) FDTD determined wavelength dependence for a $100\,\mu$m long device. Simulation results are for the device presented in Fig. 2-2 with $n_c = 2.2$, $n_{cl} = 1.445$, $h = 0.25\,\mu$m, $w_1 = 0.25\,\mu$m, and $w_2 = 0.75\,\mu$m.

A nice feature of mode-evolution-based devices is that the particular geometry of the structure is not especially important. As a result, many variations of the basic structure may be used to achieve the same result so long as a large ratio of $\overline{\delta\beta}$ to $\bar{\kappa}$ is maintained. The structure depicted in Fig 2-2 has one obvious limitation. That is, it requires high resolution lithography to enable the adiabatic transition. If e-beam lithography is an available tool, then this is perhaps only a minor concern. However, often it is desirable to use optical lithography. Commonly available optical lithography systems currently have resolution limits of roughly $\sim 0.25\,\mu$m. Fortunately, the structure in Fig. 2-2 can be modified to maintain a critical dimension of $0.25\,\mu$m. Instead of tapering the width of the upper and lower layers, they may alternatively be moved adiabatically into the evanescent field of the guided mode. Such a structure is depicted in Fig. 2-5. FDTD and EME simulations of the

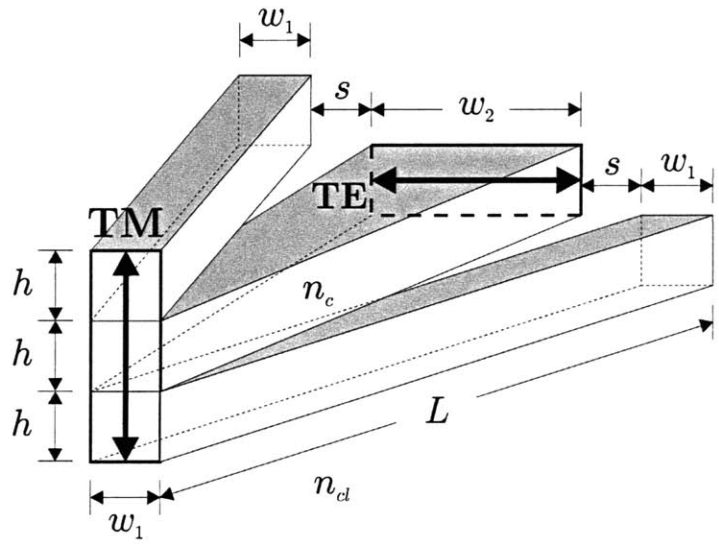

Figure 2-5: A three layer polarization rotator formed by adiabatically moving the upper and lower layers into the evanescent field of the guided mode while increasing the width of the middle layer. The structure can be fabricated with optical lithography.

structure as a function of device length at a wavelength of $\lambda = 1.55\,\mu$m are presented in Fig. 2-6a. The results indicate that a device length of only $50\,\mu$m is sufficient to efficiently induce polarization rotation. The wavelength dependence of a $50\,\mu$m device as determined from a DFT taken during the FDTD simulation is presented in Fig. 2-6b. Here again, the structure exhibits nearly lossless transmission, and almost no wavelength dependence over the 1.45 to $1.75\,\mu$m band.

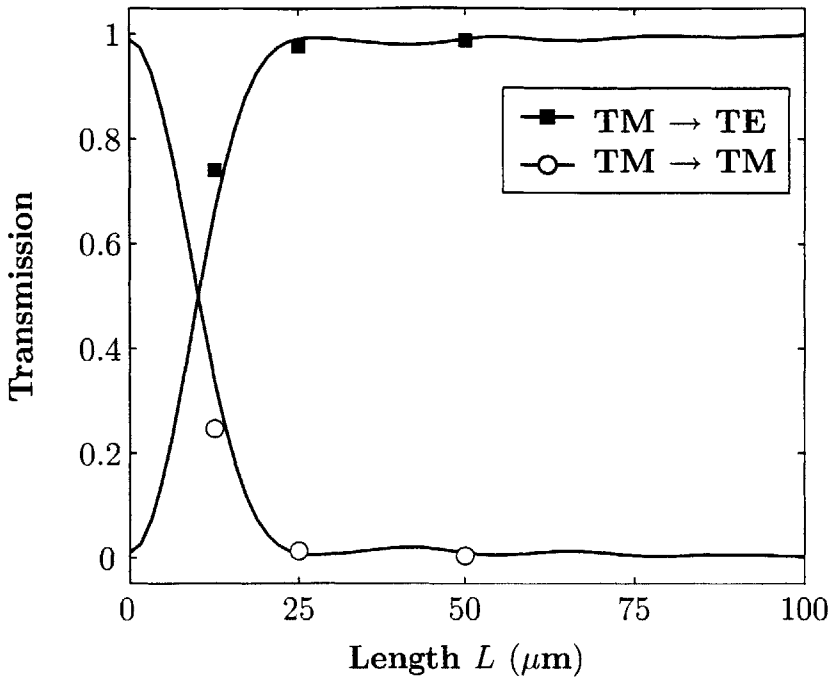

(a)

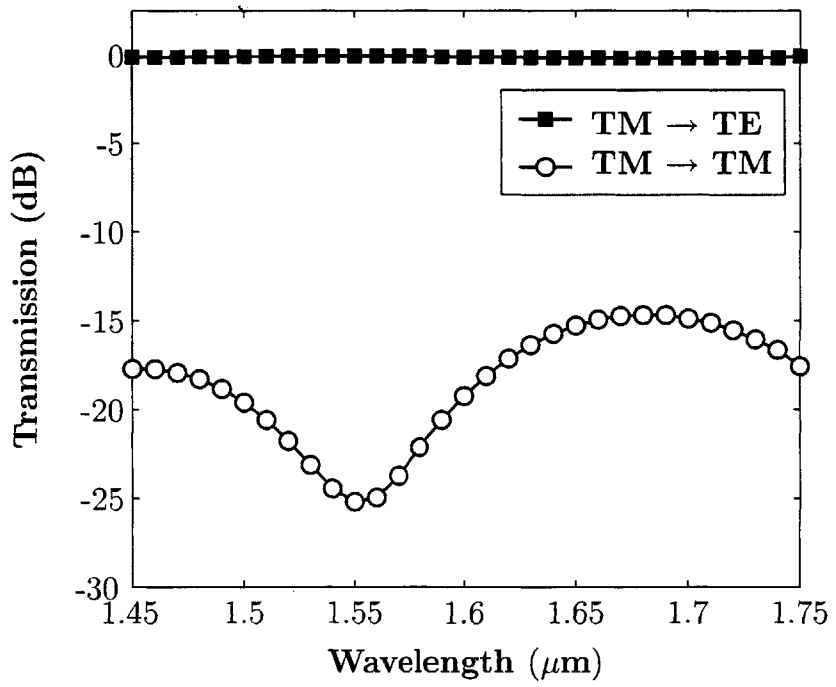

(b)

Figure 2-6: (a) FDTD (marked points) and EME simulations as function of device length for a wavelength of $\lambda = 1.55\,\mu$m, and (b) FDTD determined wavelength dependence for a $50\,\mu$m long device. The simulation results are for the device presented in Fig. 2-5 with $n_c = 2.2$, $n_{cl} = 1.445$, $h = 0.25\,\mu$m, $w_1 = 0.25\,\mu$m, $w_2 = 0.75\,\mu$m, and $s = 0.125\,\mu$m.

2.3 Two-Layer Polarization Rotators

The structures depicted in Fig. 2-2 and Fig. 2-5 are remarkably efficient at converting polarization in only $100\,\mu$m and $50\,\mu$m long structures, respectively. However, fabricating three layer structures is still quite challenging. Ideally, as few layers as possible should be used to induce polarization rotation. Fortunately, Gauss' Law for dielectrics ($\nabla \cdot \epsilon \mathbf{E} = 0$) ensures that the fundamental mode takes on a polarization that is largely aligned to the principal axis of the waveguide even when the waveguide is a crude structure formed from only a pair of rectangular dielectric cross-sections. Thus, only two-core layers are required to induce polarization rotation. The two-layer analog to the structure depicted in Fig. 2-2 is shown in Fig. 2-7. Symmetry about the axis of rotation is no longer maintained. As a result, the perturbation to the guided modes is stronger as the mode is displaced in addition to having its axis of rotation modified. It is therefore reasonable to assume that an efficient conversion of polarization states will require longer device lengths, yet the effective twisting of the geometrical axis should still ensure that the device rotates polarization.

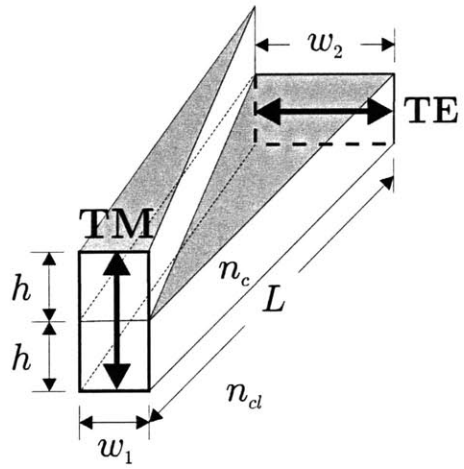

Figure 2-7: Diagram of a polarization rotator utilizing only two core layers.

The rotation of the axis of polarization may be determined by an examination of the guided modes. The modes at the beginning, middle, and end of an example structure were here again calculated and the e_x and e_y components of the fundamental mode are presented in Fig. 2-8. The example structure has a core index $n_c = 2.2$, a cladding index $n_{cl} = 1.445$ and dimensions $w_1 = 0.4\,\mu$m, $w_2 = 0.8\,\mu$m and $h = 0.4\,\mu$m. The figure clearly demonstrates

an evolution of the polarization state, from a vertically oriented or TM polarization to a horizontally oriented or TE polarization.

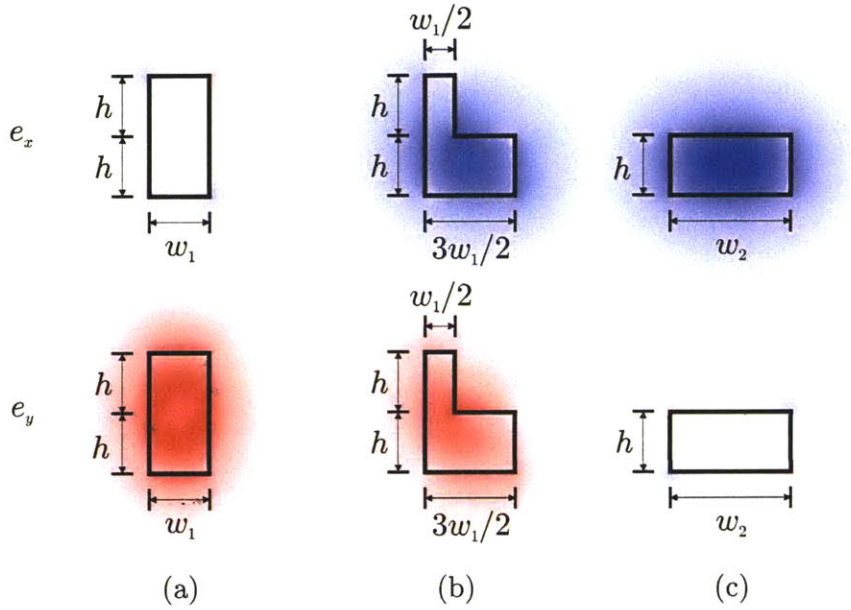

Figure 2-8: The x and y components of the electric field of the fundamental mode of the two-layer rotator depicted in Fig. 2-7 at the (a) beginning, (b) middle, (c) and end of the structure. Here, $h = 0.4\,\mu$m, $w_1 = 0.4\,\mu$m, and $w_2 = 0.8\,\mu$m with the core and cladding indices set to $n_c = 2.2$, and $n_{cl} = 1.445$, respectively.

Fig. 2-8 demonstrates the evolution of the fundamental mode along the transition. However, to verify the device performance, FDTD and EME simulations were again performed as a function of device length for a wavelength of $1.55\,\mu$m. The results are plotted in Fig. 2-9. The FDTD and EME results are in agreement indicating that the polarization conversion is nearly perfect for device lengths above $200\,\mu$m. To determine the wavelength dependence a DFT was applied during the FDTD simulation of the $200\,\mu$m long device. The wavelength dependence of the $200\,\mu$m long device is plotted in Fig. 2-9b. No significant wavelength sensitivity is observed with $< -17\,$dB cross-talk between the output polarization states obtained across the entire 1.45 to $1.75\,\mu$m band.

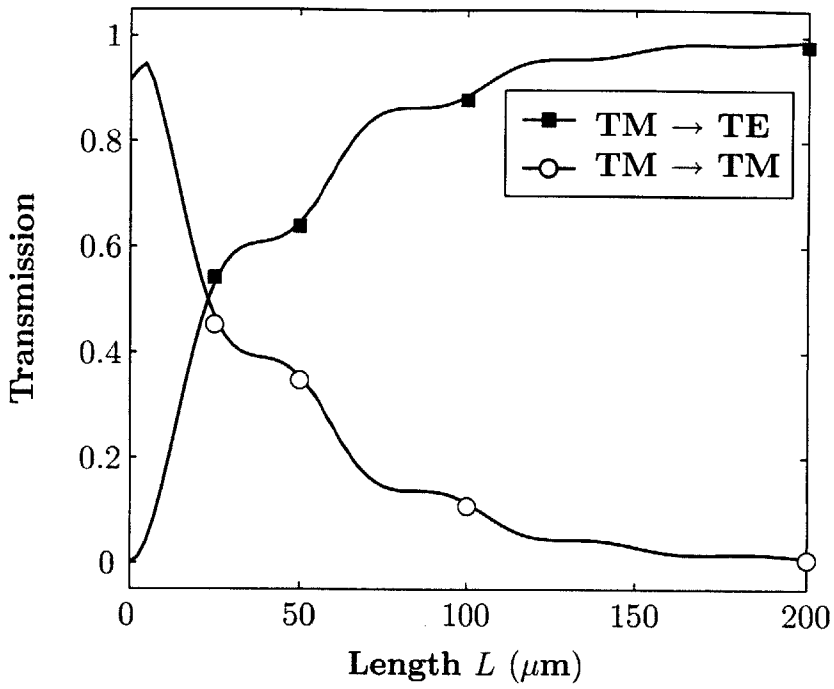

(a)

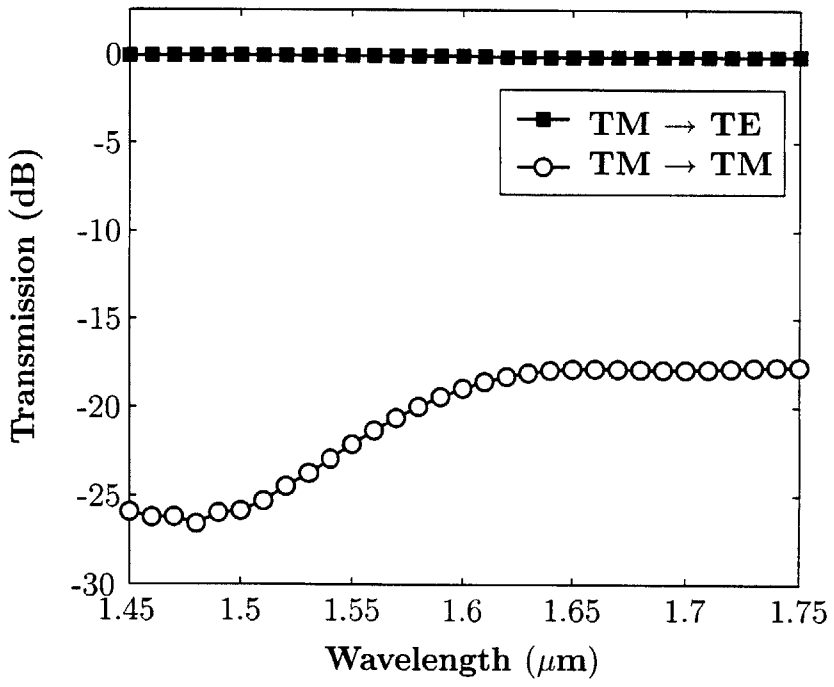

(b)

Figure 2-9: (a) FDTD (marked points) and EME simulations as function of length for a wavelength of $\lambda = 1.55\,\mu$m and (b) FDTD determined wavelength dependence for a $200\,\mu$m long implementation of the two-layer polarization rotator depicted in Fig. 2-7 with $n_c = 2.2$, $n_{cl} = 1.445$, $h = 0.4\,\mu$m, $w_1 = 0.4\,\mu$m, and $w_2 = 0.8\,\mu$m

While the device in Fig. 2-7 may be fabricated with e-beam lithography, here again optical lithography systems are not capable of resolving the fine features of the structure. As an alternative, the width of the upper layer may be held constant or tapered slightly while it is moved away from the lower section and into the evanescent field of the guided modes (Fig. 2-10). Doing so presents a tradeoff; the minimum feature size is increased but the planarization must now smoothly extend across material boundaries. The effect on propagation is similar to a pure tapering of the upper core layer width.

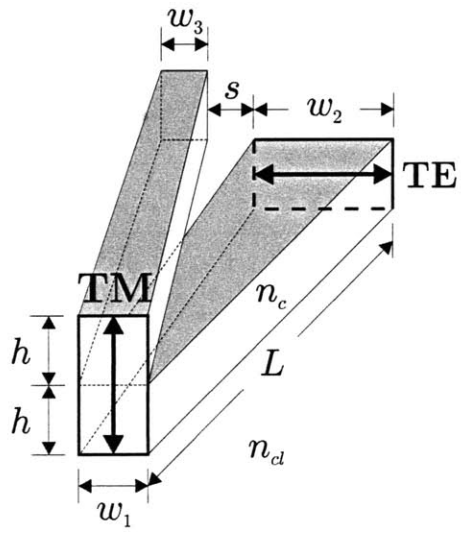

Figure 2-10: Diagram of a two-layer polarization rotator using tapering and separation of the upper and lower core layers to induce polarization rotation.

Results of FDTD and EME simulations as a function of length for the device in Fig. 2-10 are plotted in Fig. 2-11a for a wavelength of 1.55 μm. The wavelength dependence of a 100 μm long structure as determined from a FDTD simulation is shown in Fig. 2-11b. Again strong agreement is obtained between FDTD and EME results with no significant wavelength sensitivity across the 1.45 to 1.75 μm band.

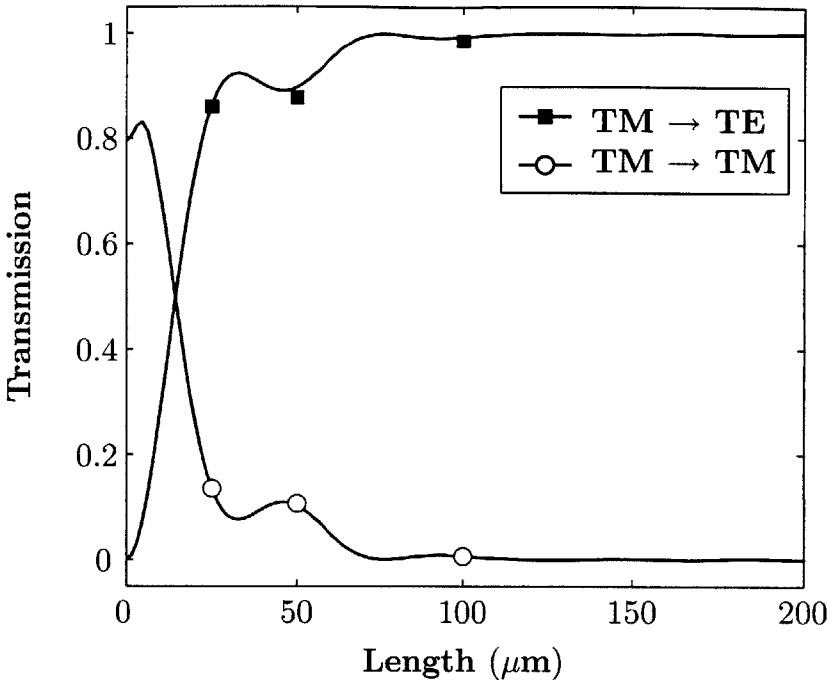

(a)

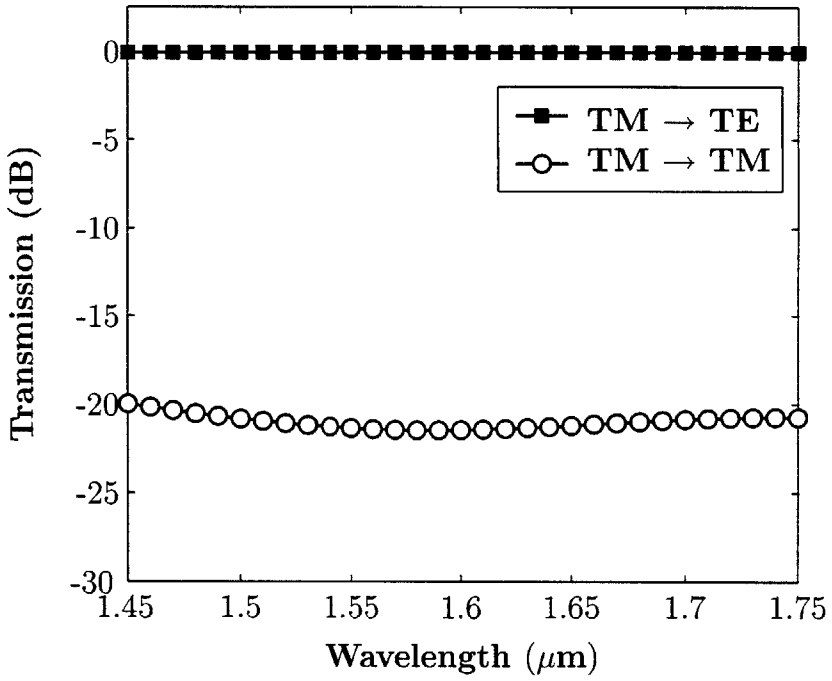

(b)

Figure 2-11: FDTD (marked points) and EME expansion results for the polarization converter depicted in Fig. 2-10 (a) as a function of the device length for a wavelength of $\lambda = 1.55\,\mu$m and (b) and versus wavelength for a $100\,\mu$m long device with $n_c = 2.2$, $n_{cl} = 1.445$, $h = 0.4\,\mu$m, $w_1 = 0.4\,\mu$m, $w_2 = 0.8\,\mu$m, $w_3 = 0.25\,\mu$m, and $s = 0.25\,\mu$m

2.4 Summary

Mode-evolution-based polarization rotators requiring two- and three-core layers have been designed and their theoretical performance verified through full three-dimensional FDTD and EME simulations. The simulations results are in strong agreement indicating that broadband ($> 300\,\text{nm}$), low-loss ($< 0.1\,\text{dB}$), and low cross-talk ($\sim -20\,\text{dB}$) performance is achievable with relatively short ($100 - 200\,\mu\text{m}$) structures. Perhaps more importantly, the mode-evolution approach only requires that mode coupling be inhibited, a far looser requirement than ensuring mode-coupling. As a result, the mode-evolution-based polarization rotator designs presented in this chapter are inherently broadband and insensitive to geometrical variations, making them highly tolerant to fabrication errors.

Chapter 3

Integrated Polarization Splitters

With the challenge of rotating polarization on-chip solved by the mode-evolution-based polarization rotators described in the previous chapter, all that remains is to solve the problem of splitting polarization states on-chip to implement an integrated polarization diversity scheme. Polarization splitters may also be formed with either mode-coupling or mode-evolution-based approaches. However, given the success of the mode-evolution-based polarization rotators, it was only natural to consider mode-evolution as the operating principle for forming a polarization splitter.

In contrast to polarization rotators, several integrated mode-evolution-based polarization splitters have been proposed [24, 25, 26, 27, 28, 15]. Here, new mode-evolution-based polarization splitters that mate directly to polarization rotators of Chapter 2 are proposed. And, in contrast to the prior art, the polarization splitters proposed herein require only a single material system. The performance of both three- and two- layer devices are verified through rigorous electromagnetic simulations and in the case of the two-layer structure, experimental results. Again, while much of this work has previously been published [29, 15, 17, 18], herein we provide a comprehensive review.

3.1 A Three-Layer Polarization Splitter

An integrated polarization splitter takes a mixed polarization state in a single input guide and splits it into orthogonal components in separate output guides. For such a device to operate through the principle of mode-evolution, the fundamental TE and TM modes of the combined structure must naturally evolve from the input guide to separate output guides.

And, for the device to exhibit low cross-talk, coupling induced by the transition must be suppressed. The coupled-local-mode theory presented in Section 2.1 demonstrated that the coupling to a mode m, given by (2.4), is minimized by maximizing the ratio of $\overline{\delta\beta}$ to $\bar{\kappa}$. This result is general and applies equally to all mode-evolution-based devices.

With this result in mind, mode-evolution-based polarization splitters may be formed from pairs of vertically and horizontally oriented waveguides. A simple symmetric intersection of a pair of identical rectangular waveguides with a 90° rotation between them will act as a polarization splitter if the guides are separated slowly. Such a structure is depicted in Fig. 3-1. The boundary conditions imposed by Gauss' Law cause the fundamental TE and TM modes of the combined structure to be largely confined to the horizontally and vertically oriented guides, respectively. Since the guide sections are rotated versions of one another, the fundamental or TE_{11} mode and TM_{11} modes are nearly degenerate. As such, the modes always remain in phase enabling coupled power to build over the course of the evolution of the structure. However, by centrally intersecting the guides, the coupling between the fundamental modes is prevented by mode symmetry. Note from (2.2), we see that the coupling goes to zero when the overlap between the modal electric fields ($\int_A \mathbf{e}_m^* \cdot \mathbf{e}_n \frac{d}{dz}\varepsilon dA$) goes to zero. The modal field distributions of an example structure are presented in Fig. 3-2 to illustrate this point.

Still, the secondary TM_{21} and TE_{21} modes (not shown) do not possess the symmetry required to prevent coupling between their like-polarized counterparts. Yet, on account of the large aspect ratio of the guides, the like polarized modes propagate at greatly differing rates (i.e. $\overline{\delta\beta}$ is large). Radiation or unguided modes are of even less concern as they propagate at much higher rates still. Thus, with the exception of the orthogonally polarized modes which exhibit no coupling, all modes exhibit large $\overline{\delta\beta}$'s with respect to the fundamental guided modes. As a result, a large ratio of $\overline{\delta\beta}$ to $\bar{\kappa}$ may be maintained despite a rapid evolution of the structure ensuring that little power is lost to any given mode. Since at the output the fundamental output TE_{11} mode is confined to the horizontally oriented guide while the TM_{11} mode is confined to the vertically oriented guide, efficient polarization splitting should result.

To demonstrate this result, an example structure with a core index of $n_c = 2.2$, cladding index of $n_c = 1.445$, $h = 0.25\,\text{mum}$, $w_1 = 0.25\,\mu\text{m}$, $w_2 = 0.75\mu m$, and $s = 1\,\mu\text{m}$ is considered. The guides are rotated versions of one another with a large aspect ratio to ensure a

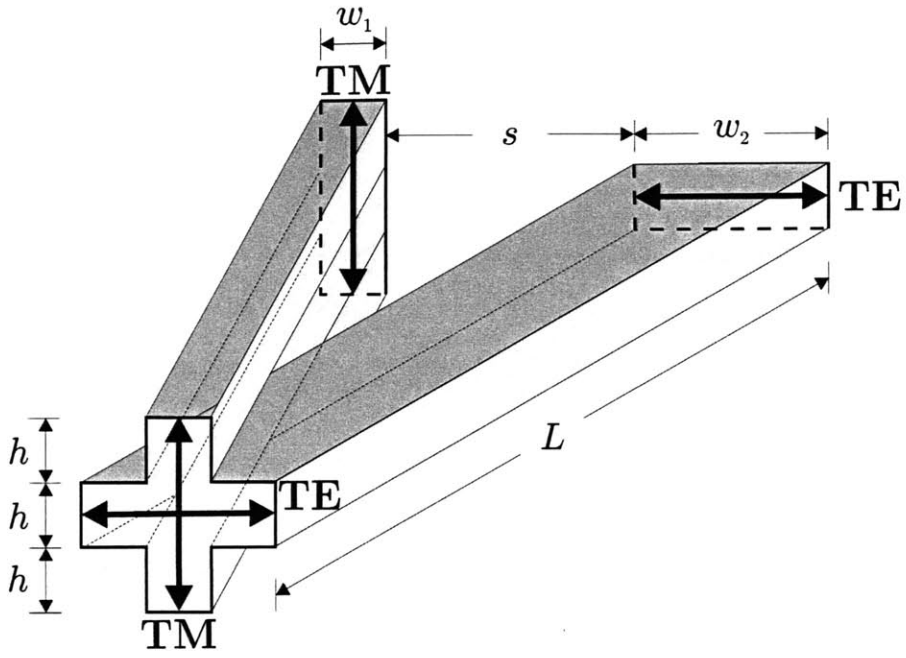

Figure 3-1: A mode-evolution-based polarization splitter formed from intersected vertically and horizontally oriented waveguides. The TE mode follows the horizontally oriented waveguide while the TM mode follows the vertically oriented waveguide.

large $\overline{\delta\beta}$ between like-polarized modes. Three-dimensional FDTD and eigenmode-expansion (EME) simulations were performed to verify the performance of the approach. FDTD results were obtained by separately launching the fundamental TE and TM input modes and monitoring the power in the TE and TM output modes. The modal power was determined from a numerical implementation of the orthogonality relation for power normalized modes (i.e. $\delta_{mn} = \frac{1}{2}\int \mathbf{e}_m \times \mathbf{h}_n \cdot \hat{\mathbf{z}} dA$). EME results were obtained from the four guided modes. Results of the FDTD and EME simulations as function of device length L at a wavelength of $1.55\,\mu$m are presented in Fig. 3-3a. The simulations are in agreement confirming the intuition that coupling amongst guided TM modes limits performance. Slower transitions induce less coupling allowing the modes a chance to de-phase before exchanging substantial amounts of power. For lengths $L > 50\,\mu$m or angle $\alpha < 0.02$, the polarization splitting is nearly perfect. Spectral information obtained from a discrete Fourier transform (DFT) in an FDTD simulation of a $50\,\mu$m long device is presented in Fig. 3-3b. More than 22 dB of extinction is observed over the entire 1.45 to $1.75\,\mu$m regime. The bandwidth is only limited by decreasing ratios of $\overline{\delta\beta}/\bar{\kappa}$ at either end of the spectrum.

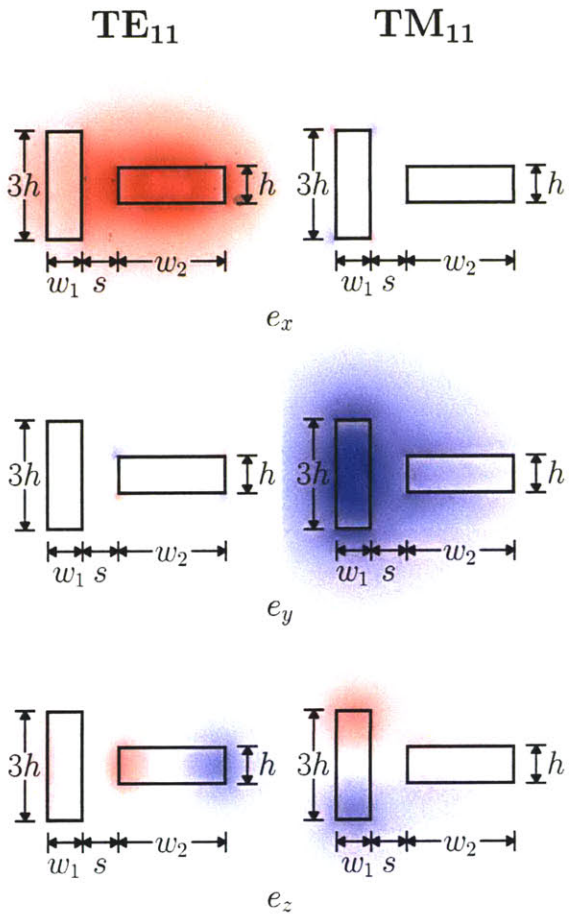

Figure 3-2: Field distributions of the TE_{11} and TM_{11} modes of the structure depicted in Fig. 3-1 with $n_c = 2.2$, $n_{cl} = 1.445$, $h = 0.25\,\mu$m, $w_1 = 0.25\,\mu$m, $w_2 = 0.75\,\mu$m, and $s = 0.25\,\mu$m. The mode symmetry prevents coupling.

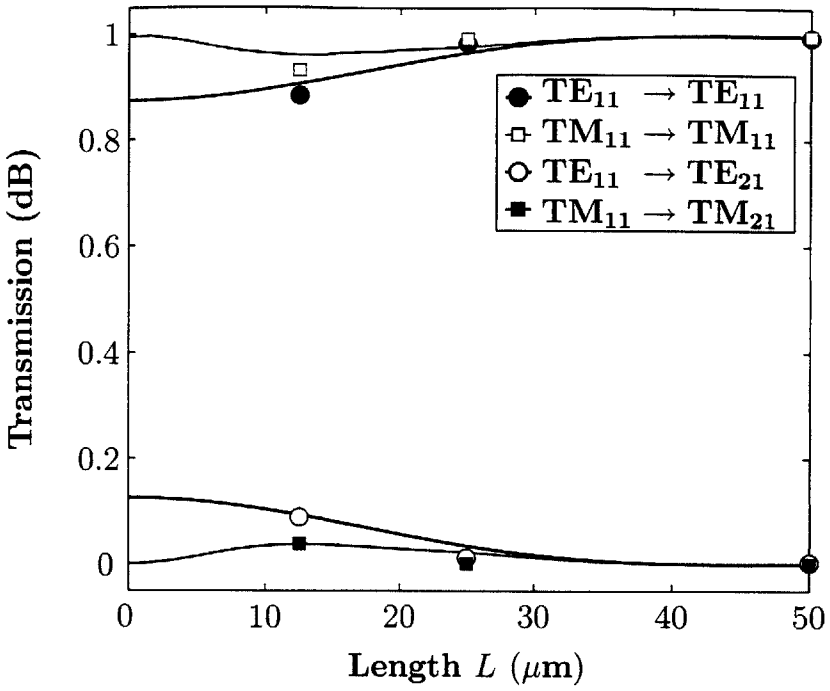

(a)

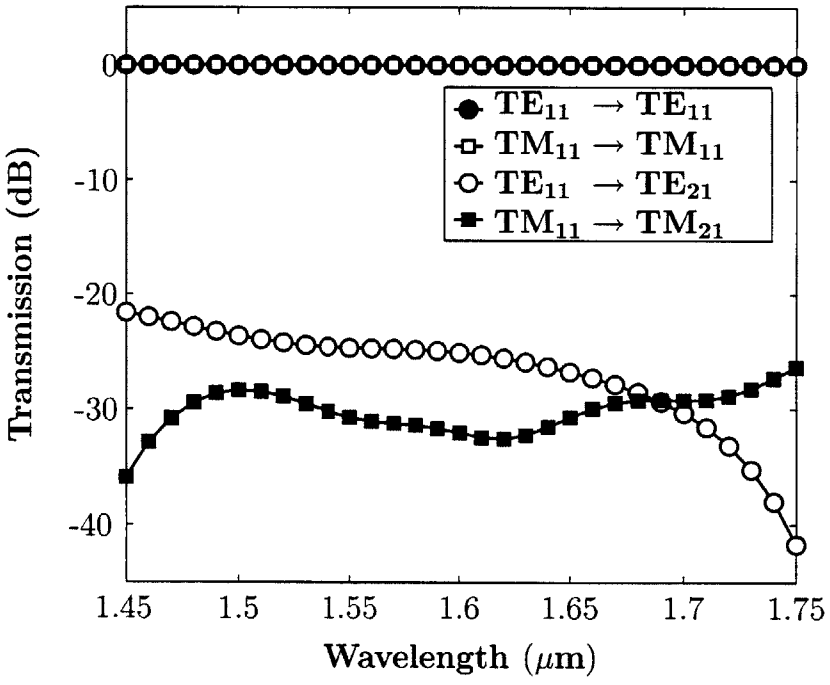

(b)

Figure 3-3: (a) FDTD (marked points) and EME simulations as function of device length, and (b) FDTD determined wavelength dependence for a $50\,\mu$m long device. Simulation results are for the device presented in Fig. 3-1 with $n_c = 2.2$, $n_{cl} = 1.445$, $h = 0.25\,\mu$m, $w_1 = 0.25\,\mu$m, $w_2 = 0.75\,\mu$m , and $s = 1\,\mu$m.

3.2 A Two-Layer Polarization Splitter

The centrally intersected guides of the splitter in Fig. 3-1 require three core layers to implement. Moreover, the point of intersection between the guides is unlikely to be reproduced accurately when fabricated as a result of both lithographic and material filling limitations. Such fabrication errors would cause the transition to be non-adiabatic. The fabrication could be greatly simplified by utilizing fewer layers, and removing the point of intersection. Fig. 3-4 depicts a polarization splitter that requires only two core layers and avoids a point of intersection between the vertically and horizontally oriented waveguides. Rather than intersect the guides, the guides are transitioned into close proximity. Here, the transition is accomplished by a simple tapering of the vertically oriented waveguide width. However, any transition will work so long as the fundamental TE and TM modes begin in the horizontally oriented guide and the transition is adiabatic. While a simple taper transition alleviates the material filling issue, high resolution lithography is still required. Although not considered here, alternate transitions which address both lithographic and material filling concerns include combining a width taper with a decrease in the separation of the guides and separately bringing pieces of the vertically oriented waveguide into proximity with the horizontally oriented waveguide.

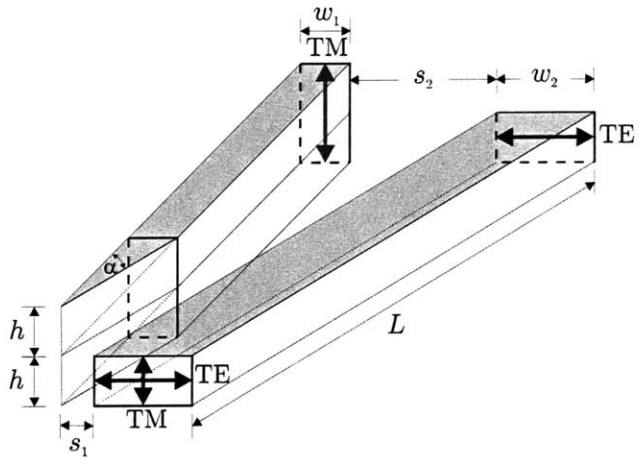

Figure 3-4: Diagram of a two-layer polarization splitter.

The structure consists of a horizontally oriented guide of height h and width w_2 and a vertically oriented guide of height $2h$ formed at a separation s_1, transitioned to a width w_1, and subsequently separated to a distance s_2. Again, on account of Gauss' Law, a

proper choice of h, w_1 and w_2 will ensure that the fundamental TE mode (i.e. TE_{11}) of the combined structure remains in the horizontally oriented guide while the fundamental TM mode (i.e. TM_{11}) transitions from the horizontally oriented guide to the vertically oriented guide. Still, power exchange between modes must be suppressed for the power to remain in the initially excited modes.

Since the waveguides of the two-layer structure are not symmetrically aligned, even orthogonally polarized modes are coupled by the evolution of the structure. Thus, in contrast to the three-layer splitter which relied on mode symmetry to prevent coupling between orthogonally polarized modes, the propagation constants of all four modes must be staggered. A large difference in the propagation constants of the TE modes is assured simply by using large aspect ratio waveguides. However, achieving the same result for the TM modes which must exchange primary guides is complicated by the fact that the $\overline{\delta\beta}$ is also intimately tied to the initial separation s_1. Large initial separations lead to TM modes that reach a point of near degeneracy as the width of the vertically oriented guide is transitioned to w_1. Finally, a $\overline{\delta\beta}$ between orthogonally polarized modes is achieved by making the vertically oriented guide slightly smaller in size than the horizontally oriented one. While these represent general guidelines for achieving modes with staggered propagation constants, eigenmode solutions must be obtained to assure the result.

As an example, we chose guides with core and cladding indices of $n_c = 2.2$ and $n_{cl} = 1.445$ and dimensions $h = 0.4\,\mu$m, $w_1 = 0.35\,\mu$m, and $w_2 = 0.8\,\mu$m. The guides are rotated versions of one another with a slight difference in the smaller dimension to break the degeneracy of the TE and TM modes. A chosen initial separation of $s_1 = 0.25\,\mu$m is large enough for fabrication but small enough to maintain a large $\overline{\delta\beta}$ between the TM modes. Since the vertically oriented waveguide evolves along the length of the transition, we cannot simply consider the modes of the individual guides, but must instead consider the modes of the combined structure as they evolve. The modes at three cross-sections of the example structure were calculated using a finite-difference modesolver. Fig. 3-5 and Fig. 3-6 show the major field components of the TE and TM modes and their effective indices $n_{eff} = \beta\lambda/2\pi$, respectively, at various points along the transition. Fig. 3-5 reveals that the TE_{11} mode remains in the horizontally oriented waveguide largely unaffected by the perturbation while a TE_{21} mode develops in the vertically oriented guide. Since only the TE_{11} and TM_{11} modes are initially excited, the fractional power in the TE_{21} and TM_{21}

modes is determined by the power exchange induced by the transition. The TE modes exhibit little overlap in the region of perturbation and vastly different effective indices at all points along the transition. Thus, little power exchange is expected between the TE modes. However, from Fig. 3-6a and 3-6b we see that the TM modes exchange guides. The transition, although necessary, causes the TM modes to exhibit much greater overlap through the perturbation than their TE counterparts. Since the TM effective indices are also more similar, power exchange amongst the TM modes is expected to limit the device performance. Still, from Fig. 3-5c and Fig. 3-6c it is clear that at a separation of $s_2 = 1\,\mu$m, the TE_{11} and TM_{11} modes propagate in separate guides. The modes have been isolated and the waveguides may be rapidly separated.

To verify the performance of the approach, FDTD and EME simulations were here again performed. However, since this two-layer splitter exhibits a smaller $\overline{\delta\beta}$ between modes than the three-layer splitter, it is more susceptible to spurious loss caused by the roughness of the FDTD grid. To minimize FDTD grid induced loss the primary guides were aligned to the FDTD grid. Results of the FDTD and EME simulations as function of device length L at a wavelength of $1.55\,\mu$m are presented in Fig. 3-7a.

The alignment of the structure to the FDTD grid, minimized spurious loss to a negligible amount in all but the $200\,\mu$m TM FDTD simulation. Otherwise, the simulations are in agreement confirming the intuition that coupling amongst guided TM modes limits performance. Slower transitions induce less coupling allowing the modes a chance to dephase before exchanging substantial power. For lengths $L > 200\,\mu$m or angle $\alpha < 0.0055$, the polarization splitting is nearly perfect. Spectral information obtained from a discrete Fourier transform (DFT) in an FDTD simulation of a $200\,\mu$m long device is presented in Fig. 3-7b. More than 22 dB of extinction is observed over the entire 1.45 to $1.75\,\mu$m band.

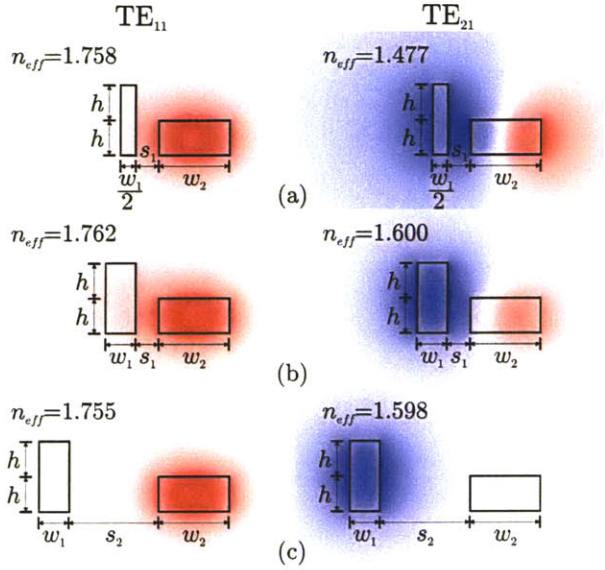

Figure 3-5: Major electric field components of the TE_{11} (left) and TE_{21} (right) modes at three points along the transition. At a separation of $s_2 = 1.0\,\mu$m the TE_{11} mode clearly propagates in the horizontally oriented guide.

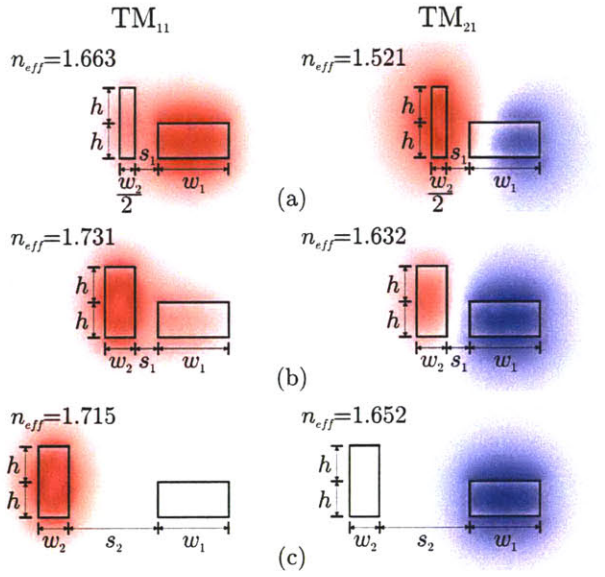

Figure 3-6: Major electric field components of the TM_{11} (left) and TM_{21} (right) modes at three points along the transition. At a separation of $s_2 = 1.0\,\mu$m the TM_{11} mode clearly propagates in the vertically oriented guide.

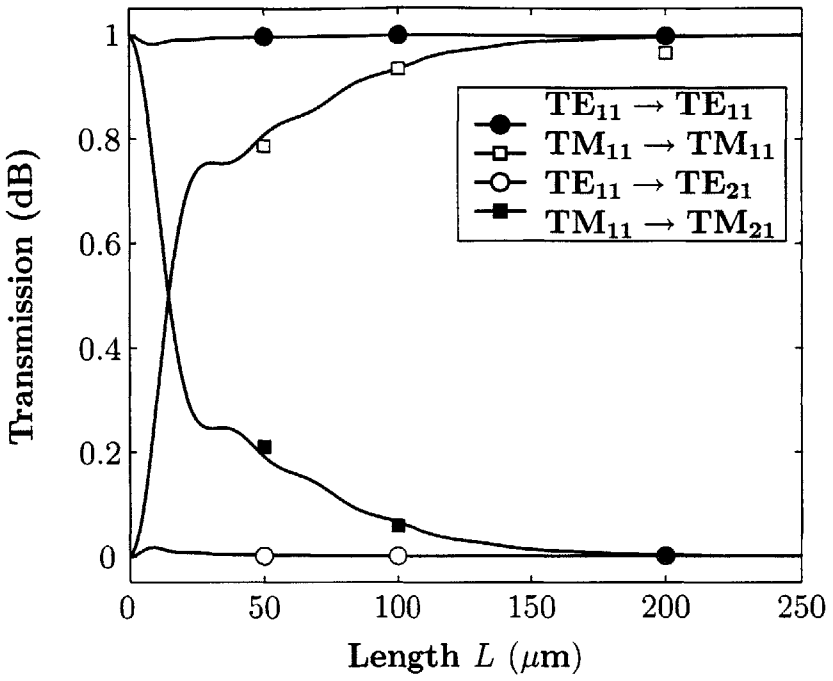

(a)

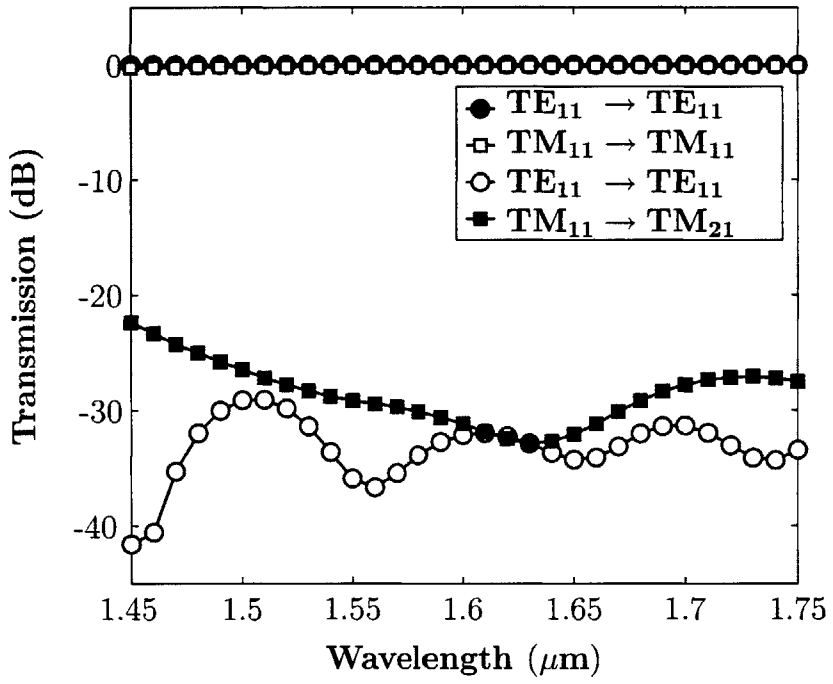

(b)

Figure 3-7: (a) FDTD (marked points) and EME simulations as function of device length, and (b) FDTD determined wavelength dependence for a $200\,\mu$m long device. Simulation results are for the device presented in Fig. 3-4 with $n_c = 2.2$, $n_{cl} = 1.445$, $h = 0.4\,\mu$m, $w_1 = 0.4\,\mu$m, $w_2 = 0.8\,\mu$m, $s_1 = 0.25\,\mu$m, and $s_2 = 1.0\,\mu$m.

3.3 Polarization Splitter-Rotators

With little to no modification of the three- and two-layer polarization rotator designs depicted in Chapter 2, integrated polarization splitter-rotators can be constructed by attaching a polarization rotator to the TM output port of a polarization splitter. The resulting devices take an arbitrary input polarization split it into TE and TM components and then rotate the TM output to produce a single on-chip TE polarization. Diagrams of such structures are depicted in Fig. 3-8. With the lessons learned in designing the two-layer splitter, the three-layer splitter was modified to avoid a point of intersection. Both devices are depicted with reverse taper mode-evolution-based mode converters to better match the input to the fiber and lensed fiber modes, respectively [30]. One of the nice features of the three-layer approach is that with $w_0 = h_0 = 0.25\,\mu$m, the match to the fiber mode is nearly 90%.

3.4 Summary

The three- and two-layer polarization splitters offer different and distinct advantages. In particular, the three-layer device allows for very rapid separation of the polarization states while the two layer device is more amenable to traditional fabrication techniques. In both cases, the mode-evolution approach enables broadband ($> 300\,$nm), low-loss, and low cross-talk performance in structures with lengths of only $50\,\mu$m and $200\,\mu$m, for the three- and two-layer cases, respectively. Moreover, the polarization rotators of the previous chapter can be directly integrated with these polarization splitters to enable a single on-chip polarization.

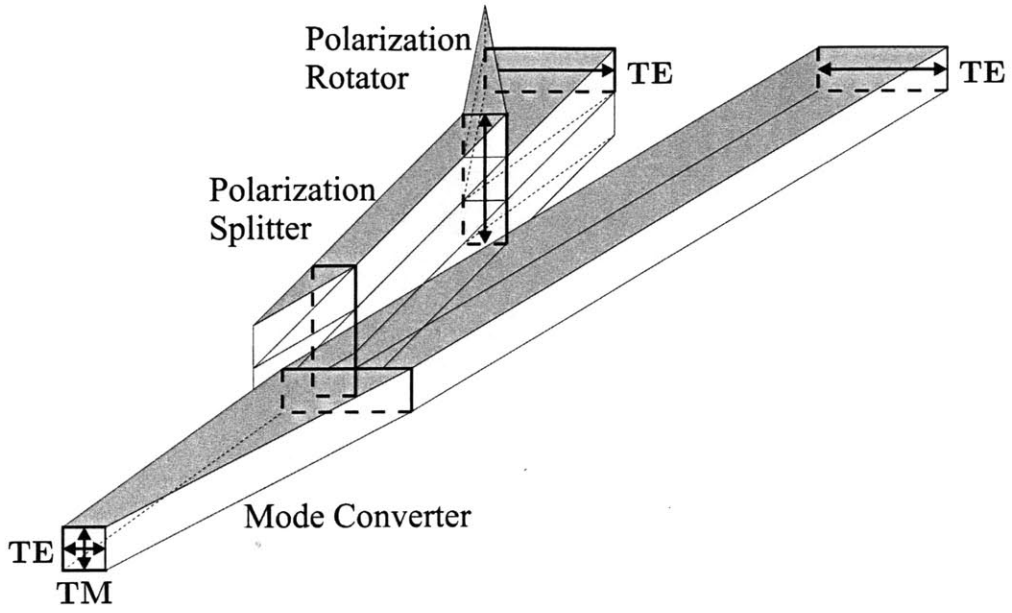

(a)

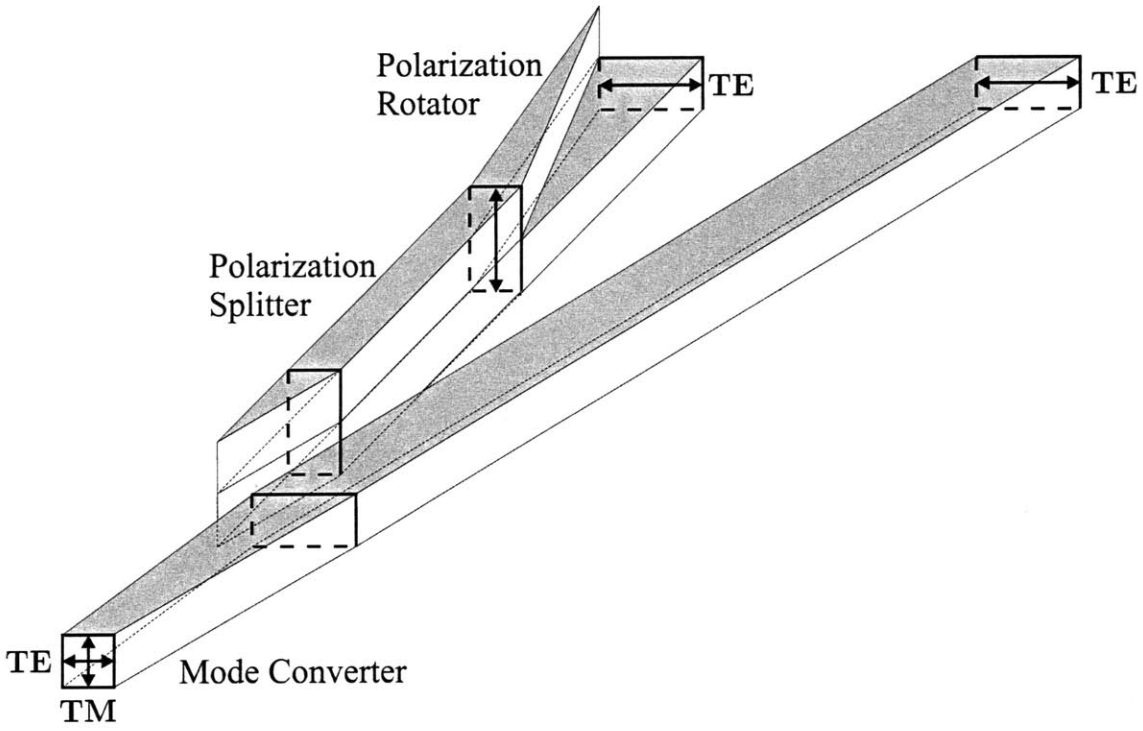

(b)

Figure 3-8: Integrated (a) three- and (b) two-layer polarization splitter-rotators formed by attaching polarizations rotators of the type presented in Chapter 2 to the TM output arm of the polarization splitters of the type presented in this chapter. Each structure is depicted with a mode-evolution-based reverse taper for mode-matching to fiber and lensed fiber input modes, respectively.

Chapter 4

Integrated Polarization Rotators, Splitters, and Splitter-Rotators: Fabrication and Characterization

After the considerable effort placed in the design of the polarization rotators, splitters, and splitter-rotators detailed in the previous two chapters, it was time to find an appropriate partner to fabricate these device designs. Initially, traditional fabrication methods were considered, that is, layers were to be deposited, patterned, over-cladded, and planarized and then the second core layer would be deposited, patterned, and over-cladded. Since all of the structures require a resolution of at least 0.25μm, e-beam lithography represented a natural choice. However, MIT's e-beam lithography tool is gold contaminated which prevents wafers exposed to the e-beam from being placed back into the clean room for further processing. As an alternative, several attempts were made to find a lab with a deep ultraviolet (DUV) lithography capability as MIT's optical lithography is limited to a 0.4 μm resolution. Yet, none of these attempts proved fruitful. As a result, for a significant period, designs existed with no fabrication solution in sight.

It was only after discussing this dilemma in detail with Tymon Barwicz, Minghao Qi, and Prof. Henry Smith of MIT's Nanostructures Lab, that a solution emerged. They proposed using a single material deposition with a two-step etch to avoid the requirement for re-introducing the wafers into the cleanroom. This process further eliminated the need for a planarization step making the whole fabrication approach considerably simpler. The

results of this considerable fabrication effort are the subject of this chapter. Designs for fabricated polarization rotators, splitters and splitter-rotators along with the unique fabrication process adopted, are presented. The structures were fabricated and characterized, and the measured results compared with rigorous electromagnetic simulations of the device designs. The devices are shown to be capable of broadband, high extinction, and low loss performance, but perhaps most importantly, they demonstrate significant tolerance to fabrication errors. Ultimately, the results of this fabrication effort demonstrate what was only surmised in the previous chapters, that is, mode-evolution is an extremely robust approach for manipulating polarization states on an integrated optic chip. While these results have recently been presented [31], this chapter represents a more comprehensive overview of the research.

4.1 Fabrication Approach

The approach for fabricating the two-layer polarization rotators and polarization splitters, developed by Tymon Barwicz and Minghao Qi, is depicted in Fig. 4-1. The process begins with thermal oxide growth (Fig. 4-1a) on a silicon wafer to form the under-cladding. Silicon rich silicon nitride (SiN) is then deposited via low-temperature chemical vapor deposition (Fig. 4-1b). Two hard-masks, one chromium (Cr) and one nickel (Ni) are then deposited and patterned with electron-beam lithography and lift-off (Fig. 4-1c). Alignment between the layers is then achieved by imaging the secondary electrons from alignment marks made in the Ni hard-mask. The first etch step which relies on the Ni hard-mask defines the wide splitter waveguide and the lower rotator waveguide layer. These waveguide patterns are transferred into the SiN via reactive-ion-etching and the Ni hard-mask is then selectively removed (Fig. 4-1d). The tall splitter waveguides and the upper core layer in the rotator are then formed via a second reactive ion etch which includes a slight over-etch into the SiO_2 underneath to ensure that the SiN is completely etched through (Fig. 4-1e). Without the protection of the Ni hard-mask, the second etch step serves to reduce the height of the lower core layer. The final step is the removal of Cr via wet-etch (Fig. 4-1f). This approach is very efficient in that it avoids the planarization and re-deposition steps required by traditional multi-layer fabrication.

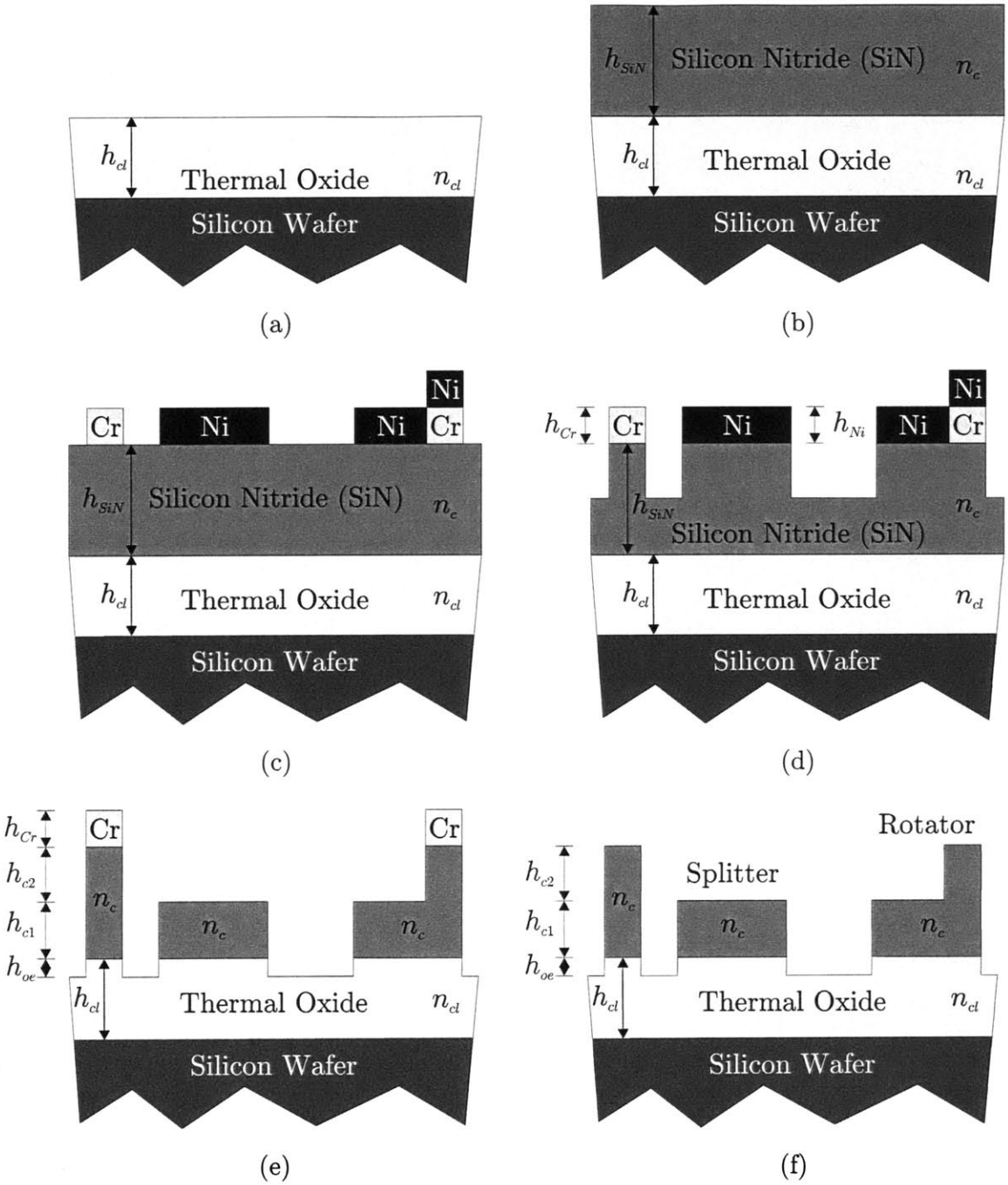

Figure 4-1: Fabrication approach developed by Minghao Qi and Tymon Barwicz for fabricating the two-layer polarization rotators, splitters, and splitter-rotators. Figures a-f detail the fabrication steps required to fabricate multilayer structures without the need for planarization. The steps are (a) silicon nitride deposition, (b) deposition and patterning of chromium and nickel hard masks, (c) etching of lower waveguide core layer, (d) removal of nickel hard mask, (e) etching of upper waveguide core layer, and (f) removal of the chromium hard mask. Representations of polarization splitter and rotator structures are depicted in the left and right sides of the sub-figures, respectively.

4.2 Fabrication of a Two-Layer Polarization Rotator

The fabrication approach depicted in Fig. 4-1 only lends itself to the fabrication of structures wherein the patterned upper core material sits directly on-top of the lower core material. Of the polarization rotators presented in Chapter 2, only the two-layer structure depicted in Fig. 2-7, fulfills this requirement. To further simplify the process, the structure is designed to operate without an upper cladding. The resulting device design is depicted in Fig. 4-2.

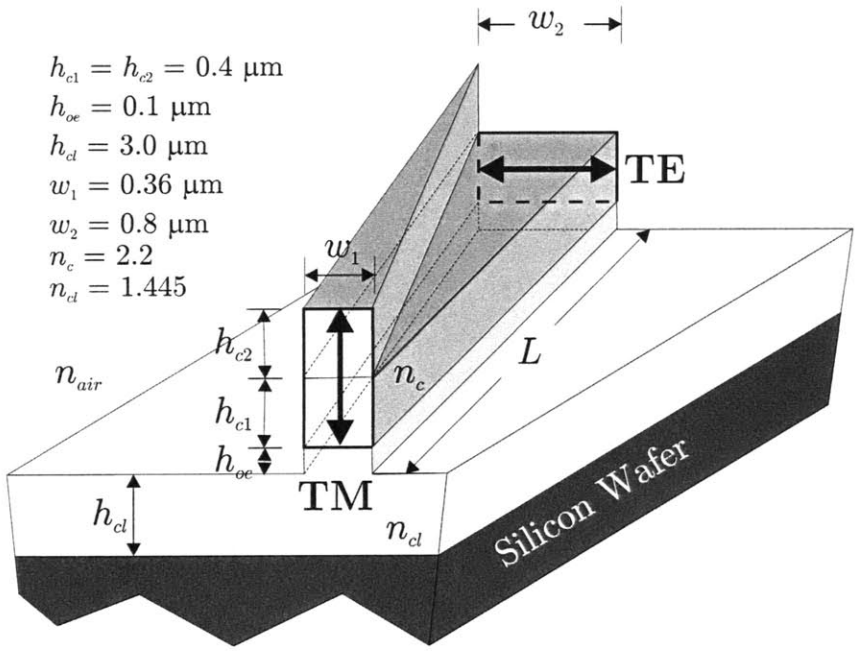

Figure 4-2: Two-layer polarization rotator design for fabrication the fabrication approach depicted in Fig. 4-1.

To determine an appropriate device length for fabrication, FDTD and EME simulations were performed as a function of the device length at a wavelength of $\lambda = 1.55\,\mu$m. The simulation results (Fig. 4-3a) indicate that efficient polarization rotation is possible for structures longer than $\sim 190\,\mu$m. The wavelength dependence obtained from a FDTD simulation of a $192\,\mu$m long structure is depicted in Fig. 4-3b. Here again little wavelength dependence is observed across the $1.45\,\mu$m to $1.75\,\mu$m band.

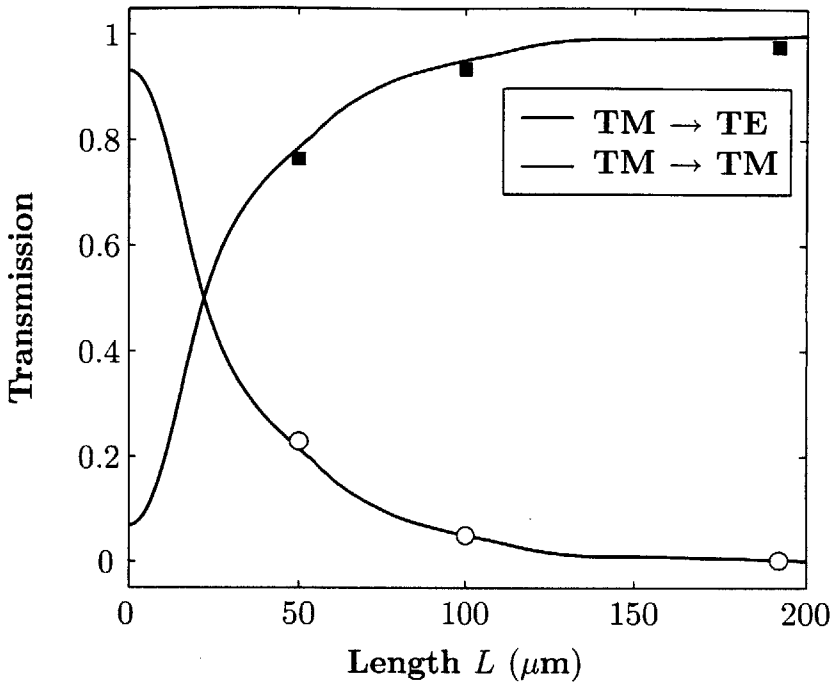

(a)

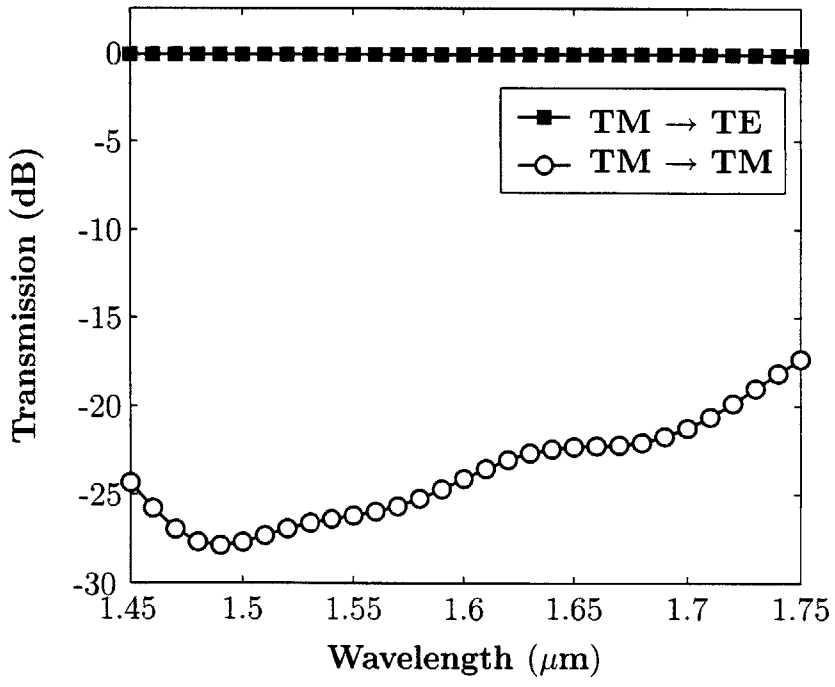

(b)

Figure 4-3: (a) FDTD (marked points) and EME simulations as function of length for a wavelength of $\lambda = 1.55\,\mu$m and (b) FDTD determined wavelength dependence for a 192μm long device for the polarization rotator depicted in Fig. 4-2.

Realistically, in fabrication the fine feature at the output of the structure may only be resolved to $\sim 100\,\text{nm}$. Before proceeding to fabrication it is necessary to consider the effect this will have on the performance of the device. A FDTD simulation of the junction, depicted in Fig. 4-4 indicates that the cross-talk induced by the junction is below $-24\,\text{dB}$ with the loss being less than $0.02\,\text{dB}$. Since this cross-talk is comparable to that seen in the ideal $192\,\mu\text{m}$ long device, if the resolution of the lithography system is in fact $100\,\text{nm}$, it is of little value to make longer structures with lower theoretical cross-talk values.

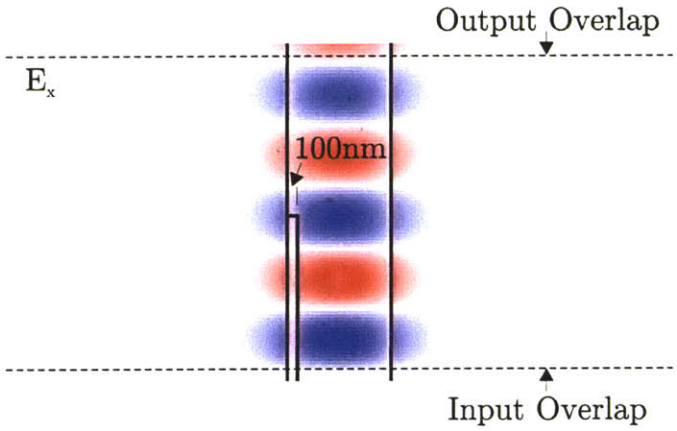

Figure 4-4: FDTD simulation modeling the junction formed by a realistic rotator output waveguide. The junction introduces less $-24\,\text{dB}$ cross-talk and less than $0.02\,\text{dB}$ loss.

The chip layout included a dozen polarization rotator implementations. Two device lengths, $192\mu\text{m}$ and $384\mu\text{m}$, were chosen despite the indications of the FDTD simulation results of Fig. 4-4, the idea being that it might be possible to achieve finer than $100\,\text{nm}$ linewidths. For each length two different input widths w_1 were chosen, $0.36\,\mu\text{m}$ and $0.378\,\mu\text{m}$, so as to determine the effect of guide width on device performance. Finally, three different layer alignments were chosen to minimize the impact of a e-beam stage drift. The basic device layout is depicted in Fig. 4-5 and the full list of device dimensions are listed in Table 4.1. Three sets of the twelve device implementations were fabricated by Minghao Qi using the process described in Section 4.1 and depicted in Fig. 4-1. The layer thicknesses used were $h_{cl} = 3\,\mu\text{m}, h_{SiN} = 820\,\text{nm}, h_{Cr} = 50\,\text{nm}, h_{Ni} = 50\,\text{nm}, h_{c1} = 410\,\text{nm}, h_{c2} = 410\,\text{nm}$, and $h_{oe} = 70\,\text{nm}$. The cladding thickness was specified and chosen to ensure negligible coupling to the substrate, but all other dimensions were measured using a profilometer. The core and cladding indices were measured to be $n_{cl} = 1.455$ and $n_c \approx 2.2$.

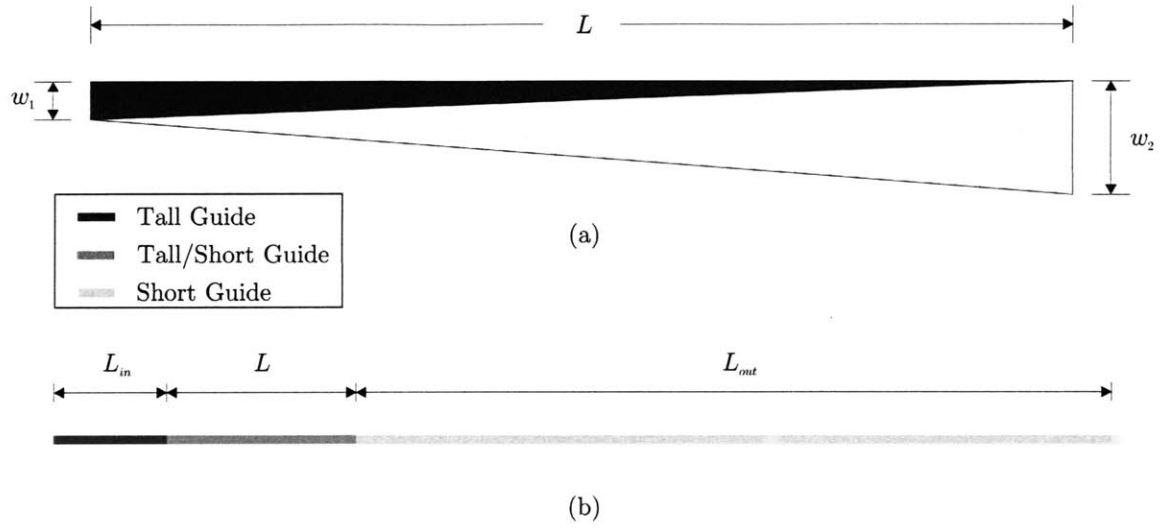

Figure 4-5: Layout (a) of the polarization rotator and (b) polarization rotator along with connecting input and output waveguides.

Device	L_{in}	L_R	L_{out}	w_1	w_2	δ
1	1300	384	2100	0.378	0.8	-0.048
2	1300	384	2100	0.378	0.8	0
3	1300	384	2100	0.378	0.8	0.048
4	1300	384	2100	0.36	0.8	-0.048
5	1300	384	2100	0.36	0.8	0
6	1300	384	2100	0.36	0.8	0.048
7	1300	192	2300	0.378	0.8	-0.048
8	1300	192	2300	0.378	0.8	0
9	1300	192	2300	0.378	0.8	0.048
10	1300	192	2300	0.36	0.8	-0.048
11	1300	192	2300	0.36	0.8	0
12	1300	192	2300	0.36	0.8	0.048

Table 4.1: The dimensions of the fabricated polarization rotators. All dimensions are in microns. Here δ is an offset introduced between the Ni and Cr hard-masks used to compensate for e-beam stage drift.

4.3 Polarization Rotator Characterization

The devices were characterized with a Santec tunable laser with a tuning range covering the $1510 - 1610\,\text{nm}$ wavelength span using the experimental setup depicted in Fig. 4-6. The output of the tunable laser was coupled to a single mode fiber and subsequently collimated, chopped, and focussed to a second single-mode fiber equipped with a standard paddle wheel based polarization controller and lensed fiber output. The paddle wheel based polarization controller enabled control of the input polarization to the chip while the lensed fiber improved coupling to the tightly confined waveguide modes. The lensed fiber and integrated optic chip sat on separate Melles-Griot piezo-electric controlled stages with nanometer alignment precision. Coarse alignment between the lensed fiber and waveguides on the chip was achieved visually through an imaging apparatus with a 20X magnification. Coupling to the chip was facilitated by imaging the output facet of the waveguide with a Vidicon infrared camera and visually inspecting the power exiting the waveguide. Once a substantial amount of power was coupled into the waveguide, the aperture radius was reduced to block light passing through the substrate and the flip-up mirror was repositioned to direct the light through the output analyzer (adjusted to accept and reject the appropriate polarizations) and onto the output detector. Fine control of the piezo-electric actuated stage holding the lensed fiber was then used to maximize the power incident on the detector. The chopper and lock-in amplifier served to minimize the impact of background light falling on the detector.

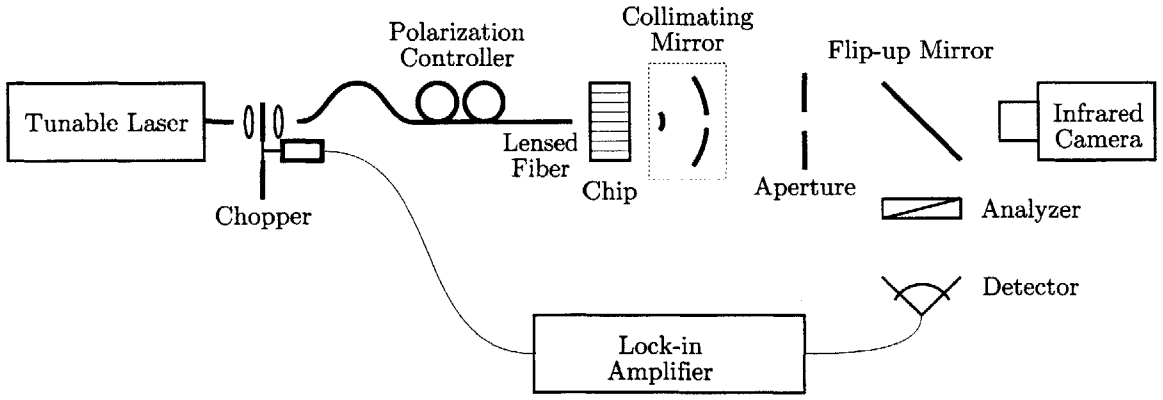

Figure 4-6: Experimental setup used to characterize the polarization rotator. The experimental setup was designed and built by Peter Rakich.

The raw measurements of the TE and TM components of the polarization rotator outputs are, by themselves, not especially revealing because the transmission characteristics of the experimental apparatus are mixed in with the measurement obscurring the transmission of the device itself. In order to extract the transmission T_R of the polarization rotator itself, it is necessary to consider all of the loss mechanisms impacting the measurement. Doing so, we write the detected current for the polarization rotator I_R as

$$I_R = P_L C_{T_{in}} T_{in} T_R T_{out} C_{W_{out}} R_d \tag{4.1}$$

where, P_L is the power of the laser used to characterize the device, $C_{T_{in}}$ is the input coupling coefficient, T_{in} is the transmission of the input waveguide, T_R is the transmission of the polarization rotator itself, T_{out} is the transmission of the output waveguide, $C_{W_{out}}$ is the output collection efficiency ($C^{TE}_{W_{out}}$ / $C^{TM}_{W_{out}}$ depending on polarization), and R_d is the responsivity of the detector. Rearranging (4.1) we get

$$T_R = \frac{I_R}{P_L C_{T_{in}} T_{in} T_{out} C_{W_{out}} R_d} \tag{4.2}$$

There are many parameters needed to determine the rotator transmission T_R, but by using the current I_{PClip} measured in a reference paperclip waveguide many of these parameters can be extracted rather easily. The current for the paperclip waveguide can be expressed in a similar manner

$$I_{PClip} = P_L C_{W_{in}} T_{PClip} C_{W_{out}} R_d \tag{4.3}$$

where the input coupling $C_{W_{in}}$ has changed because of the fact that the reference paperclip has dimensions corresponding to the wide output waveguide of the polarization rotator. Rearranging (4.3)

$$T_{PClip} = \frac{I_{PClip}}{P_L C_{W_{in}} C_{W_{out}} R_d} = \exp(-2\alpha_W L_{PClip}) \tag{4.4}$$

we find the transmission coefficient for the paperclip T_{PClip} which is also expressed in terms of the loss coefficient α_W for the waveguide. By dividing (4.4) by I_{PClip}, and inserting the

LHS of the resulting equation into (4.2), we get

$$T_R = \frac{T_{PClip}}{T_{in}T_{out}} \frac{C_{W_{in}}}{C_{T_{in}}} \frac{I_R}{I_{PClip}} \tag{4.5}$$

The coupling coefficients $C_{W_{in}}$ and $C_{T_{in}}$ can be approximated through simple mode overlap calculations between the lensed fiber mode and the corresponding input waveguide mode (i.e. $C_{ij} = \left|\frac{1}{2}\int \mathbf{e}_i \times \mathbf{h}_j \cdot dA\right|^2$). Doing so, we find $C_{W_{in}}^{TE} = 0.125$ and $C_{T_{in}} = 0.127$. The transmission of the paperclip waveguide is then calculated by comparing the transmission for waveguides of different lengths.

Paperclip waveguides with lengths of 4.0 mm, 5.6 mm and 7.2 mm were fabricated and characterized. The 4.0 mm paperclip had a damaged end facet, however, the remaining two provided clean results. The loss in dB/cm for the TE and TM polarizations of the paperclip waveguide are presented in Fig. 4-7. The transmission of the output waveguide T_{out} for each polarization is then readily determined leaving the transmission of the input waveguide as the only remaining unknown quantity. While paperclip waveguides for the tall waveguide were not fabricated, the geometry of the tall guide is nearly a rotated version of the output waveguide. Therefore, if the losses in the guide are due to bulk absorption or scattering they should be nearly identical to the losses of the TE mode of the wide output waveguide. By calculating T_{in} in this manner, and inserting the result into (4.5), we should obtain a lower bound for the transmission of the polarization rotator.

The twelve polarization rotators on Chip 1 were fully characterized and normalized according to (4.5) and the results are plotted in Fig. 4-8 and Fig. 4-9. Nearly all of the fabricated devices exhibited extinctions of greater than 10 dB for the un-rotated TM to TM component across the 100 nm bandwidth of the tunable laser.[†] The highest extinction is found in rotator R4. Taking into account the artificially high cross-talk level caused by the interference of the TE and TM output components, the extinction demonstrated by rotator R4 is $\sim$ 20 dB across the band. The normalized curves indicate that most of the devices are nearly lossless at the short wavelength end.

Despite the impressive measured performance, most of the devices fell short of their

[†]The modulation in the TM to TM component observed in all of the measurements is a due to an inability to perfectly isolate the TM output from the TE output. The the two components travel different optical distances causing a beat signal to be produced across the band. Thus, the actual TM output level is up to 3 dB below the interference maxima.

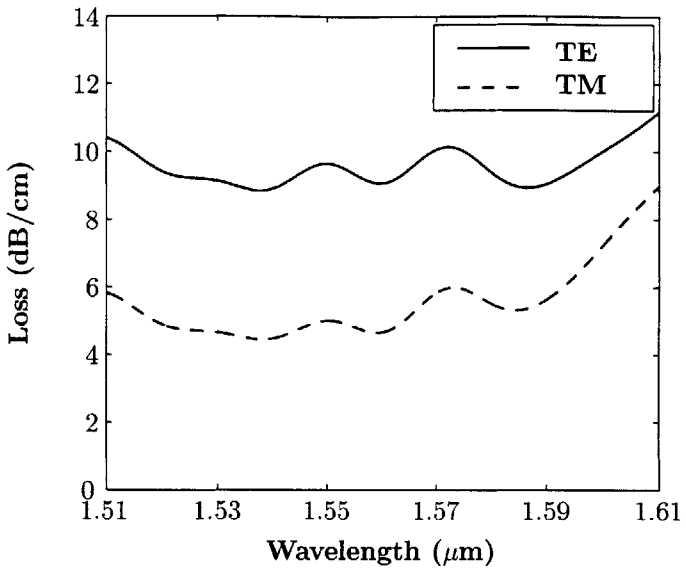

Figure 4-7: Losses for the TE and TM modes of the wide output waveguide of the polarization rotator as a function of wavelength as determined from differential length paperclip waveguides. Note: The high frequency components resulting from Fabry-Perot effects were removed using a fast Fourier transform of the data.

theoretical potential (Fig. 4-3). To determine the cause of the discrepancy in performance, the fabricated devices were inspected. Scanning electron micrographs (SEMs) of a representative fabricated device are depicted in Fig. 4-10a and Fig. 4-10b which show the input waveguide facet and rotator output end, respectively. Fig. 4-10a shows that the tall waveguide has only a minor sidewall slope and Fig. 4-10b demonstrates that the minimum feature size achieved was below the 100 nm goal. Given the fine features that were achieved, it seems unlikely that the output end limited the device performance.

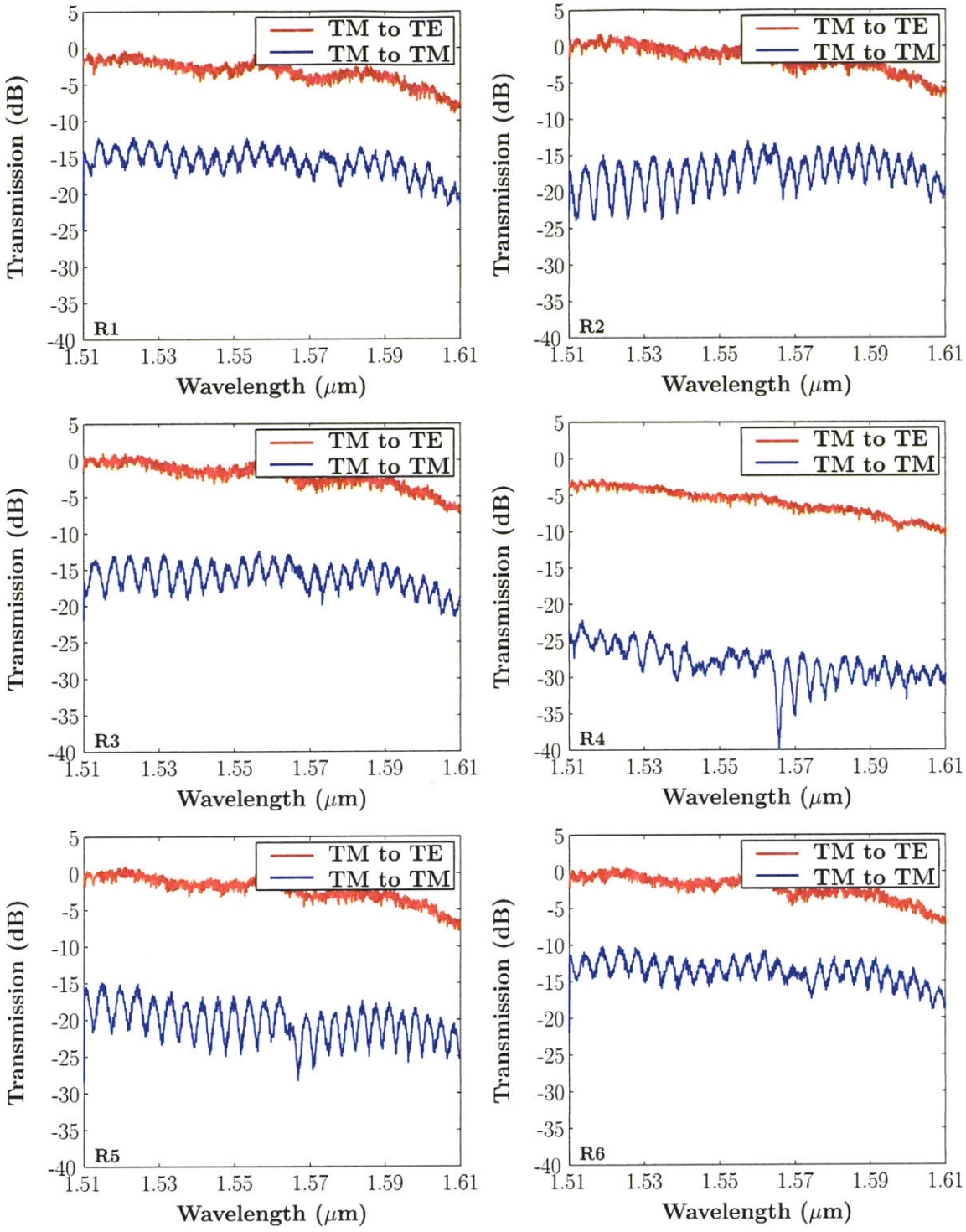

Figure 4-8: Measured performance of the two-layer polarization rotator depicted in Fig. 4-2. Rotators R1, R2, and R3 are all 384 μm long and have device widths 0.378 μm. Rotators R4, R5, and R6 are also 384 μm long but have device widths 0.36 μm. R1 and R4 have a -48 nm bias to the top layer alignment, R2 and R5 have no bias, and R3 and R6 have $+48$ nm bias to the top layer alignment.

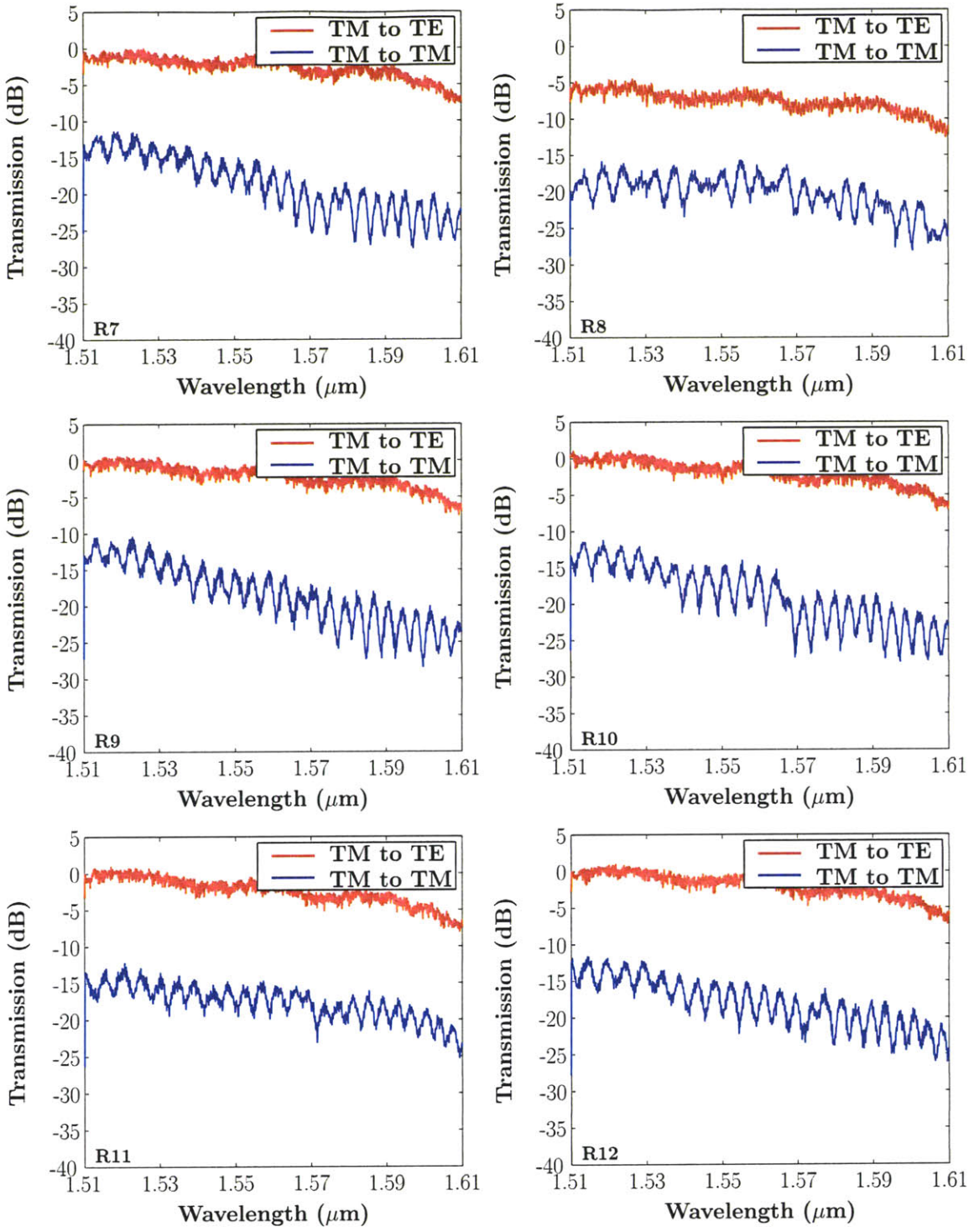

Figure 4-9: Measured performance of the two-layer polarization rotator depicted in Fig.4-2. Rotators R7, R8, and R9 are all 192 μm long and have device widths 0.378 μm. Rotators R10, R11, and R12 are also 192 μm long but have device widths 0.36 μm. R7 and R10 have a -48 nm bias to the top layer alignment, R8 and R11 have no bias, and R9 and R12 have $+48$ nm bias to the top layer alignment.

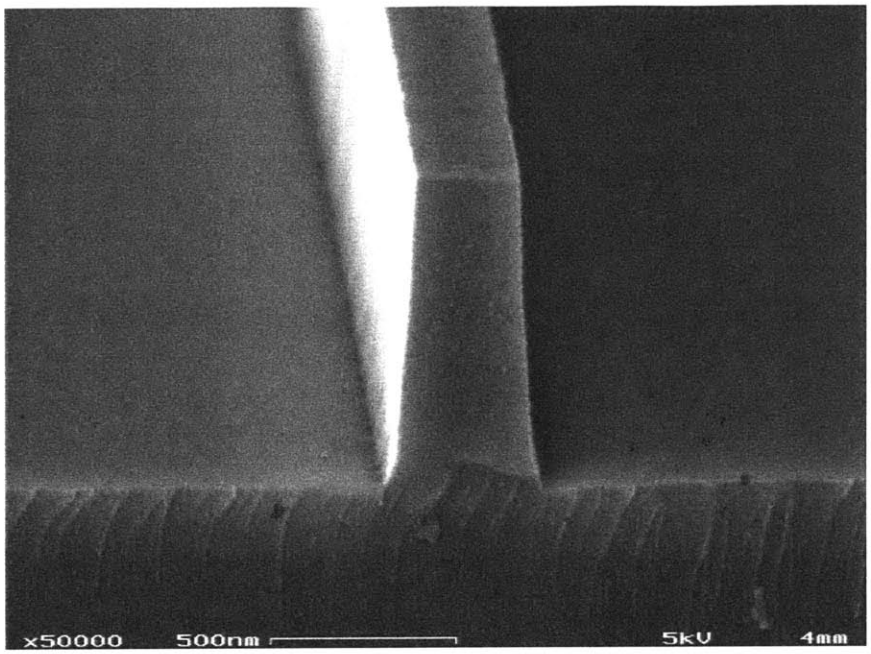

(a)

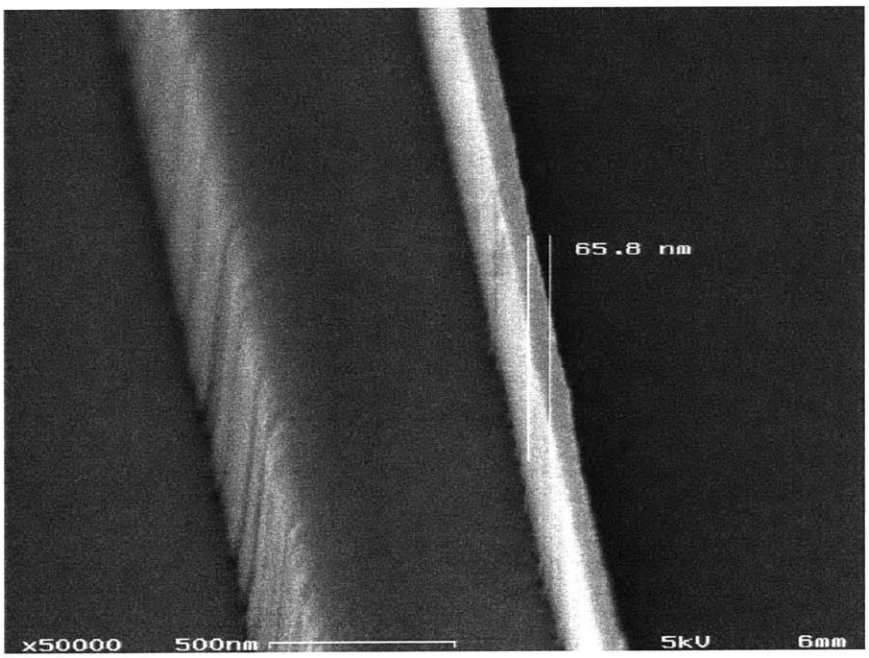

(b)

Figure 4-10: (a) Scanning electron micrograph (SEM) of a fabricated two-layer polarization rotator input facet, and (b) a close-up of the output end of a fabricated polarization rotator. Dimensions are approximate. Micrographs taken by Minghao Qi.

The SEMs in Fig. 4-10 only provide coarse estimates of the guide dimensions. To more accurately determine what may have caused the discrepancy in the device performance, we made some calibrated measurements of the devices using the Raith 150 e-beam lithography system in the measure mode. The input and output junctions of rotators R4 and R9 were measured and their dimensions are as indicated in Fig. 4-11. Both devices have highly irregular input waveguides. The input waveguide and the device input are offset by $160 - 170\,\text{nm}$ and separated by $\sim 80\,\text{nm}$. Additionally, it appears that the lower core layer is considerably wider than the upper core layer in both guides. This lower core region is also offset from the upper core layer with the offset being larger in rotator R9. SEMs of the output waveguide cross-sections are also shown. Both devices show imperfect output waveguides, with the output of R4 showing some damage and that of R9 indicating an unintended offset for the upper core layer. Also, both output guides are considerably wider ($\sim 1000\,\text{nm}$) than the design (800 nm).

To determine the effects of these fabrication errors, post fabrication simulations of these structures were performed. The L-like shape of the rotator input waveguides rotates the polarization states of the fundamental and secondary guided modes leading to cross-talk at the input junction. FDTD simulations of the input sections (Fig. 4-11d, left) indicate that in rotator R4, the induced cross-talk is $-15.6\,\text{dB}$ while in rotator R9 the cross-talk is $-11\,\text{dB}$. The slightly smaller offset in R4 is responsible for the lower cross-talk. The device cross-talks should be limited by the calculated amounts. Yet, the measured results indicate performance that is in fact better than that predicted by the simulations. This could be because the secondary guided mode is only weakly guided and may be coupling to the substrate resulting in polarization dependent loss thereby improving the extinction ratio. The rotator output ends are also highly imperfect. While the rotator R4's output is difficult to simulate, an FDTD simulation of R9's output end (Fig. 4-11c, right) indicates that the cross-talk introduced in rotator R9 by the output end is below $-29\,\text{dB}$, clearly implicating fabrication errors at the input end as the cause for reduced extinction. As a final note, in both cases the poorly aligned coupling region leads to $\sim 2.6\,\text{dB}$ loss which calls into question the normalization of the data. Most devices show little to no loss at the short wavelength end which cannot be accurate. It is possible that the wavelength dependence of the tall input waveguide is the cause of the imperfect normalization.

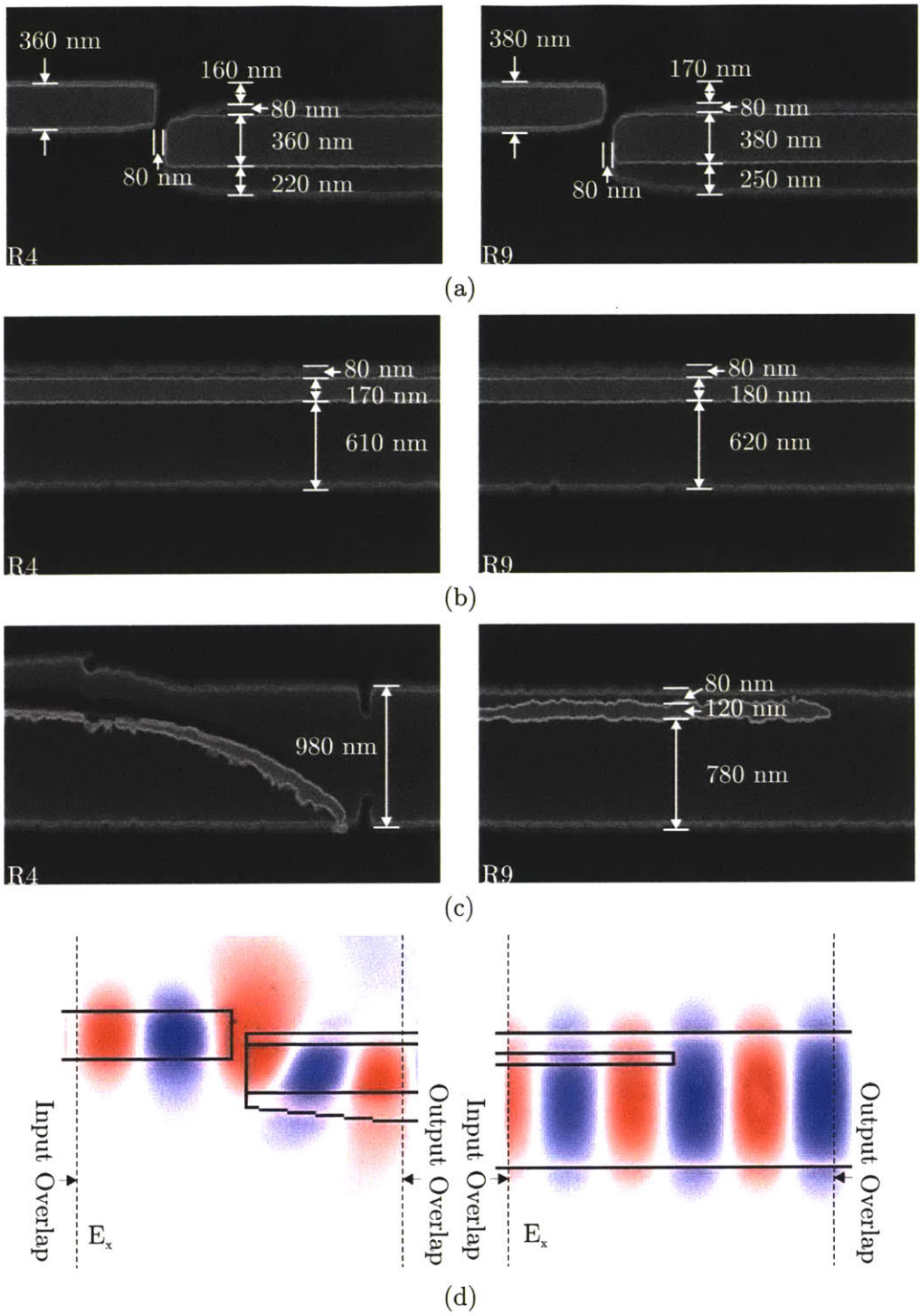

Figure 4-11: SEM images of the input and output ends of polarization rotators (a) R4 and (b) R9 along with (c) field plots of FDTD simulation results of the input (left) and output (right) ends. The simulations indicate that fabrication errors on the input end cause -15.6 dB and -11 dB cross-talk in rotators R4 and R9, respectively, and 2.6 dB loss in each device. Micrographs taken by Minghao Qi.

4.4 Fabrication of Two-Layer Polarization Splitters

The polarization splitter was designed to use the same layer set as the polarization rotator so that it could be fabricated in the same run and integrated to form a polarization splitter-rotator. The fabricated device design is depicted in Fig. 4-12.

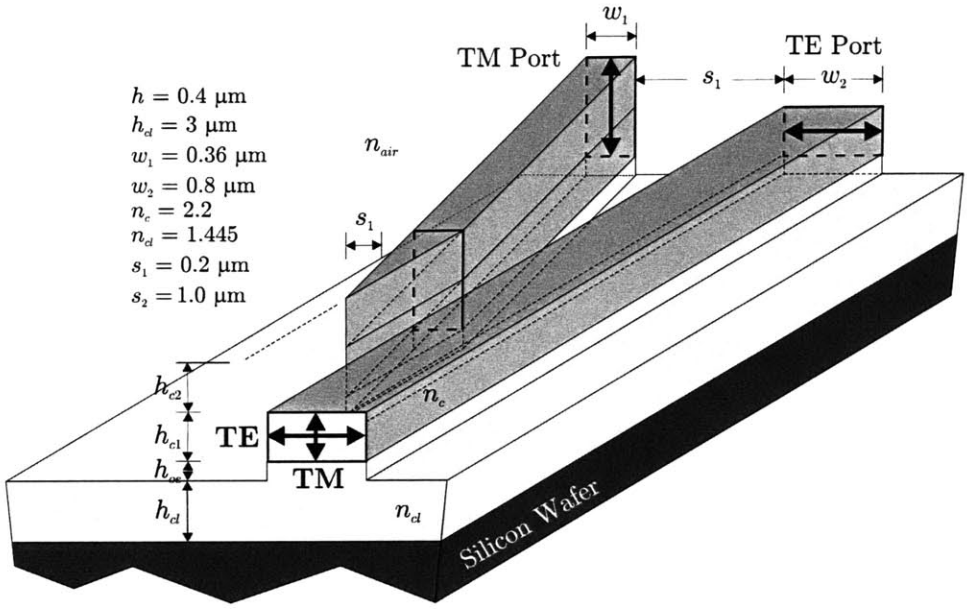

Figure 4-12: The fabricated polarization splitter design

The design is a modified version of the two-layer splitter presented in Chapter 3. The dimensions, listed in Fig. 4-12, are nominally the same with the primary difference being the lack of an upper cladding. To verify the performance of the device, the structure was simulated using FDTD and EME codes. The results as a function of device length are presented for a wavelength of $\lambda = 1.55\,\mu$m in Fig. 4-13a. The wavelength dependence for a $242\,\mu$m long device obtained from a DFT taken during the FDTD simulation is presented in Fig. 4-13b. Here again, the device exhibits low cross-talk over the $1.45 - 1.75\,\mu$m band. On account of the lack of an upper cladding, there is no guided secondary TE (i.e.TE_{21}) mode and thus no TE cross-talk component.

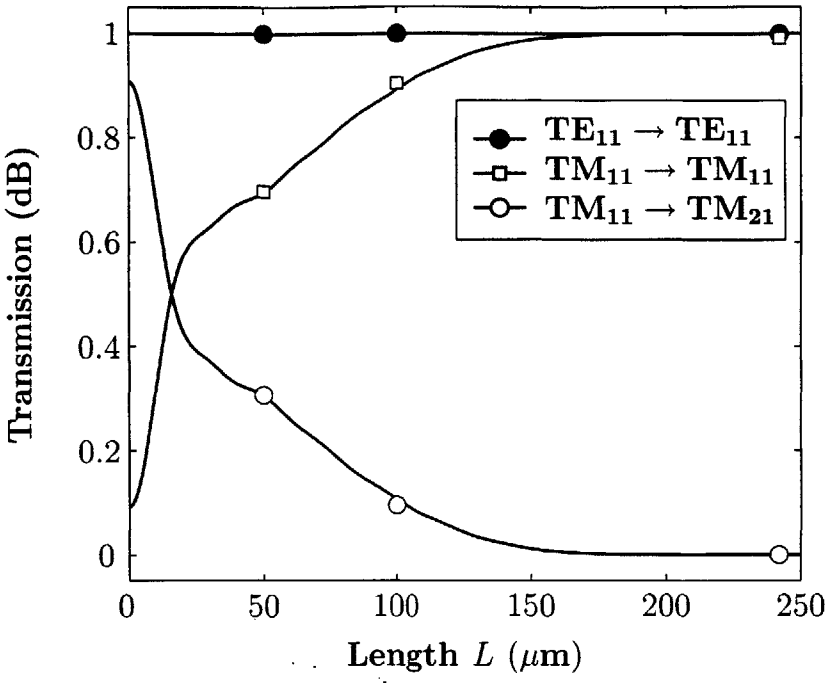

(a)

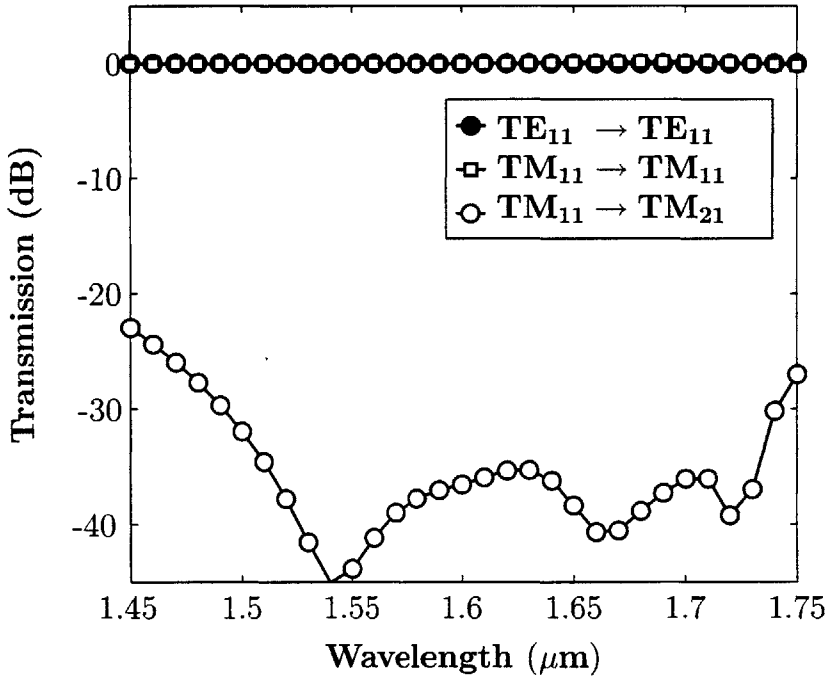

(b)

Figure 4-13: a) FDTD (marked points) and EME expansion results as a function of the device length for a wavelength of $\lambda = 1.55\,\mu$m, and (b) FDTD results for a $242\,\mu$m long device as a function of wavelength. The simulation results are for the device depicted in Fig. 4-12.

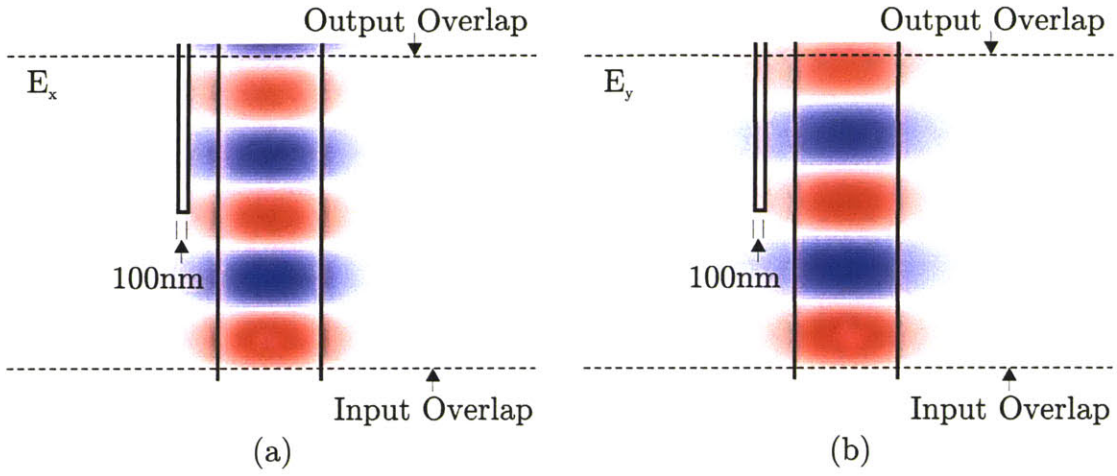

Figure 4-14: FDTD simulation of the junction formed by a realistic splitter input waveguide for the (a) TE and (b) TM cases. The junction induces less 0.0025 dB and 0.02 dB loss for the TE and TM case, respectively, and no appreciable cross-talk.

Of course, like the polarization rotator, the fine feature in the polarization splitter may not be resolved to a width less than 100 nm. To determine the impact of the finite initial width of the tall waveguide on the device performance, I ran a FDTD simulation on the junction left by this feature. The simulations, depicted in Fig. 4-14 indicate that the $TE_{11} \rightarrow TM_{11}$ induced cross-talk is below -45 dB and the loss experienced by the TE_{11} mode is below 0.0025 dB with the loss experienced by the TM_{11} mode below 0.02 dB across the band. There is no $TM_{11} \rightarrow TM_{21}$ induced cross-talk because the TM_{21} mode is not guided at this point along the transition. The simulations demonstrate that a 100 nm linewidth has little impact on performance.

The layout of the structure on the integrated optic chip is depicted in Fig. 4-15. Three copies of twelve different device implementations were fabricated. Variations were made in the tall waveguide width w_1, the initial separation between the guides s_1, and the length of the device L. The full table of dimensions is presented in Table 4.2. As was discussed in Section 3.2, the width of the tall waveguide critically affects the $\overline{\delta\beta}$ between the TM_{11} and TM_{21} modes. By making multiple widths of the tall waveguide, two things can be accomplished at once: (1) the sensitivity to width variations can be investigated in an actual structure, and (2) the probability that the desired width is achieved is enhanced. The widths chosen for the e-beam write were the desired width of 0.36μm and a slightly larger width

of 0.378μm. The initial separation s_1 also impacts the TM mode splitting, with smaller separations providing higher degrees of mode splitting and improved device performance. However, a fusing of the guides would likely lead to a non-adiabatic transition limiting device performance. To achieve the appropriate balance between these effects, multiple initial separations s_1 of 0.162μm, 0.198μm, and 0.234μm were chosen to compensate for the known drift in the e-beam stage. Finally, two different lengths $L = 242\mu$m and $L = 484\mu$m were chosen. Theoretically the longer devices should perform better. Again, the twelve device implementations were fabricated on three separate chips by Minghao Qi.

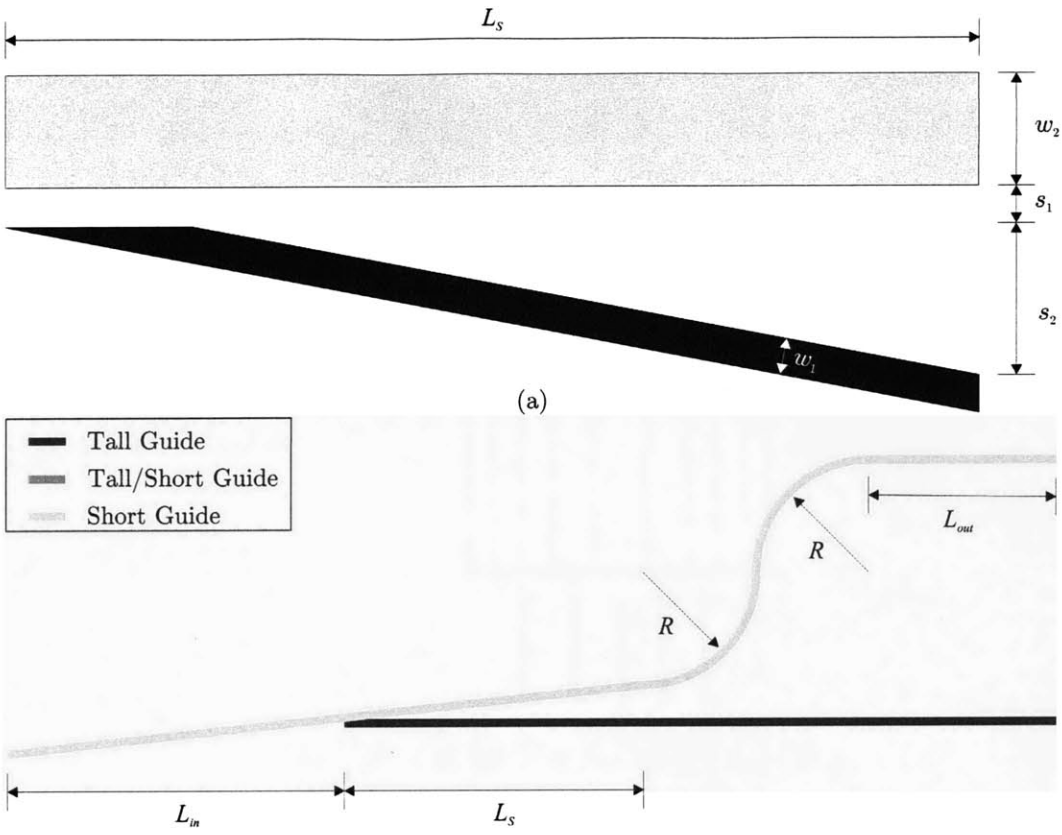

Figure 4-15: Splitter layout on the integrated optic chip

Device	L_{in}	L	L_{out}	w_1	w_2	s_1
1	1600	484	1700	0.378	0.8	0.234
2	1600	484	1700	0.378	0.8	0.198
3	1600	484	1700	0.378	0.8	0.162
4	1600	484	1700	0.36	0.8	0.234
5	1600	484	1700	0.36	0.8	0.198
6	1600	484	1700	0.36	0.8	0.162
7	1700	242	1950	0.378	0.8	0.234
8	1700	242	1950	0.378	0.8	0.198
9	1700	242	1950	0.378	0.8	0.162
10	1700	242	1950	0.36	0.8	0.234
11	1700	242	1950	0.36	0.8	0.198
12	1700	242	1950	0.36	0.8	0.162

Table 4.2: The chosen dimensions for the fabricated polarization splitters. The input and output waveguide lengths are approximate. All dimensions are in microns.

4.5 Polarization Splitter Characterization

The polarization splitters were characterized using the experimental setup depicted in Fig.4-6. The input polarization was aligned to a TM input by adjusting the input polarization controller until the power emanating from the horizontally oriented waveguide was minimized. The power emanating from the vertically oriented waveguide was then imaged onto the detector and the laser wavelength was subsequently scanned across the $1.51 - 1.61\,\mu$m band while the current $I_{S_{TM}}$ was recorded with the output analyzer aligned to accept the TM polarization. The power emanating from the vertically oriented output waveguide was then minimized by adjusting the polarization controller therein ensuring maximal TE input. The power emanating from the horizontally oriented waveguide was then imaged onto the detector and again the laser wavelength was scanned across the $1.51 - 1.61\,\mu$m band while the current $I_{S_{TE}}$ was recorded with the output analyzer aligned to accept a TE polarization. Cross-talk levels were recorded in an analogous manner.

The data was normalized in a manner quite similar to the approach taken for the polarization rotators. The detected current at the TE input port $I_{S_{TE}}$ is written as

$$I_{S_{TE}} = P_L C_{W_{in}} T_{in} T_{S_{TE}} T_{out} C_{W_{out}} R_d \tag{4.6}$$

where, P_L is the power of the laser used to characterize the device, $C_{T_{in}}$ is the input coupling coefficient, T_{in} is the transmission of the input waveguide, $T_{S_{TE}}$ is the transmission for the TE port of the polarization splitter, T_{out} is the transmission of the output waveguide, $C_{W_{out}}$ is the output collection efficiency, and R_d is the responsivity of the detector. Rearranging (4.6) we get

$$T_{S_{TE}} = \frac{I_{S_{TE}}}{P_L C_{W_{in}} T_{in} T_{out} C_{W_{out}} R_d} \tag{4.7}$$

Here again, by using the measured current I_{PClip} and transmission of a reference paperclip waveguide, we can express (4.7) as simply

$$T_{S_{TE}} = \frac{T_{PClip}}{T_{in} T_{out}} \frac{I_{S_{TE}}}{I_{PClip}} \tag{4.8}$$

Similarly, the expressions for the vertically oriented output can be written as

$$T_{S_{TM}} = \frac{I_{S_{TM}}}{P_L C_{W_{in}} T_{in} T_{out} C_{T_{out}} R_d} \tag{4.9}$$

and by again using (4.3), (4.9) can be expressed as

$$T_{S_{TM}} = \frac{T_{PClip}}{T_{in}T_{out}} \frac{C_{W_{out}}}{C_{T_{out}}} \frac{I_{S_{TM}}}{I_{PClip}} \tag{4.10}$$

The loss in dB/cm for the TE and TM polarizations of the paperclip waveguide are presented in Fig. 4-7. The transmission of the output waveguide T_{out} for each polarization is then readily determined. To determine the approximate difference in the collection efficiencies for each mode, the far field of each was calculated and overlapped with aperture of the collimating mirror. The collimating mirror objective has a numerical aperture of 0.4 and a second mirror that blocked the central 16.7% of the mirror aperture area. For the TE and TM modes, the calculated collection efficiencies are 22.8 % and 29.8 % for the wide waveguide and 23 % for the tall waveguide. Using equations (4.8) and (4.10), the measured responses of the polarization splitters were normalized and the results for the polarization splitters on chip 1 are presented in Fig. 4-16. On Chip 1, only polarization splitters S3, S6, S9,and S12 were fully characterized because the rest of the devices were qualitatively deemed of too low performance to be useful. As observed in Fig. 4-16, the extinction ratios of the polarization splitters on Chip 1 were all $\sim$ 10 dB and therefore short of the predicted performance.

To determine the cause of the imperfect extinction, the device geometry was inspected. Scanning electron micrographs (SEMs) of a representative polarization splitter input and output are depicted in Fig. 4-17a and Fig. 4-17b, respectively. The marked dimensions are approximate but they detail a couple of important features. First, Fig. 4-17a indicates that the desired 100 nm resolution was achieved. However, the separation between the wide and tall waveguides appears to be larger than the design (200 nm). And, both Fig. 4-17a and Fig. 4-17b indicate that the width w_2 of the wide waveguide is significantly larger (949nm and 988nm) than the design specification (800nm) while Fig. 4-17b also indicates that the width w_1 of the output tall waveguide is substantially smaller (330nm) than the design specification (360nm). To confirm these measurements calibrated measurements were made on the input and near the output of a pair of polarization splitters. The devices chosen for measurement were splitters S10 and S12 of Chip 1. The measurement results presented in Fig. 4-18. The calibrated SEMs confirm that the initial separation s_1 and and guide width w_2 were both considerably larger than the design specifications although they indicate that

the tall waveguide width w_1 was close to that specified.

The increased width w_2 of the wide waveguide causes the TM_{21} mode to be more confined thereby increasing its effective index and causing the guided TM modes (TM_{11} and TM_{21}) modes to propagate at much more similar rates (i.e. exhibit a much smaller $\overline{\delta\beta}$) than was called for in the design. The smaller $\overline{\delta\beta}$, naturally leads to more power exchange between the modes thereby limiting the extinction of the TM component in the TE Port. Additionally, the larger than expected initial separation between the guides further reduces the splitting between the guided TM modes. Confirmation of the importance of the initial separation is the fact that Splitters S3, S6, S9, and S12 were the best performing devices on Chip 1, devices that all have the smallest initial design separations in their device sets. Evidence that the smaller design separations in fact led to smaller realized separations is provided by the comparison in the separations of devices S10 and S12 in Fig. 4-18.

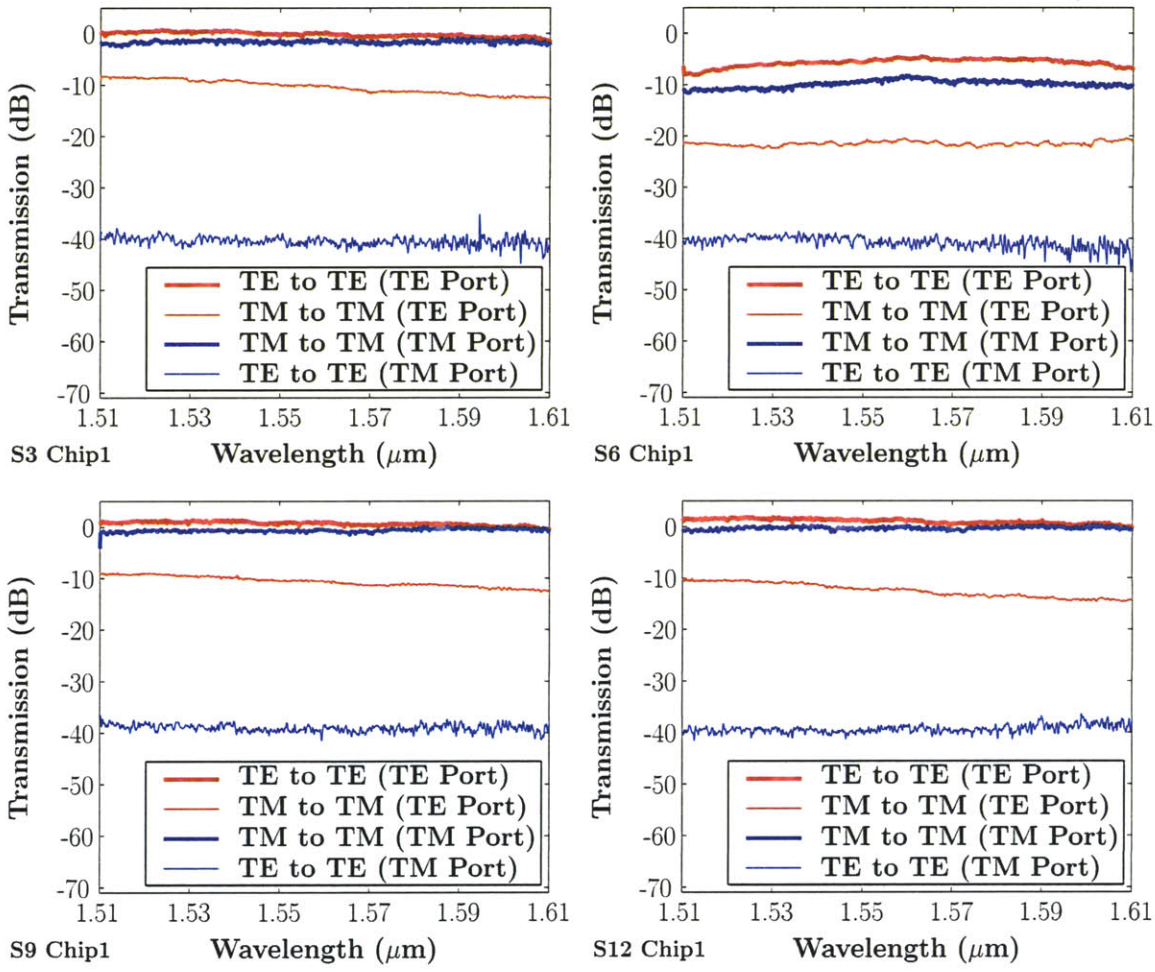

Figure 4-16: Measured performance of the two-layer polarization splitter depicted in Fig. 4-12. Measured data for splitters S1, S2, S9, and S12 on Chip 1 are shown.

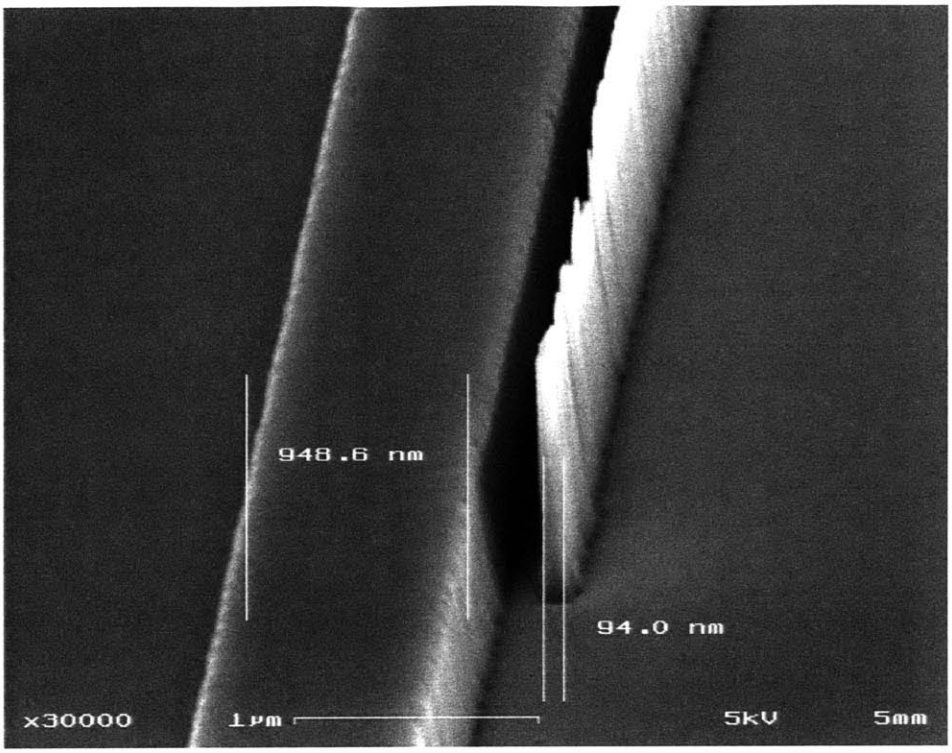

(a)

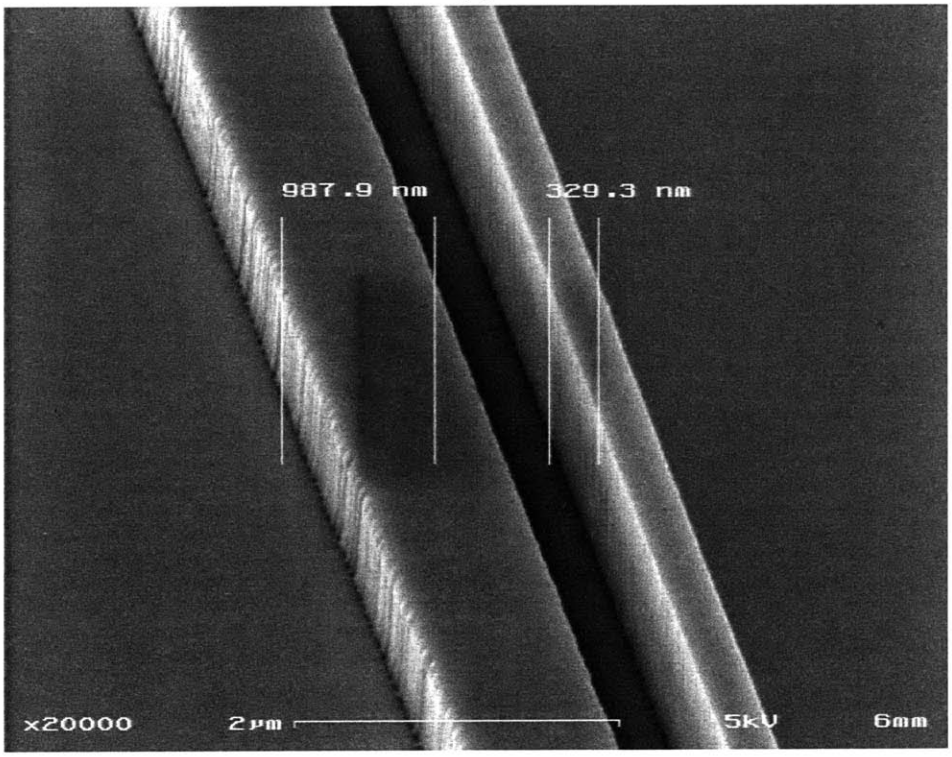

(b)

Figure 4-17: SEM showing (a) the input to and (b) mid-way along a representative polarization splitter. Dimensions are approximate. Micrograph taken by Minghao Qi.

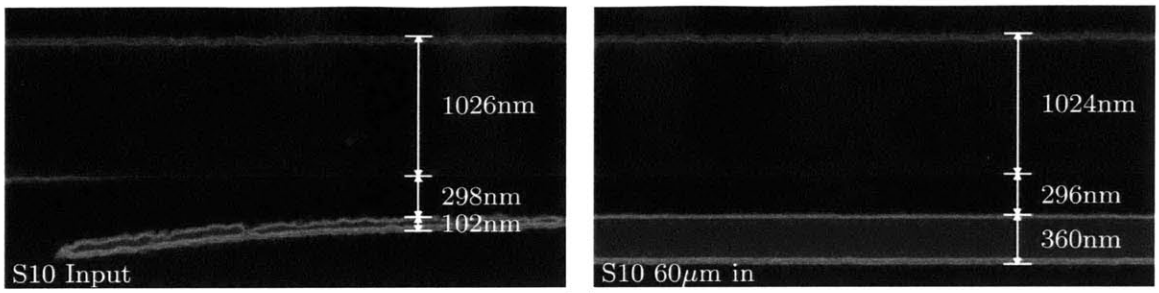

(a)

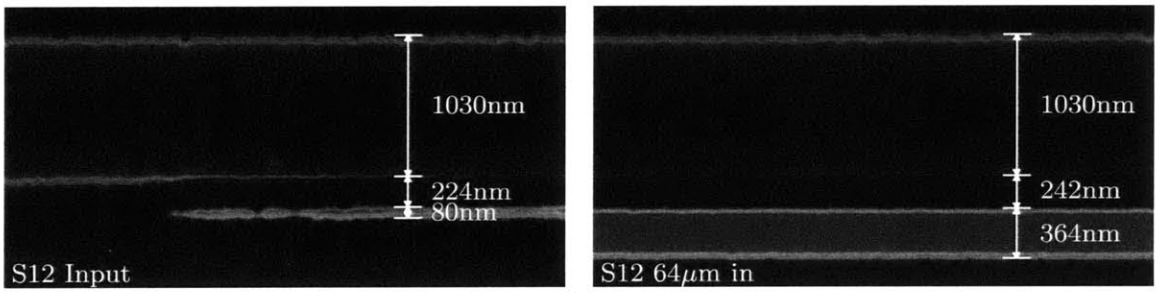

(b)

Figure 4-18: Calibrated SEMs of polarization splitters (a) S10 and (b) S12. The larger than expected wide waveguide width w_2 and initial separation s_1 is the cause of their poor measured extinction ratios. Micrographs taken by Minghao Qi.

Given the poor performance of the devices on Chip 1, the devices on Chip 2 were characterized in the hope of finding some higher performing devices. This second set of polarization splitters exhibited much better extinction. The results for some of the polarization splitters on Chip 2 are presented in Fig. 4-19.[‡] The polarization splitters on Chip 2 performed quite well achieving greater than $> 22\,\text{dB}$ extinction in 4 out of the 5 characterized devices across the 100 nm tuning range of our laser.

[‡]Due to e-beam stage drift the input and output connecting waveguides were often not attached to the device outputs. On account of the narrower waveguide width, higher losses were observed in the TM output port. Devices that were severely affected were not characterized.

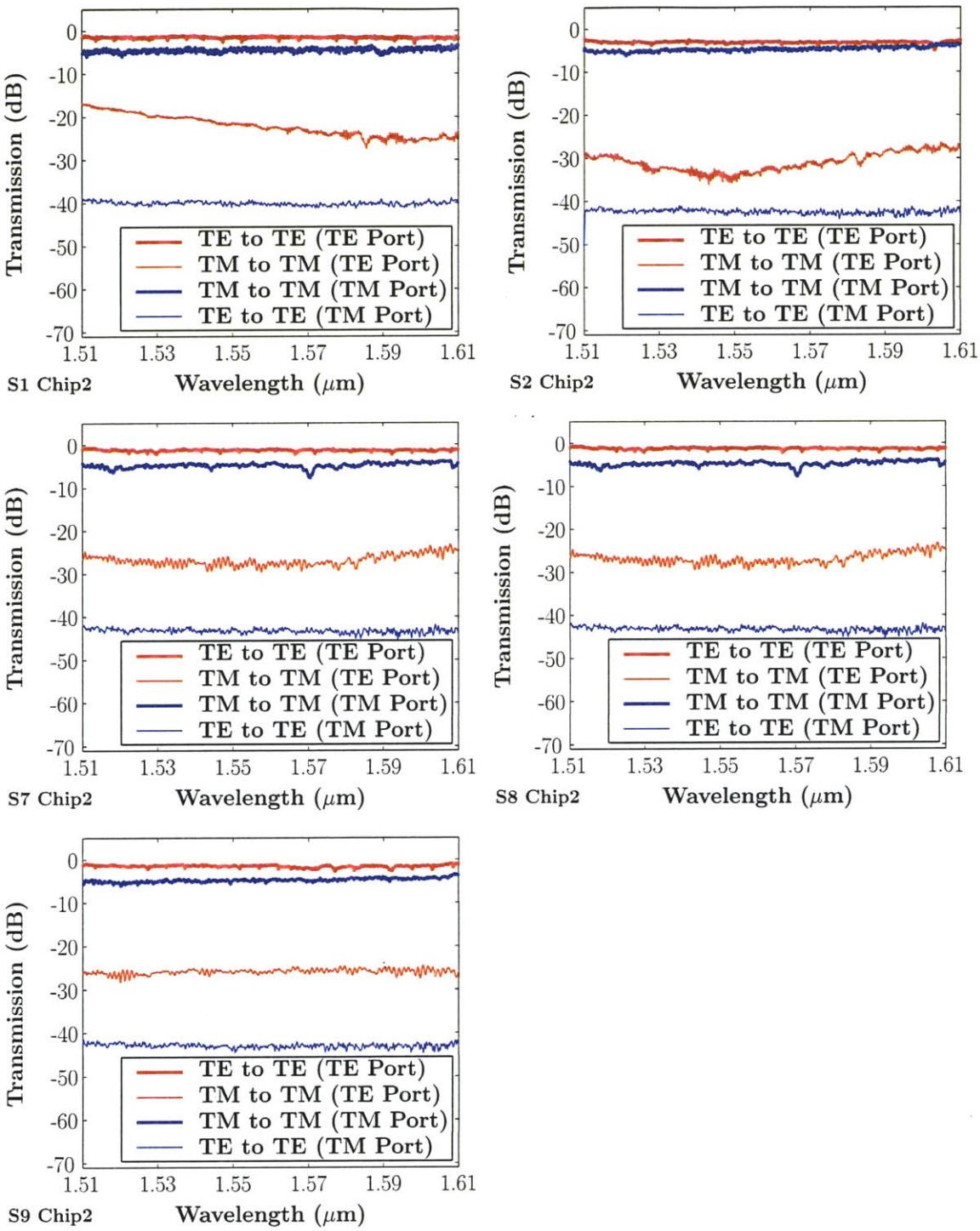

Figure 4-19: Measured performance of the two-layer polarization splitter depicted in Fig. 4-12. Measured data for splitters S1, S2, S7, S8, and S9 on Chip 2 are shown.

4.6 Fabricated Polarization Splitter-Rotators

Finally, the polarization rotator and polarization splitter of the previous sections were combined to form an integrated polarization splitter rotator (Fig. 4-20).

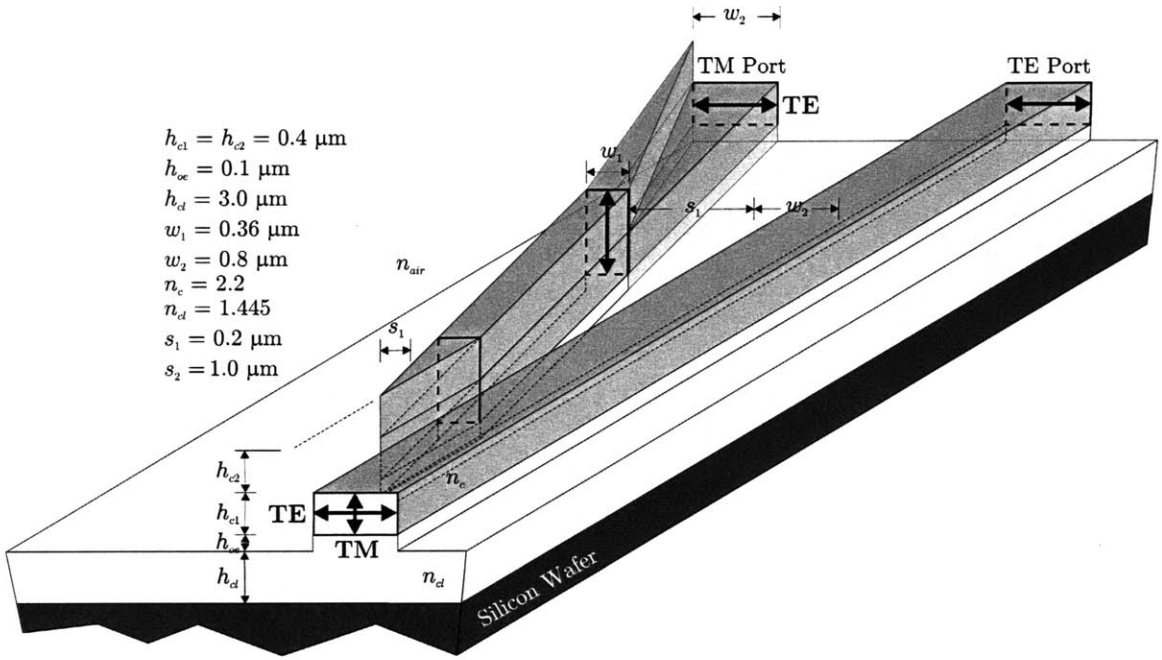

Figure 4-20: Fabricated polarization splitter-rotator design

The chip layout and dimensions are shown in Fig. 4-21 and Tab. 4.3. Again, three copies of the twelve device implementations were fabricated by Minghao Qi in the same fabrication run and on the same chips as the polarization splitters and rotators of the previous sections. The two variations in the device lengths for the splitters and rotators were combined to form long ($\sim 800\,\mu$m) and short ($\sim 400\,\mu$m) polarization splitter-rotator implementations. Also, multiple polarization splitter and rotator widths and rotator layer alignments were used.

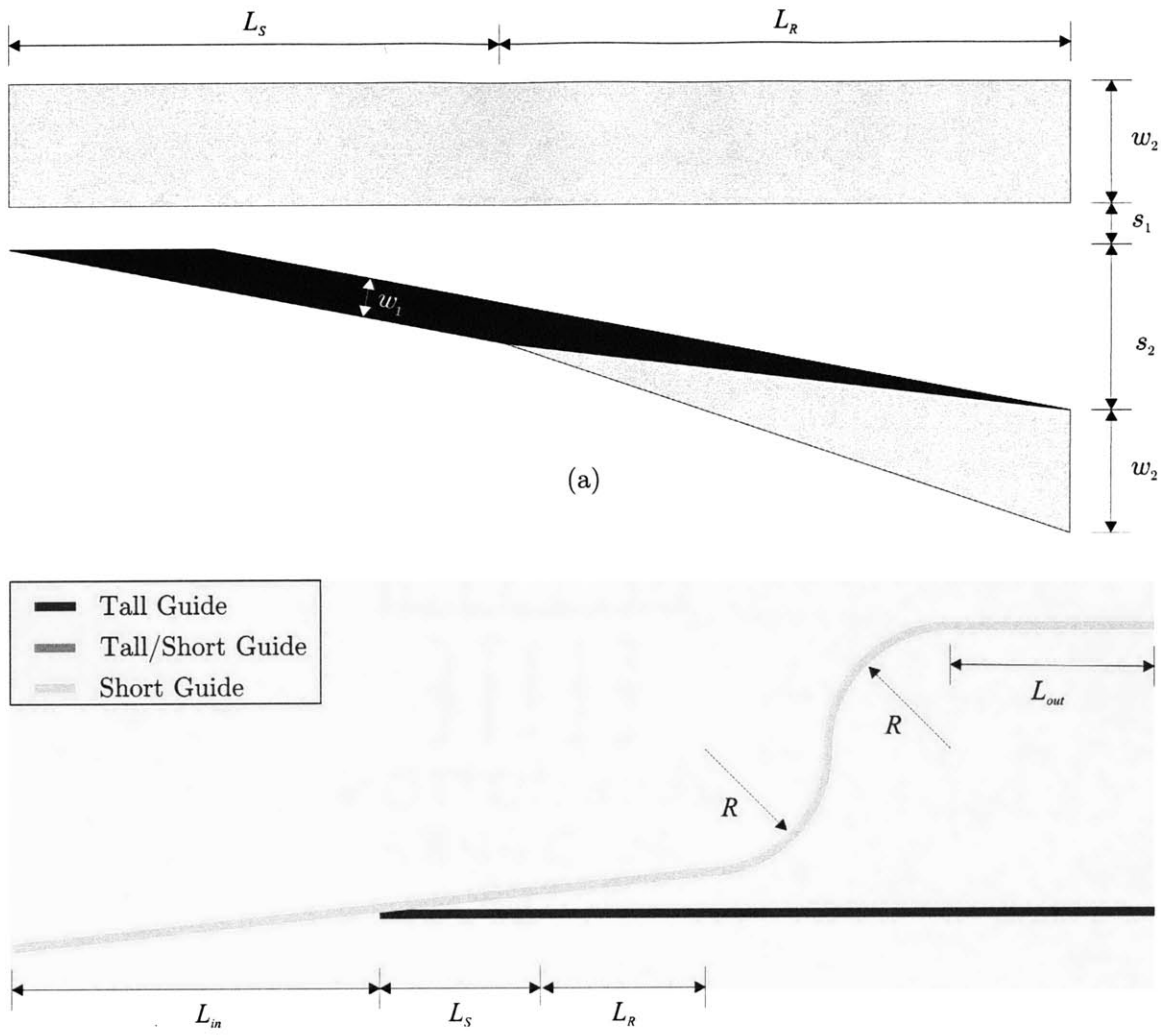

Figure 4-21: Polarization splitter-rotator layout on the integrated optic chip.

The polarization splitter-rotators were characterized using the experimental setup depicted in Fig. 4-6. Here again, the input polarization was aligned to be TM by adjusting the input polarization controller until the power emanating from the TE output port was minimized, ensuring maximal TM input. The power emanating from the TM output port was then imaged onto the detector and the laser wavelength was subsequently scanned across the 1.51μm to 1.61μm band while the current $I_{PSR_{TM}}$ was recorded. The power emanating from the TE output port was then imaged onto the detector and here again the laser wavelength was then scanned across the 1.51μm to 1.61μm band while the current $I_{PSR_{TE}}$ was recorded. Cross-talk levels were measured in an analogous manner.

Device	L_{in}	L_S	L_R	L_{out}	w_1	w_2	δ
1	1200	484	384	1730	0.378	0.8	-0.048
2	1200	484	384	1730	0.378	0.8	0.
3	1200	484	384	1730	0.378	0.8	0.048
4	1200	484	384	1730	0.36	0.8	-0.048
5	1200	484	384	1730	0.36	0.8	0
6	1200	484	384	2260	0.36	0.8	0.048
7	1300	242	192	2260	0.378	0.8	-0.048
8	1300	242	192	2260	0.378	0.8	0
9	1300	242	192	2260	0.378	0.8	0.048
10	1300	242	192	2260	0.36	0.8	-0.048
11	1300	242	192	2260	0.36	0.8	0
12	1300	242	192	2260	0.36	0.8	0.048

Table 4.3: Polarization splitter-rotator dimensions. All dimensions are in microns . The input and output waveguide lengths are approximate.

The data was normalized in a manner quite similar to the approach taken for the polarization splitters. The detected current (implicitly keeping track of polarization) in the TE Port for the polarization splitter-rotator $I_{PSR_{TE}}$ is written

$$I_{PSR_{TE}} = P_L C_{W_{in}} T_{in} T_{PSR_{TE}} T_{out} C_{W_{out}} R_d \tag{4.11}$$

where $T_{PSR_{TE}}$ is the transmission for the TE Port of the polarization splitter-rotator. Rearranging (4.11) we get

$$T_{PSR_{TE}} = \frac{I_{PSR_{TE}}}{P_L C_{W_{in}} T_{in} T_{out} C_{W_{out}} R_d} \tag{4.12}$$

Here again, by using the measured current I_{PClip} and transmission of a reference paperclip waveguide, we can express (4.12) as simply

$$T_{PSR_{TE}} = \frac{T_{PClip}}{T_{in} T_{out}} \frac{I_{PSR_{TE}}}{I_{PClip}} \tag{4.13}$$

Similarly, the expressions for the TM output port can be written as

$$T_{PSR_{TM}} = \frac{I_{PSR_{TM}}}{P_L C^{TE}_{W_{in}} T_{in} T_{out} C^{TM}_{W_{out}} R_d} \tag{4.14}$$

and by again using (4.3), (4.14) can be expressed as

$$T_{PSR_{TM}} = \frac{T_{PClip}}{T_{in}T_{out}} \frac{C_{W_{in}}^{TE}}{C_{T_{in}}^{TM}} \frac{I_{PSR_{TM}}}{I_{PClip}} \tag{4.15}$$

The polarization splitter-rotators measurements were normalized according to this procedure and the results are plotted in Fig. 4-22 and Fig. 4-23. The cross-talk in the TE Port (i.e. TM to TM in the TE Port) is limited by the polarization splitter while the cross-talk in the TM Port (i.e. TM to TM in the TM Port) is limited by the polarization rotator. Most of the polarization splitters achieved better than 20 dB extinction while most of the polarization rotators achieved better than 10 dB extinction across the $1.51 - 1.61\,\mu$m band. The longer devices (Fig. 4-22) tended to achieve slightly better performance than the shorter ones (Fig. 4-23) with the most impressive performance achieved in PSR1 and PSR2. In particular, PSR2 demonstrated better than 28 dB extinction in the TE Port indicating that its polarization splitter is performing very nicely. Otherwise it is of note that the splitters with the wider tall waveguide widths (i.e. PSR1, PSR2, PSR3, PSR7, PSR8, and PSR9) tended to perform slightly better than the devices with the narrower waveguide widths (i.e. PSR4, PSR5, PSR6, PSR10, PSR11, and PSR12).

To determine why the polarization splitters in the PSRs on Chip 1 performed so much better than the polarization splitters by themselves on Chip 1, calibrated SEMs were taken of the input and near the output ports of the devices. The measurements are presented in Fig. 4-24. Of note is the very close separation between the tall and wide waveguides. The smaller than designed initial separation improves the splitting between the TM guided modes thereby enabling the TM modes to de-phase before substantial coupling occurs. What is most impressive is that the devices worked remarkably well inspite of the significantly wider than expected horizontally oriented waveguide width.

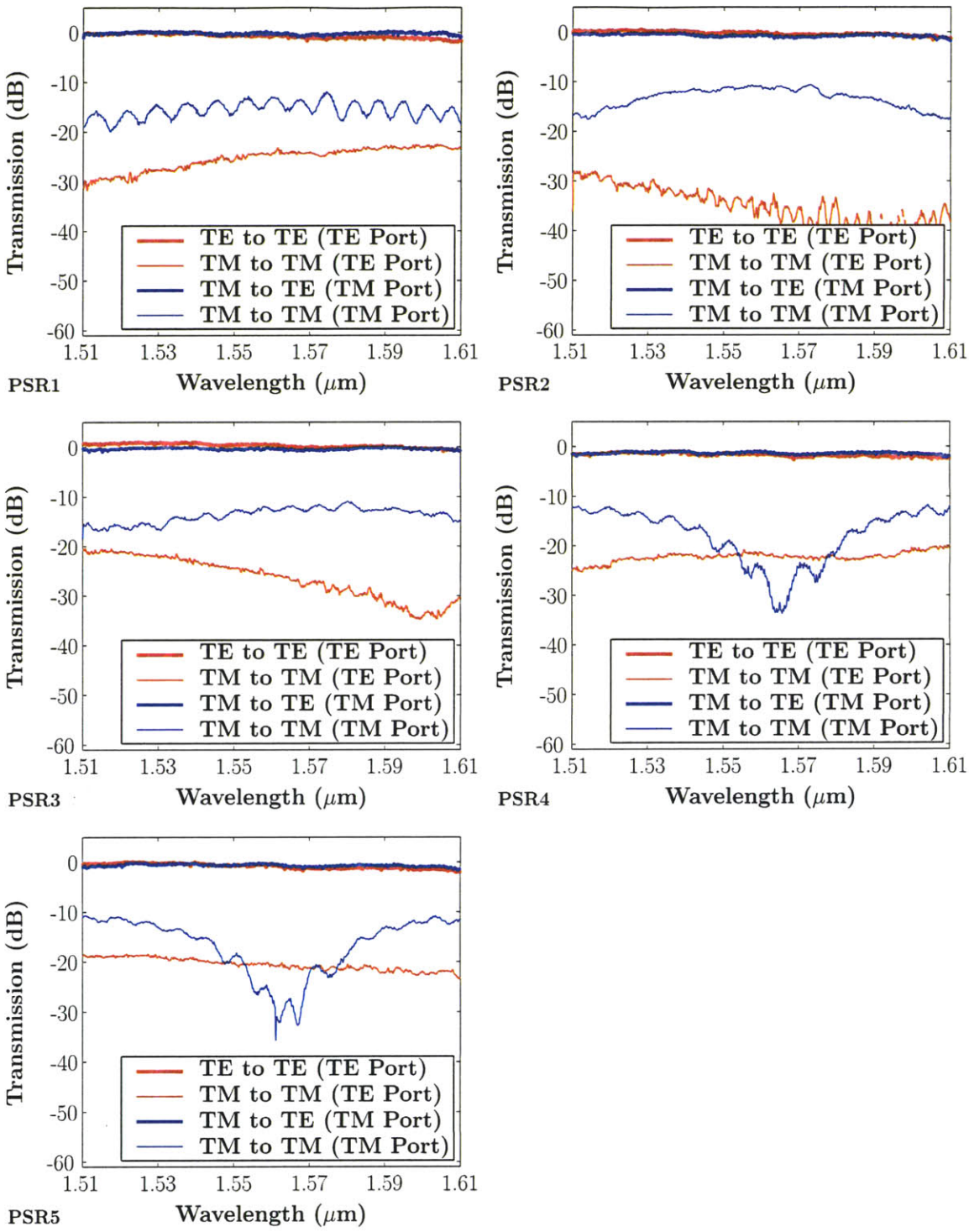

Figure 4-22: Measured performance of the two-layer polarization splitter-rotator depicted in Fig. 4-20. Measured data for PSRs PSR1-PSR5 are shown. Data was not collected for PSR6.

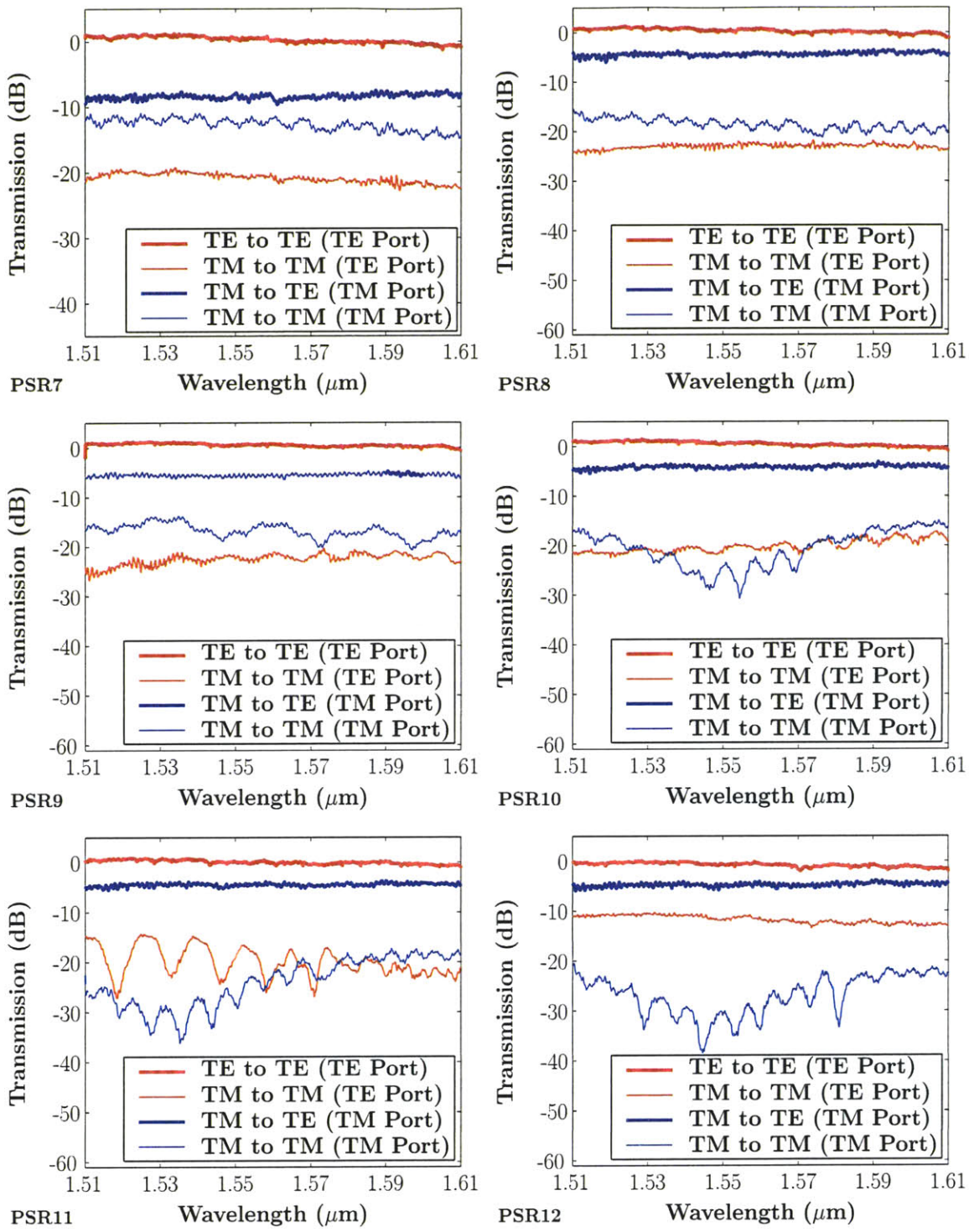

Figure 4-23: Measured performance of the two-layer polarization splitter depicted in Fig. 4-20. Measured data for PSRs PSR7-PSR12.

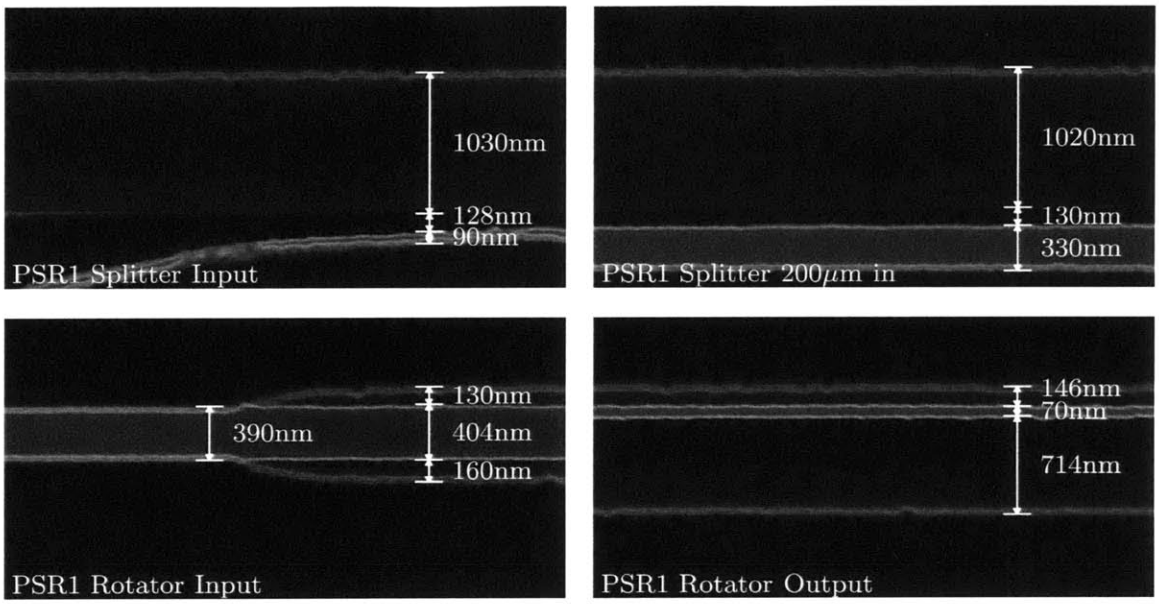

(a)

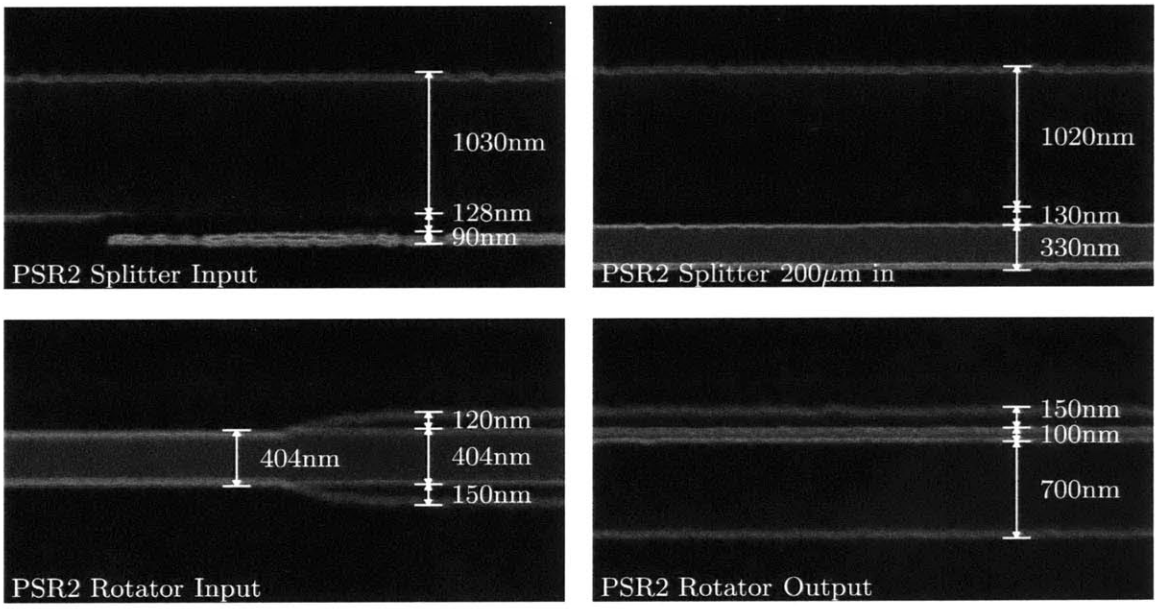

(b)

Figure 4-24: Calibrated SEMs of polarization splitter-rotators (a) PSR1 and (b) PSR2. The close initial separation s_1 in the splitter input is the cause of their high measured extinction ratios. Micrographs taken by Minghao Qi.

While quantitative measurements give the most accurate representation of device performance, qualitative measurements are often more exciting. To illustrate this point, we have included a series of images taken at the output facet of a representative polarization splitter for different combinations of input polarization state (Fig. 4-25). The images clearly demonstrate the ability of the device to re-direct the light based on the input polarization.

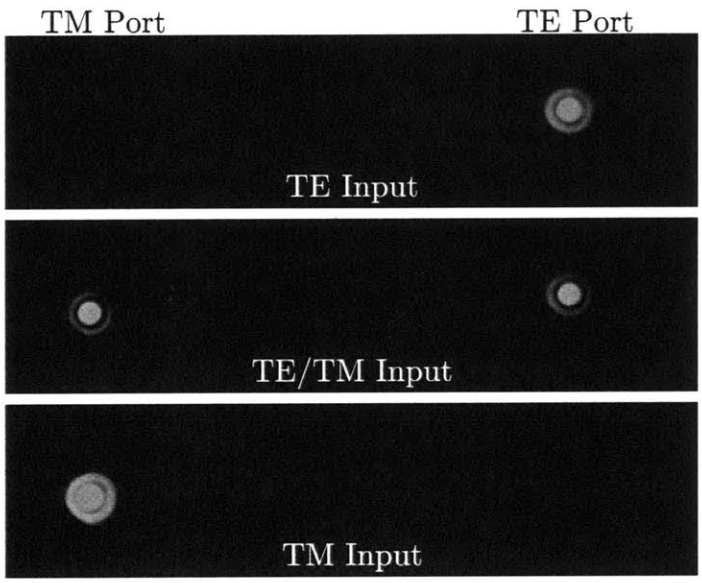

Figure 4-25: Infrared images of the output facet of PSR5 for different input polarization states.

4.7 Summary

Designs for polarization rotators, splitters, and splitter-rotators presented in Chapters 2 and 3 were taylored to the novel single deposition and two-step etch fabrication approach developed by Minghao Qi and Tymon Barwicz of MIT's Nanostructure Laboratory. Rigorous electromagnetic simulations were used to verify the device designs which were subsequently fabricated by Minghao Qi, and characterized. The highest performing polarization rotator achieved an extinction of $\sim 20\,\mathrm{dB}$ across the $1.51 - 1.61\,\mu\mathrm{m}$ band while the best performing polarization splitters achieved an extinction of $\sim 27\,\mathrm{dB}$ in both the TE and TM output ports. And, the integrated polarization splitter-rotators achieved extinctions that were very close to the best combined results of the individual splitters and rotators. More importantly, nearly all fabricated rotators, splitters, and splitter-rotators exhibited low cross-talk across

the $1.51 - 1.61\mu$m band. The consistent performance exhibited by the fabricated devices was in spite of dimensional variations and alignment offsets that exceeded 25 % of the device dimensions demonstrating the tolerant nature of the mode-evolution-based designs. Additionally, through proper normalization we showed that with the exception of devices that were not properly connected to their output waveguides, all of these devices exhibit nearly lossless performance. In the end, the fabrication errors that limited the ultimate potential of these device designs were in many respects beneficial as they demonstrated just how tolerant these mode-evolution-based devices are to geometrical variations.

Chapter 5

Microring-Resonator Filters

Having demonstrated broadband, low-loss, and low cross-talk polarization splitter-rotators, we can consider using polarization dependent components such as microring-resonators and still achieve chip-level polarization independence. In this chapter, I present the work of a significant team effort to produce the widest free spectral range (FSR), highest performing, high-order microring-resonator filters. My role in this effort was primarily to aide in the design and simulation of these structures. In general the design effort was shared with Milos Popovic, the fabrication performed by Tymon Barwicz, and the measurements made by Peter Rakich and Luciano Socci.

Our motivation, as discussed in the Introduction, is to develop an optical add/drop multiplexer (OADM) microphotonic circuit. We chose coupled microring-resonator based filters to form the basic filter for our optical add/drop multiplexer (OADM) because of the ease of fabrication and natural separation of ports inherent to the microring resonator approach. Impressive filter characteristics have been demonstrated by others using microring-resonators. In particular Little [1] and Absil [10] have demonstrated box-like drop port responses in filters with FSRs on the order of 6 nm. Yet, while the drop responses of these filters are impressive, deep rejection in the thru port response and considerably larger FSRs must be realized in order to implement an OADM of reasonable utility.

Herein, we set out to increase the FSR of microring-resonator filters by using very high index contrast (HIC) waveguides to enhance confinement and reduce bending loss in small radius rings. In addition, we address the problem of extinction in the thru port by compensating for spurious theoretical and fabrication related resonant frequency shifts. In

contrast to much of the work in the literature, we develop microring-resonator filter designs using rigorous electromagnetic simulations. This design approach is described, verified through experimental data, and applied to develop high performance coupled microring-resonator based filters. The resulting filters demonstrate the deepest thru port extinctions and largest FSRs of any previously reported high order microring-resonator filter. At the end of the chapter, we present recent results on the implementation of a Vernier approach [32, 33] that further extends the FSR. In contrast to most Vernier approaches for extending a small FSR [9] which tend to introduce significant dispersion into some of the thru channels leading to pulse distortion and signal degradation, the approach taken here has little impact on the dispersion introduced by the filter. Both simulation and fabrication results are presented. Here again, while much of this work has been published [34, 35, 36, 37, 38], this chapter represents a comprehensive overview of the research.

5.1 OADM Design Specifications

As was discussed briefly in the Introduction, the number of nodes that can communicate simultaneously in a wavelength routed ring network is twice the number of wavelengths on the ring. Consequently, for a R-OADM to be useful in a network it needs to make efficient use of the fiber bandwidth. And of course, cross-talk, loss and dispersion induced by the R-OADM must be kept low. These and other requirements for a simple R-OADM were provided to us by our sponsor, Pirelli Labs, and are listed in Table 5.1. Some of the more important filter specifications are indicated diagrammatically in Fig. 5-1. To summarize, the device must be able to selectively add and drop any channel over a $\sim$ 4.5 THz range. Channels are spaced every 100 GHz and thus as many as 45 channels can propagate simultaneously on the ring network. The filter is specified to have a $\sim$ 40 GHz 1 dB bandwidth and add / drop extinction levels of $\geq$ 28 dB 80 GHz from the channel center to avoid cross-talk with the adjacent channels. The thru extinction is similarly set to $\geq$ 28 dB. And, the pass-band ripple should be kept to $\leq$ 0.5 dB. While Table 5.1 lists attributes for a reconfigurable or R-OADM, in the current chapter only a passive OADM is considered.

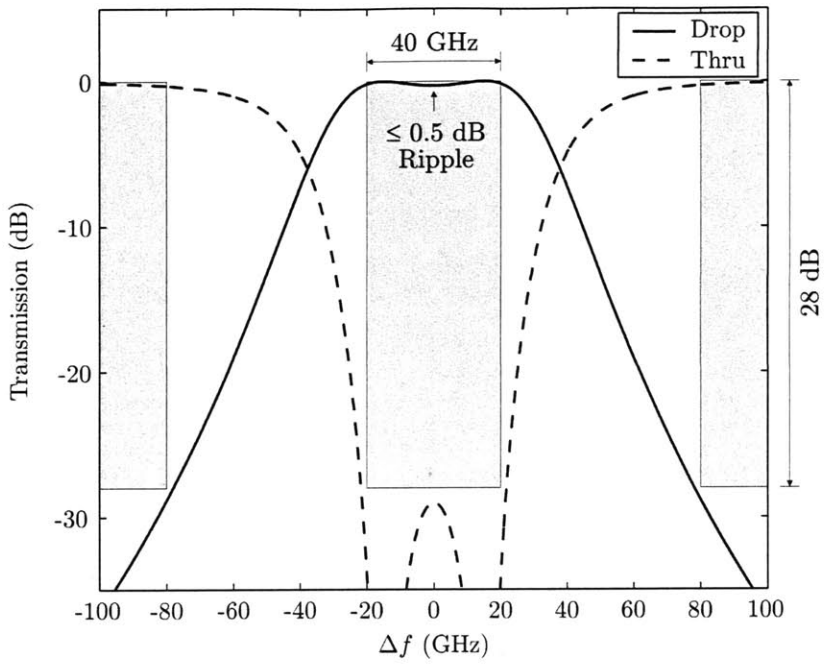

Figure 5-1: An example response meeting the OADM specifications.

Attribute	Specification
Operating Frequency Range (C-Band)	191.68 – 196.12 THz
Channel Spacing	100 GHz
Add/Drop Bandwidth (1 dB)	40 GHz
Add/Drop Extinction	$\geq$ 28 dB
Add/Drop/Thru Loss (Fiber-to-Fiber)	$\leq$ 4 dB
Add/Drop Ripple	$\leq$ 0.5 dB
Add/Drop/Thru Dispersion	$\leq$ 22 ps / nm
Thru Extinction	$\geq$ 28 dB
Adjacent Channel Loss	$\leq$ 1 dB
Polarization Dependent Loss	$\leq$ 0.2 dB

Table 5.1: The R-OADM specifications.

5.2 Microring-Resonator Design Approach

The specifications for the OADM described in Section 5.1 are very stringent. The filter bandwidth, extinction, loss, and shape must be dead-on in order to meet the design specifications. In order to appropriately design a filter of such high quality, rigorous electromagnetic simulations are required. Moreover, as a result of the high index contrasts, sharp bends, and tight modal confinement required to form microring-resonators, fast approximate techniques, such as the beam propagation method and eigenmode expansion, that rely on the paraxial wave equation or, alternatively, a limited set of eigenmodes, cannot accurately model microring-resonator-based filters. The finite-difference time-domain (FDTD) technique, however, does not make any approximations other than those caused by discretization, and is therefore ideal for modeling such a complex structure. Yet, full three-dimensional FDTD simulations require massive computational resources. Thus, designing the whole filter with FDTD is impractical. Fortunately, this is not necessary. Rather, filter responses can be synthesized by calculating the resonant mode with a finite-difference modesolver [11], calculating the complex coupling coefficients using full three-dimensional FDTD [21], and inserting these parameters into a coupled mode theory (CMT) or transfer matrix model.

Much emphasis has been placed on the design of microring-resonator filters using coupled mode theory (CMT) in the time domain [39, 40]. With this approach, the resonator field amplitudes are assumed to be spatially invariant within the resonator which enables the resonator to be described by its energy amplitude. A nice feature of CMT is that it provides a one-to-one correspondence with circuit theory enabling filter designs to be taken directly from microwave circuit tables. However, as a result of the uniform field approximation, this approach is only valid in the limit of large Q (i.e. $Q >> 1$), where the quality factor Q is defined as the number of cycles required for the energy amplitude to decay by $e^{-2\pi}$. Moreover, multiple resonances do not naturally fall out of the formalism.

The transfer matrix approach is more accurate, multiple resonances are innate to the formalism, and the parameters obtained from FDTD and eigenmode calculations can be directly inserted into the model. The calculation of the resonant mode provides the complex propagation constant $\beta = \beta_r + j\alpha$ needed to propagate the field in the ring whereas FDTD provides the complex transmission t and reflection coefficients r. The filter response is then

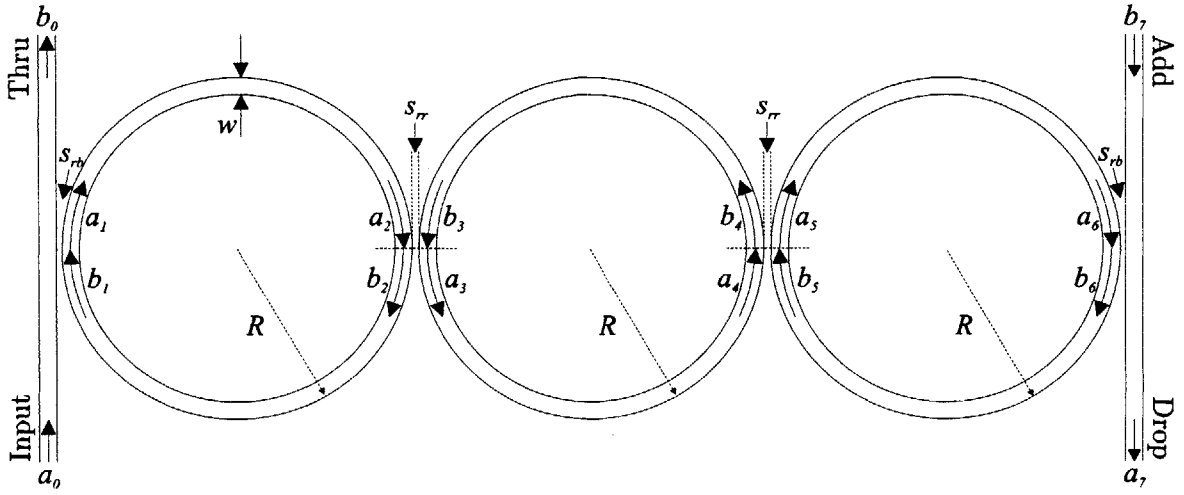

Figure 5-2: Diagram of a 3^{rd} order microring-resonator filter detailing the dimensions and mode amplitude coefficients used in the transfer matrix model.

assembled using the standard transfer matrix approach [39]. For example, consider the three ring filter depicted in Fig. 5-2. The transfer matrix connecting the input a_0 and thru b_o fields to the mode amplitude coefficients a_1 and b_1 of the first ring is

$$V_{01} = \frac{1}{t_1}\begin{pmatrix} (t_1^2 - r_1^2) & r_1 \\ -r_1 & 1 \end{pmatrix} \tag{5.1}$$

and the propagation matrix connecting the mode amplitude coefficients a_1 and b_1 to a_2 and b_2 is given by

$$V_{12} = \begin{pmatrix} e^{j\gamma\pi} & 0 \\ 0 & e^{-j\gamma\pi} \end{pmatrix} \tag{5.2}$$

where γ is the radial propagation constant (i.e. the number of optical cycles in the ring). Similar expressions can be obtained for connecting the input and output fields across each coupling point and propagating them through each ring section. The full transfer matrix is then obtained by simply multiplying the individual matrices together (5.3).

$$M = V_{67}V_{56}V_{45}V_{34}V_{23}V_{12}V_{01} \tag{5.3}$$

The add and drop port amplitudes b_7 and a_7 are related to the input a_0 and thru b_0 port

amplitudes through (5.4)

$$\begin{bmatrix} a_7 \\ b_7 \end{bmatrix} = \begin{bmatrix} M_{11} & M_{12} \\ M_{21} & M_{22} \end{bmatrix} \begin{bmatrix} a_0 \\ b_0 \end{bmatrix} \tag{5.4}$$

Since the input and add ports can, for the purposes of finding the filter response, be taken to be 1 and 0, respectively, the thru and drop port responses are given by $b_0 = -M_{21}/M_{22}$ and $a_7 = M_{11} - M_{12}M_{21}/M_{22}$.

It is important to note that the radial propagation constant must follow a dispersion relation that ensures a resonance condition when it takes on an integer value. The appropriate relation can be obtained from a Taylor series expansion of the radial propagation constant. For $\beta(\omega)$, we have

$$\beta(\omega) = \beta(\omega_0) + (\omega - \omega_0)\frac{\partial\beta}{\partial\omega}\bigg|_{\omega=\omega_0} + \cdots \tag{5.5}$$

and by noting that the radial propagation constant γ, is given by $\gamma = \beta L/2\pi$ where L is the resonator path length, we arrive at the following expression for γ

$$\gamma(\omega) = \gamma(\omega_0) + \frac{(\omega - \omega_0)}{\text{FSR}} \tag{5.6}$$

where we have dropped all high order terms and have used the fact that $L\frac{\partial\beta}{\partial\omega}\Big|_{\omega=\omega_0} = \frac{L}{v_g} = \frac{1}{\text{FSR}}$ where FSR is the free spectral range in units of Hertz. The FSR is generally found by calculating the resonant modes of a ring with mode numbers m and $m \pm 1$. However, it can be argued that for determining the filter response, γ is more accurately determined directly from the local group velocity because the filter response occurs over a bandwidth much smaller than the FSR.

The transfer matrix approach just described is a highly accurate technique that is used throughout this chapter to calculate filter responses. However, the concept of Q which is borrowed from coupled mode theory in the time domain is commonly referred to in this chapter. To connect the transfer matrix approach, which operates in the spatial domain, with coupled mode theory in the time domain, we can use a Taylor series expansion to expand the propagation constant in terms of the resonant frequency. Doing so

$$\beta(\omega) = \beta(\omega_0) + (\omega - \omega_0)\frac{\partial\beta}{\partial\omega}\bigg|_{\omega=\omega_0} + \cdots \tag{5.7}$$

and substituting $\omega_0 + \frac{j}{\tau}$ for ω, where τ is the temporal decay constant of the resonator, we get

$$\beta(\omega_0 + \frac{j}{\tau}) = \beta(\omega_0) + \frac{j}{\tau}\frac{\partial\beta}{\partial\omega}\bigg|_{\omega=\omega_0} + \cdots \tag{5.8}$$

The imaginary part of the complex propagation constant is commonly denoted by α. Noting that $Q = \frac{\omega_0\tau}{2}$ and $\frac{\partial\beta}{\partial\omega}\Big|_{\omega=\omega_0} = \frac{1}{v_g}$ where v_g is the group velocity, we find

$$Q = \frac{\omega_0}{2\alpha v_g} \tag{5.9}$$

where we have dropped all high order terms. Here, we see that the Q is inversely proportional to the spatial decay coefficient α. The higher the loss, the lower the Q.

Before moving on to the first actual filter design, it is worth considering one last point. The flat pass-band and sharp roll-off required by the filter specifications requires a high order filter design. Others have shown that high order maximally flat and Chebyshev filter responses can be obtained by coupling multiple resonators in series and using microwave filter tables to determine the required couplings [40]. A diagram of series coupled resonators is provided in Fig. 5-3a and maximally flat responses for 1^{st}, 2^{nd}, and 3^{rd} order filters are provided in Fig. 5-3b. By appropriately adjusting the couplings, the filter specifications in Fig. 5-1 can be met with a 3^{rd} order filter.

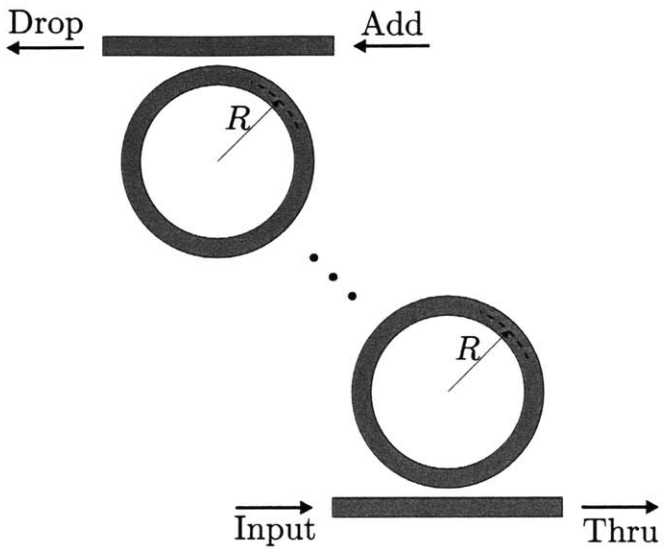

(a)

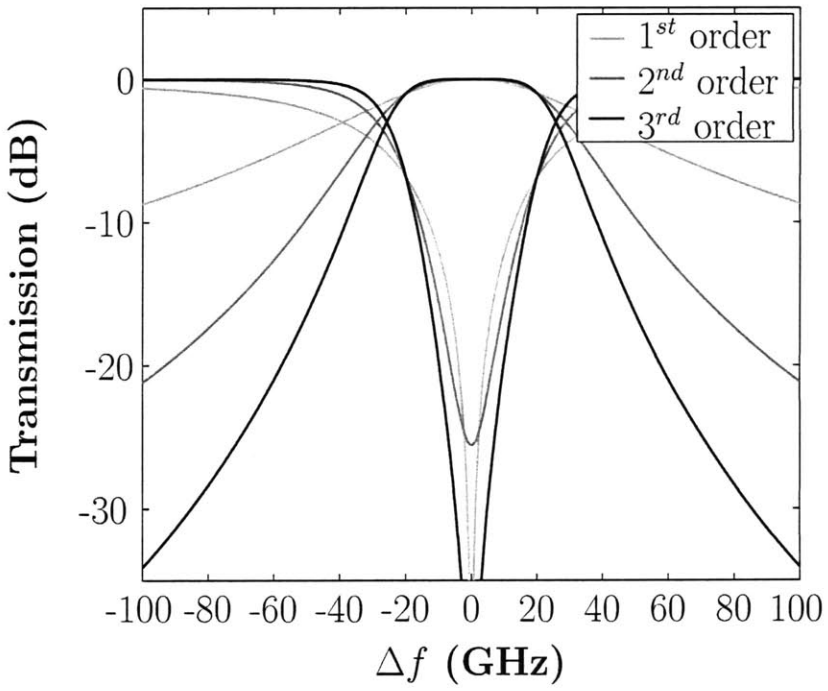

(b)

Figure 5-3: (a) Diagram of series coupled microring resonators and (b) corresponding maximally flat filter responses for 1^{st}, 2^{nd}, and 3^{rd} order filters.

5.3 Microring-Resonator Filter Design/Fabrication I

Three sets of microring-resonator filters were fabricated. The first of which was not designed with the rigorous approach described in the previous section because at the time computational resources were scarce. Instead guestimates of the ring-bus and ring-ring coupling gaps were made. As a result, the performance of this early filter did not closely match the design. However, lessons were learned in this design/fabrication iteration and rigorous post-fabrication simulations served to validate the rigorous design approach presented in Section 5.2, clearly demonstrating our ability to accurately model microring-resonator filters and reconcile theory with experiment. As a result, this fabrication iteration turned out to be highly beneficial despite the crude nature of the design. Here again, much of this work has previously been published [34, 35].

5.3.1 Design I

Both silicon (Si) and silicon nitride (SiN) were considered as core materials for forming our microring waveguides. Silicon, which has an index of 3.48 at $\lambda = 1.55\,\mu$m is a convenient material choice because in its crystalline form, its index is well known and does not vary from wafer to wafer. Moreover, its high index enables highly confined modes that can survive tight bends with little radiative loss. Consequently, silicon waveguides can be used to form high Q microring-resonators with very large FSRs. However, the index contrast and device tolerances scale together leaving very high index contrast structures with very tight tolerances. Stochiometric silicon nitride (SiN) has an index of 2.0 at $\lambda = 1.55\,\mu$m and can provide a moderately high index contrast. Yet, while Fig. 1-5 indicates that an index of 1.9 is sufficient to provide a FSR of 4.5 THz, the vertical confinement provided by two-dimensional waveguide cross-sections reduces the effective index contrast. Thus, to achieve the required 4.5 THz FSR, higher index contrasts are required.

As an intermediate solution, we chose to form our waveguides from silicon rich silicon nitride yielding an index of $n \sim 2.2$. Silica ($n \sim 1.445$) was chosen to form the under-cladding, and to avoid a final deposition step, air was used for an upper-cladding. A cross-section of the ring-bus coupler region depicts the geometry (Fig. 5-4). A wide, thin waveguide cross-section was chosen for a few reasons: (1) wide waveguides shift the sensitivity of the resonant frequency from the waveguide width to the waveguide height which is controlled

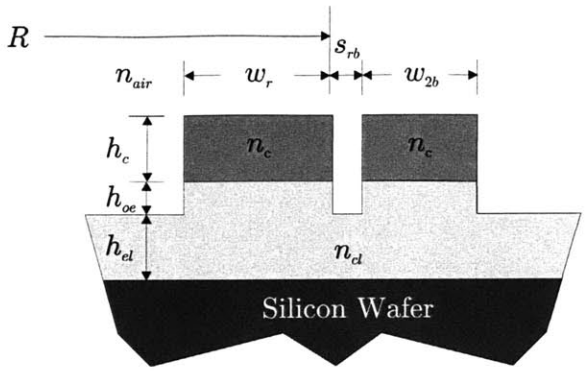

Figure 5-4: The cross-section of the ring-bus coupler region of a general microring resonator waveguide.

by the more accurate film deposition process, (2) the problem of surface roughness induced scattering loss is shifted from the relatively rough sidewalls to the much smoother top and bottom waveguide surfaces, and (3) large aspect ratio guides naturally inhibit coupling between orthogonally polarized modes. The over-etch was introduced so as to ascertain the etch fully penetrated the waveguide core. Also shown in the diagram is a narrower bus than ring waveguide. The narrowed bus serves to improve the ring-bus coupling. A ring waveguide width of $w_r = 1050\,\text{nm}$ was chosen with a core height of $h_c = 330\,\text{nm}$, radius of $R = 7.28\,\mu\text{m}$, overetch depth of $h_{oe} = 100\,\text{nm}$, and under-cladding thickness of $h_{cl} = 2.5\,\mu\text{m}$. The core and cladding indices are those of silicon rich silicon-nitride $n_c = 2.2$ and silica $n_{cl} = 1.445$. With these dimensions and indices, the 46^{th} and 47^{th} resonances have wavelengths near 1550 nm. Their respective resonant wavelengths and Qs were calculated using a modesolver developed by Milos Popovic [11] to be $\lambda_{46} = 1561.1\,\text{nm}$ with $Q \sim 28,000$ and $\lambda_{47} = 1537.0\,\text{nm}$ with $Q \sim 42,000$. The 47^{th} resonance was chosen as the design resonance and a 3^{rd} order filter (i.e. 3 coupled micro-rings) was constructed with these rings. Bus waveguides of width $w_b = 850\,\text{nm}$ were designed to couple to the rings. The ring-bus and ring-ring separations chosen for this initial filter are $s_{rb} = 60\,\text{nm}$ and $s_{rr} = 285\,\text{nm}$.

5.3.2 Fabrication Process I

The fabrication and process development were performed by Tymon Barwicz of MIT's Nanostructures Laboratory. Since the focus of this thesis is on the design of microphotonic

devices, only a brief discussion (provided by Tymon Barwicz) of the fabrication process is included. A detailed discussion of the fabrication will be contained in Tymon's thesis to published soon after this one.

The waveguide under-cladding was formed by thermally oxidizing silicon wafers to create a 2.5 μm layer of SiO_2, a layer sufficiently thick to prevent substantial coupling to the substrate. Then, a layer of SiN was deposited by low-pressure chemical-vapor-deposition (LPCVD) using a gas mixture of SiH_2Cl_2 and NH_3. The structures were patterned using direct-write scanning-electron-beam lithography (SEBL) with non-chemically-amplified resist. This approach enables the fabrication of high resolution features with strict dimensional control. To do so, 200 nm of polymethyl-methacrylate (PMMA) and 40 nm of Aquasave were spun on. PMMA is a positive e-beam resist while Aquasave is a water-soluble conductive polymer from Mitsubishi Rayon used to prevent charging during SEBL. The PMMA was exposed at 30 KeV using a Raith 150 SEBL system. The e-beam dose was selected to generate a correct bus waveguide width at the coupling region. Post exposure, the Aquasave was removed, and the PMMA developed. Next, 50 nm of Ni was evaporated on the structure, and a liftoff was performed by removing the nonexposed PMMA. Using the Ni as a hardmask, the waveguides where defined by conventional reactive-ion-etching (RIE) with a gas mixture of CHF3-O2 in a 16:3 ratio. To obtain an accurate etch depth, the RIE was performed in several steps between which the etch depth was measured with a profilometer. Finally, the Ni was removed using a commercial wet Ni etchant.

5.3.3 Device Characterization I

Scanning-electron-micrographs (SEMs) of the waveguide cross-section and microring-resonator filter are presented in Fig. 5-5. The lateral device dimensions were measured using the e-beam system in measure mode while the refractive indices and layer thicknesses were measured using an ellipsometer. The etch depth was measured using a profilometer. The measured parameters are listed in Tab. 5.2.

The fabricated structure was characterized with a tunable laser and the measurement setup depicted in Fig. 4-6. The measured response demonstrates a 24 nm FSR (Fig. 5-6a). However, a closeup of the resonance at 1544.5 nm (Fig. 5-6b) reveals that the design reponse is asymmetric and exhibits a wider ($\sim$ 80 GHz) than expected (40 GHz) bandwidth. While more obvious in the thru port, both the thru and drop port responses are asymmetric, a

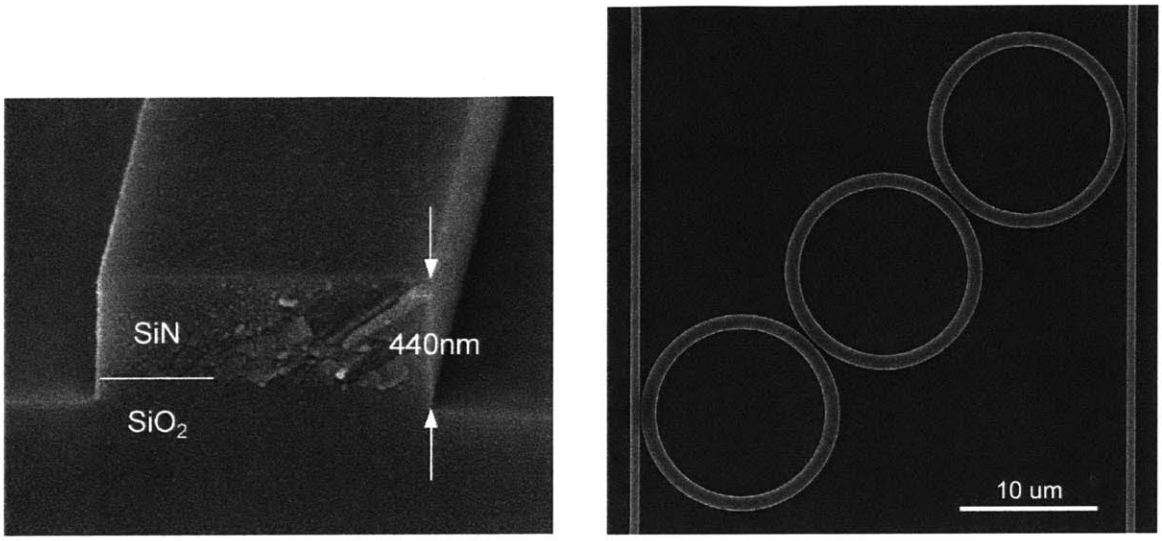

(a) (b)

Figure 5-5: Scanning electron micrographs (SEMs) (a) of the waveguide cross-section and (b) a top view of a fabricated microring-resonator filter. Micrograph taken by Tymon Barwicz.

result of the central ring having a higher frequency than the outer rings by $\sim 22\,\mathrm{GHz}$. In addition to the wider than expected bandwidth and spectral asymmetry, appreciable losses (2.5 dB) are evident in the drop response.

Fortunately, by the time the full characterization of the device had been completed, computational resources became available enabling rigorous post-fabrication simulations to be performed to determine the cause of the design and/or fabrication related errors. The resonant mode of the ring was calculated using the finite-difference modesolver. The shorter than expected waveguide core height $h_c = 314\,\mathrm{nm}$ reduced the theoretical Q of the resonator to $Q = 22,000$. The coupling coefficients were calculated using three-dimensional FDTD simulations by launching a pulse with the cross-sectional distribution of the waveguide mode into the ring and taking mode overlaps with the corresponding ring and bus modes at the input and output waveguides. False color images of the out of plane magnetic field (i.e. H_z) for the ring-bus and ring-ring simulations are presented in Fig. 5-7. The overlaps provided complex coupling coefficients for the measured ring-bus and ring-ring separations. In addition to the coupling coefficients and loss obtained from the simulations, the presence of differing external dielectrics, causes differential phase shifts and thus frequency shifts in

Parameter	Designed	Measured
n_c	2.2	2.217
n_{cl}	1.445	1.455
h_{cl}	2500	2530
h_c	330	314
h_{oe}	100	126
w_r	1050	1060
w_b	850	860
s_{rb}	60	60
s_{rr}	285	268
R	7265	NM

Table 5.2: The dimensions/indices of the fabricated Design I microring resonator filters. Dimensions measured by Tymon Barwicz using the Raith 150 e-beam in measure mode.

the rings, an effect that has been termed coupling induced frequency shifts (CIFS) [41]. The CIFS is calculated by using a Taylor series to approximate the frequency shift of a resonator as a result of the phase shift $\Delta\phi$. Doing so, we have

$$\nu(\phi) = \nu(\phi_0) + (\phi - \phi_0)\frac{\partial \nu}{\partial \phi}\bigg|_{\phi=\phi_0} + \cdots \tag{5.10}$$

and by noting that 2π radians are subtended in one FSR, we arrive at

$$\Delta\nu = \frac{\Delta\phi}{2\pi}\,\mathrm{FSR} \tag{5.11}$$

where $\Delta\nu$ is the frequency difference in Hertz.

Since FDTD can only be used to obtain couplings at discrete separations it is necessary to interpolate between calculated points to obtain accurate results. Fortunately, the coupling, loss, and CIFS all exhibit logarithmic dependencies with separation as a result of the exponential decay of the evanescent field. Plots of the calculated ring-bus and ring-ring couplings, losses, and CIFS (using the measured dimensions) as a function of separation are provided in Fig. 5-8. The exponential fit parameters are included with the plots using the subscripts c, l, and f to refer to coupling, loss, and frequency shift, respectively. Using the fits and the measured ring-bus and ring-ring separations ($s_{rb} = 60\,\mathrm{nm}$, and $s_{rr} = 268\,\mathrm{nm}$), we find ring-bus and ring-ring power transmission coefficients of $T_{rb} = 0.109$ and $T_{rr} = 0.007$ and corresponding coupler scattering induced losses of $L_{rb} = 0.024$ and $L_{rr} = 0.0039$ for

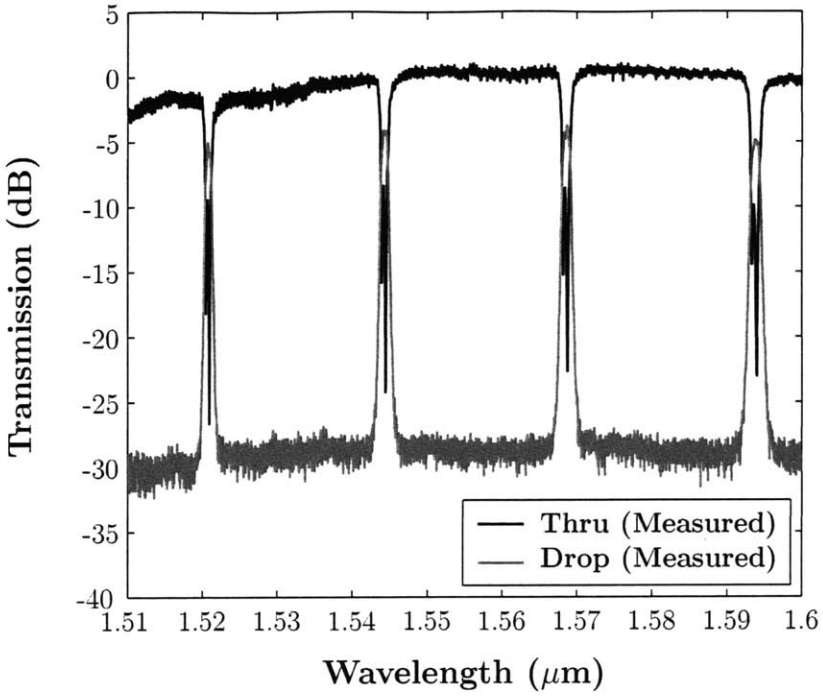

(a)

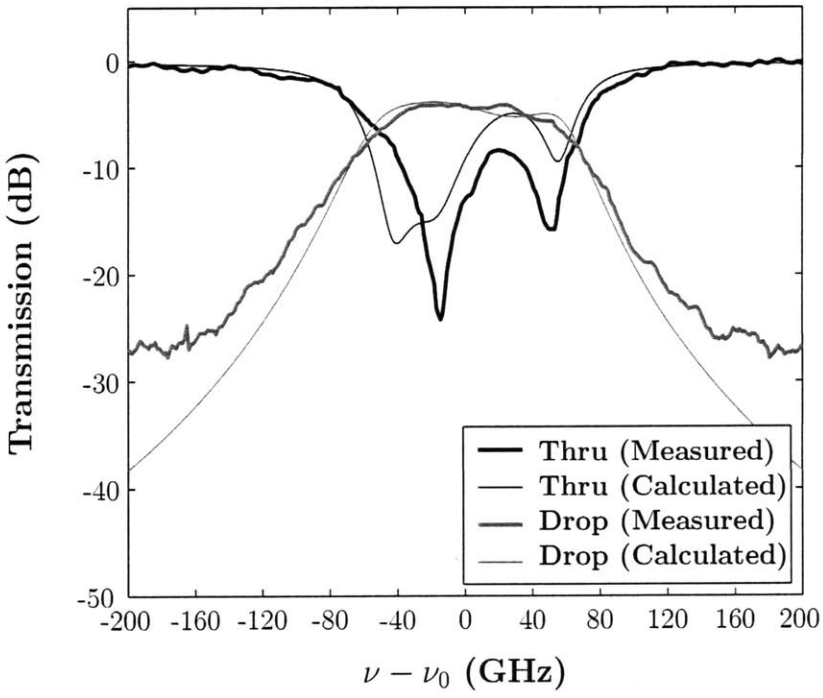

(b)

Figure 5-6: (a) Measured wide-band filter response revealing a 24 nm FSR and (b) measured filter response with calculated filter response superimposed. The calculated response was obtained using device dimensions and indices measured post-fabrication with the transfer matrix approach described in Section 5.2. The resonant frequency was fit to the measured response.

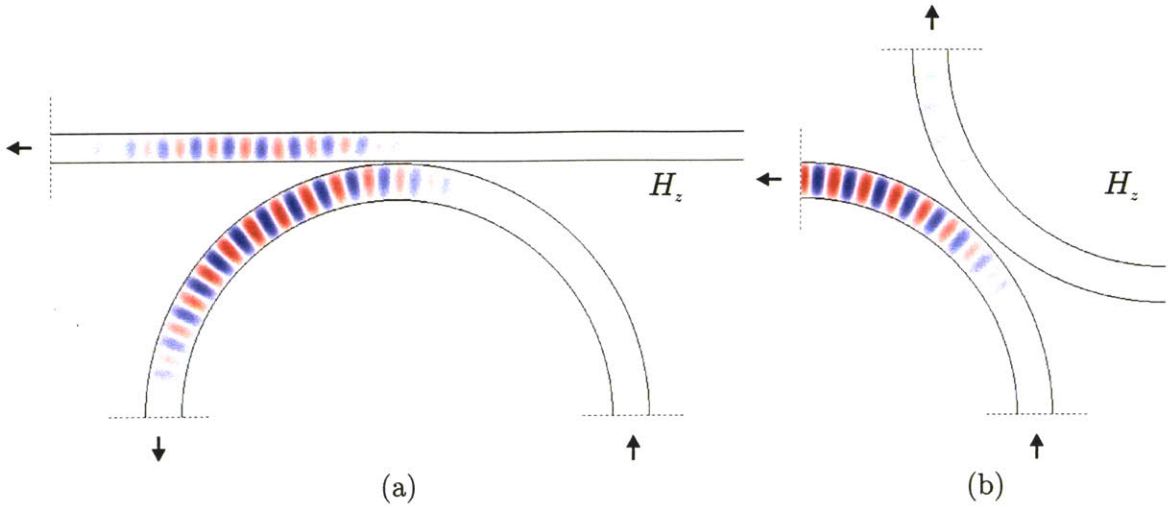

Figure 5-7: False color images of the out of plane (i.e. H_z) magnetic field for the (a) ring-bus and (b) ring-ring coupling region simulations. The figures depicts the input fields and overlap planes (dotted lines). The bouncing back-and-forth of the coupled fields is an indication of coupling to higher order leaky modes resulting in loss.

which the bend losses were subtracted from the result. Similarly, frequency shifts (CIFS) were calculated to be $\Delta\nu_{rb} = 42.6\,\text{GHz}$ and $\Delta\nu_{rr} = 7.8\,\text{GHz}$ resulting in a total CIFS between the center and outer rings of 34.8 GHz.

Using the calculated coupling coefficients, loss coefficients, calculated complex propagation constant, and by fitting values for the resonant frequency, propagation loss, and relative frequency shifts between the center and outer rings, a theoretical curve based on post fabrication simulations was generated. The calculated and measured filter responses are overlayed in Fig. 5-6b. The only fit parameters were the resonant ring resonant frequencies which included a 22 GHz frequency difference between the center and outer rings and a waveguide propagation loss of 9.6 dB/cm. All other parameters were calculated. The frequency shift between the center and outer rings was fit because the theoretical CIFS component is only one portion of the realized shift. E-beam proximity effects and other fabrication induced distortions of the rings should account for a significant portion of the shift. The fitted loss, while high is in agreement with losses found in the paperclip waveguides of the previous chapter. Otherwise, the calculations revealed that the errors in the design lead to the larger ($\sim 80\,\text{GHz}$) than expected (40 GHz) bandwidth as the calculated and measured responses exhibit nearly identical bandwidths. The strong agreement be-

tween theory and experiment verified the simulation technique, a technique that would be applied to each of the subsequent filter designs.

As a final note, the large coupling losses in the ring-bus and ring-ring coupling regions resulted in a significant portion of the filter loss. The losses are due to coupling to a lossy higher-order transverse mode of the ring waveguide at the couplers. The waveguides support a single mode of each polarization when straight, but when bent reconfine the second-order TE mode as a leaky resonance with high bend loss. The calculated response reveals that out of the 3.8 dB losses observed in the filter, 2 dB (i.e. 53%) are the result of coupler scattering.

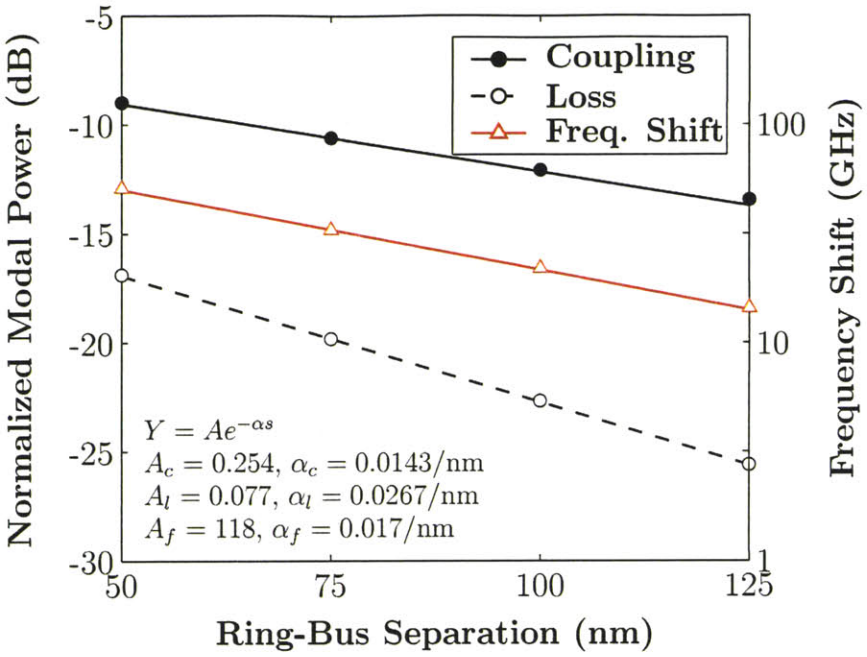

(a)

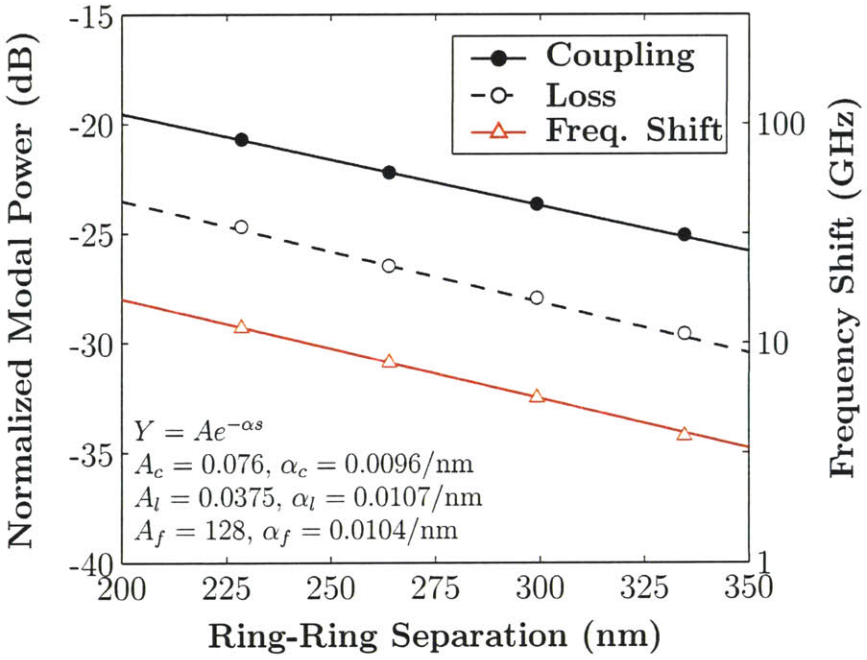

(b)

Figure 5-8: 3D FDTD determined (a) ring-bus and (b) ring-ring, coupling, loss, and coupling-induced frequency shifts for Design I.

5.4 Microring-Resonator Filter Design / Fabrication II

Having completed one design/fabrication cycle which demonstrated both our ability to accurately fabricate and model coupled microring resonator filters, we set out to improve upon our initial results. The first step was to design a filter using the rigorous transfer matrix approach described in Section 5.2. In doing so, we wanted to reduce the coupler scattering induced losses and compensate for the CIFS to produce a filter with the correct bandwidth and filter shape. These results were recently presented [36].

5.4.1 Design II

The post-fabrication simulations of the previous device indicated that a significant component of the losses in the filter were due to scattering at the coupler regions. Additionally, if the correct filter bandwidth had been achieved another significant component of the loss would have been due to the relatively low radiation Q. Thus, in designing a new filter we set out to improve the Q of the resonator while reducing the losses at the coupler regions. However, extinguishing the secondary TE_{21} mode believed to be responsible for the excess loss, requires reducing the guide width which has the adverse effect of reducing the Q of the desired TE_{11} mode. To bring the Q of the TE_{11} mode back up the height and radius of the ring must be increased.

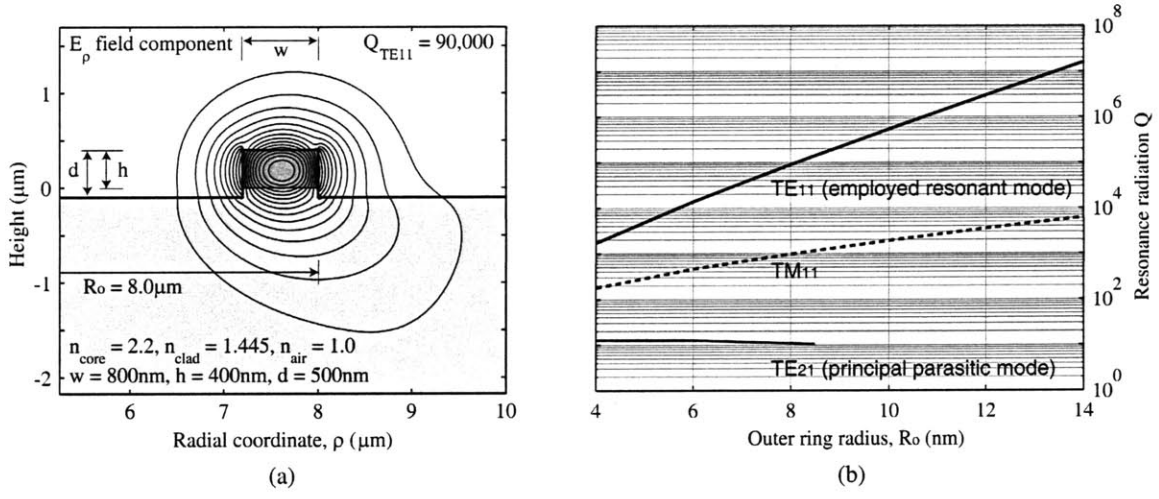

Figure 5-9: (a) HIC ring waveguide cross-section with overlaid horizontal electric field pattern; (b) Q vs. radius and FSR for the fundamental TE_{11} and spurious TE_{21} and TM_{11} modes. Simulation by Milos Popovic.

Doing so, a radiation $Q \sim 90,000$ was achieved for the TE_{11} mode with an outer ring radius of $R = 8\,\mu$m, guide width $w_r = 800\,$nm, guide height $h_c = 400\,$nm, and over-etch depth of $h_{oe} = 100\,$nm while reducing the Q of the TE_{21} to 10. The increased core layer thickness increases the confinement and Q of the TM_{11} mode, but its presence is of little concern since coupling to it is inhibited by the near-orthogonality of the cross-polarized modes in the coupling regions. The resonant wavelength remained nearly constant at $\lambda_{52} = 1544.5\,$nm, but as indicated, the mode number increased to $m = 52$ reducing the FSR to 20 nm.

To determine the complex coupling coefficients, coupling-induced frequency shifts CIFS, and loss, FDTD simulations were performed on the coupling regions. Here, the bus waveguides were again simple straight guides, but this time the bus width was set equal to the ring width (i.e. $w_b = w_r = 800\,$nm). Plots of the power coupling ratio, and loss as a function of ring-bus and ring-ring separations are presented in Fig. 5-10a and Fig. 5-10b. The data sets were plotted on logarithmic scales and fitted with exponentials (linear on the logarithmic scale). Here again, all of the curves demonstrate clear exponential dependencies.

As was described at the beginning of this chapter, for the OADM application a filter with a flat-top, 40 GHz 1 dB passband, 28 dB thru port extinction, and 28 dB rejection 80 GHz from the center of the passband is desired. Coupled power ratios of $T_{rb} = 0.089$ for the ring-bus and $T_{rr} = 0.0017$ and for the ring-ring couplers were chosen which resulted in coupler scattering induced losses of $L_{rb} = 0.007$ and $L_{rr} = 0.000055$. At less than 8 % and 3.3 % of the coupled power ratios, respectively, the scattering losses are much lower than in Design I confirming the importance of minimizing the confinement of the TE_{21} mode. Using the transfer matrix approach described in Section 5.2, the uncompensated response was generated and is presented in Fig. 5-11a. The passband is highly distorted due to a net CIFS of 38.3 GHz, a shift comparable to the filter bandwidth. If the CIFS is correctly compensated, the theoretical response depicted in Fig. 5-11b is obtained. The drop port response exhibits a flat passband, 38 GHz 1 dB bandwidth, and 1.2 dB loss due to bending and coupler scattering while the thru port demonstrates 19 dB extinction.

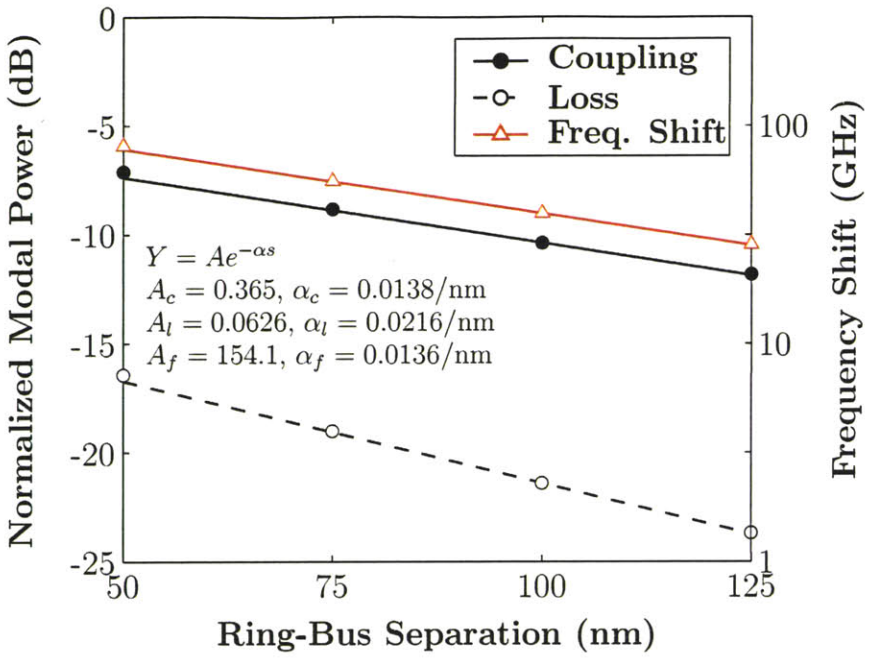

(a)

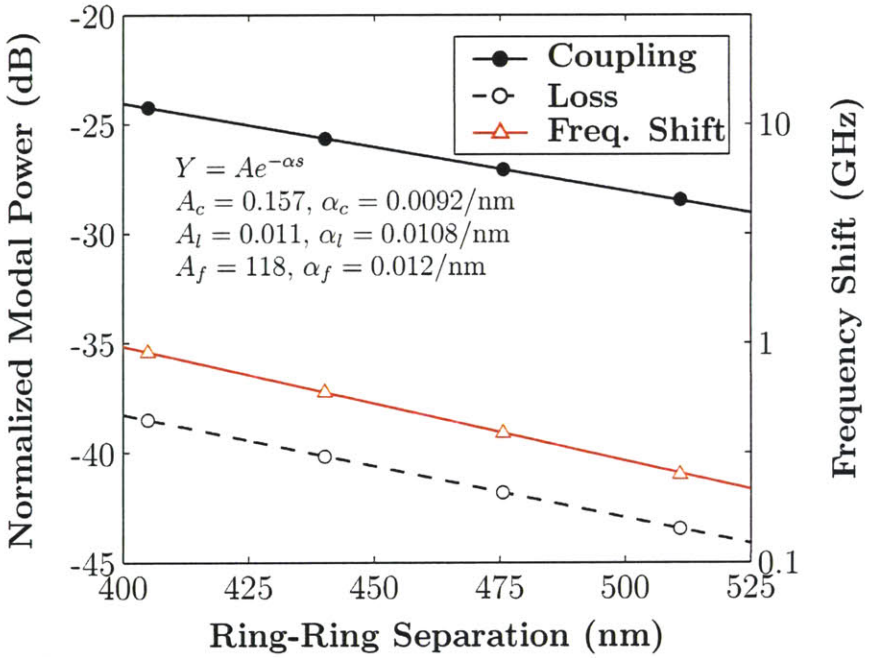

(b)

Figure 5-10: 3D FDTD determined (a) ring-bus and (b) ring-ring, coupling, loss, and coupling-induced frequency shifts for Design II.

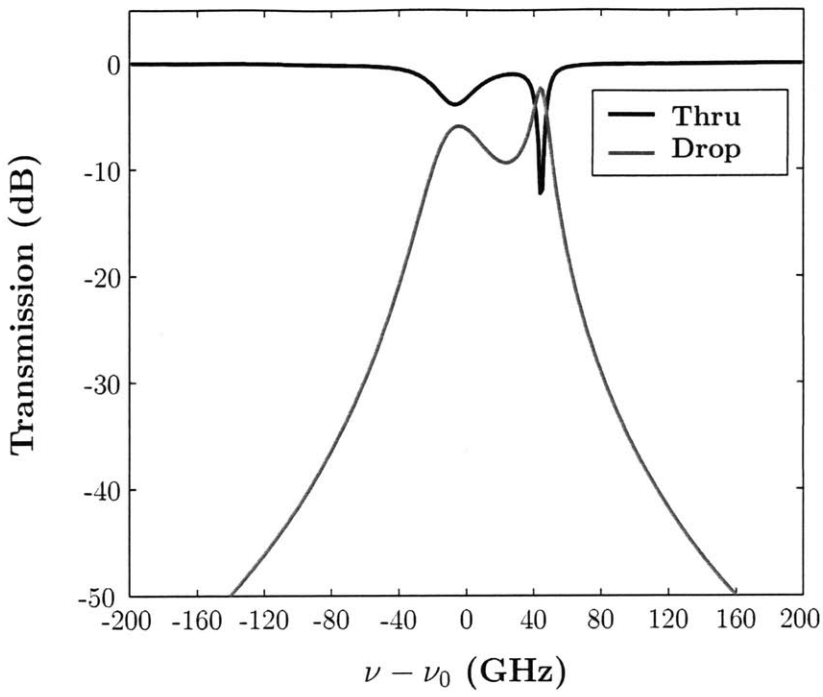

(a)

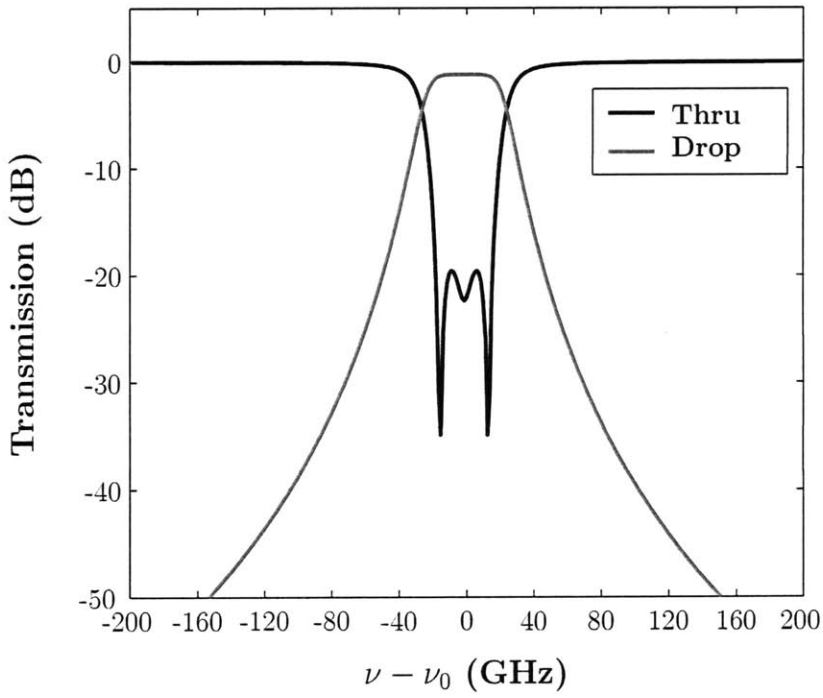

(b)

Figure 5-11: Theoretical filter responses for the CIFS (a) uncompensated and (b) compensated filters.

Achieving the full 28 dB extinction in the thru port is done in principle using cascaded filters [37]. The direct write e-beam system used to fabricate the rings has a 6 nm pixel size. To ensure that each ring is identically exposed, the structure must fall on integer multiples of the e-beam grid. So, rounding the separations to the nearest 6 nm grid point, we arrive at ring-bus and ring-ring separations of $s_{rb} = 102\,\text{nm}$ and $s_{rr} = 492\,\text{nm}$, respectively, corresponding to the aforementioned couplings.

5.4.2 Fabrication and Characterization of Design II

The fabrication was done using a process substantially similar to that described in Section 5.3.2 with the main differences being a 500 nm deep etch depth and use of differential e-beam doses to compensate for the frequency shift of the center ring. Not knowing the appropriate dose to apply, a dose matrix was applied across many filters with each filter getting a slightly different dose to the center ring.

The measured thru and drop responses for the uncompensated filter are shown in Figs. 5-12a. A fit to the response using the calculated coupling coefficients indicates that the frequency of the center ring is 170 GHz higher than that of the rings adjacent to the bus waveguides. The additional shift of the rings adjacent to the bus waveguides beyond the 38.3 GHz caused by the CIFS is due to e-beam proximity effects. This is an intuitive result as proximity effects are more severe for the rings adjacent to the bus due to the smaller ring-bus separation. The result is over-exposure and thus widening of the ring waveguides. The added dielectric increases the effective index requiring a lower frequency to keep a constant phase and remain resonant ($\phi = \omega n_{eff}/c$). In addition to providing the differential frequency shift, the fit to the uncompensated response enables an accurate determination of the loss in the ring as the filter behaves much like a single lossey ring in the thru port. The propagation loss determined from the fit is 15 dB/cm.

A 4.5 % increase in the e-beam dose to the center ring was sufficient to compensate for the 170 GHz frequency shift. The thru and drop port responses of the resulting compensated filter (shown in 5-12b) exhibit a 30 GHz wide 1 dB passband in the drop port, with a roll-off that provides 25 dB extinction 58 GHz from the channel center. In addition, a $\sim$ 14 dB in-band rejection of the dropped channel in the thru-port was achieved, the highest reported for a high-order microring filter. However, the filter exhibits 6 dB of drop loss which also serves to round the compensated filter passband. A fit, using the calculated coupling coeffi-

Parameter	Designed	Measured
n_c	2.2	2.189
n_{cl}	1.445	1.455
h_{cl}	2500	2530
h_c	400	406
h_{oe}	100	104
w_r	800	802
w_b	800	804
s_{rb}	102	103
s_{rr}	492	485
R	8000	NM

Table 5.3: The dimensions/indices of the fabricated Design II microring resonator filters. Dimensions measured by Tymon Barwicz using the Raith 150 e-beam in measure mode.

cients and the 15 dB/cm propagation loss determined from the uncompensated response is superimposed on the measured response. The loss obtained in the fit is considerably lower than that of the measured response. This discprency is due to the narrower than expected bandwidth of the filter which makes the filter more sensitive to loss components. The loss breakdown is 9 % due to bending, 11 % due to excess coupler scattering and 80 % attributed to excess propagation loss and the narrower than expected bandwidth.

The device lateral dimensions were measured with the e-beam lithography system in measure modes. Indices were measured using an ellipsometer and thicknesses using a profilometer. The results are listed in Tab. 5.3. Most of the critical dimensions were accurately attained. The only major exception is the waveguide core index which is approximately 5 % lower. The lower core index is the likely cause of the reduced coupling and narrower filter bandwidth. Despite this minor error and the higher than expected losses, this design/fabrication represented a major step towards meeting the OADM design specifications as both the filter shape and bandwidth were much closer to the design than in Design I.

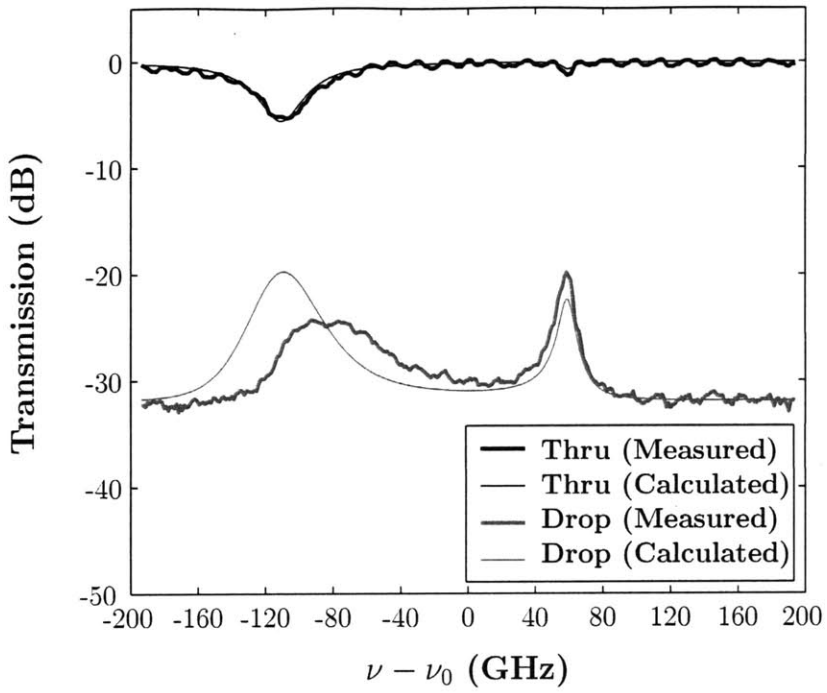

(a)

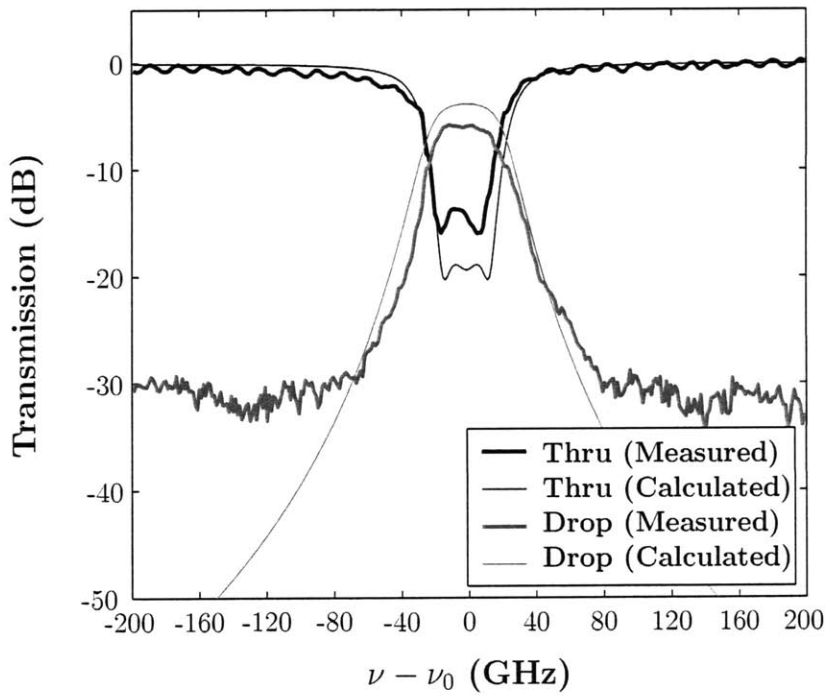

(b)

Figure 5-12: (a) Drop and thru port response of the uncompensated 3^{rd} order filter and (b) drop and thru port responses of the compensated filter with a 15 dB/cm waveguide loss obtained from the fit to the uncompensated response. The uncompensated filter exhibits a 170 GHz frequency shift between the center and outer rings.

5.5 Coupled Microring-Resonator Design III

Although the second design/fabrication iteration demonstrated a frequency compensated filter with high thru port extinction, the response is still far from the design specification. While to a large extent the filter loss was caused by excess propagation loss in the waveguides, a theoretical loss of 1.2 dB plagued the design (Fig. 5-11). And, it seems the interplay between design and fabrication could still be better as the filter bandwidth missed its mark by more than 25 %. Another design/fabrication iteration was initiated to improve upon these results.

5.5.1 Design III

Here again, the design of the resonator guide was considered first. This time, in order to more accurately hit the filter bandwidth specifications, the layer thickness and index of the silicon nitride deposited wafers were first measured using an ellipsometer. The measured layer thickness and index, 2.18 and $h_c = 398\,\text{nm}$, respectively, were then used to design the filter. The ring radius was kept at $8\,\mu\text{m}$ so as to maintain an $\sim 20\,\text{nm}$ FSR. In order to maintain a high Q with the reduced index, the over-etch depth was increased to $h_{oe} = 192\,\text{nm}$ and the waveguide width to $w_r = 900\,\text{nm}$. At the $8\,\mu\text{m}$ radius, the Q of the TE_{11} mode was calculated to be $250,000$ and the Q of the TE_{21} mode to be ~ 25, both a factor of ~ 2.5 higher than the previous design.

With a higher Q for the TE_{21} mode, minimizing the coupler scattering was a concern. After a few simulations, we realized that the coupler loss could be minimized by reducing the width of the bus waveguide. Example simulations demonstrating this point are provided in Fig. 5-13. Two simulations, one with ring and bus waveguides of equal width $w_r = w_b = 900\,\text{nm}$ (Fig. 5-13a), and another with a reduced bus waveguide width $w_b = 700\,\text{nm}$ were performed. The coupling and the loss for the case of equal widths were found to be $T_{rb} = 0.047$ and $L_{rb} = 0.017$. With the reduced width of the bus waveguide the coupling improves to $T_{rb} = 0.134$ while the loss is reduced to $L_{rb} = 0.007$. The effect is partially explained in the following manner. Reducing the bus waveguide width causes the evanescent field of the bus mode to exhibit a smaller evanescent decay. This enables greater coupling for a given separation of the ring and bus waveguides. And, since the coupler loss is due to a second order interaction with the bus waveguide (i.e. coupling between the TE_{11} and TE_{21}

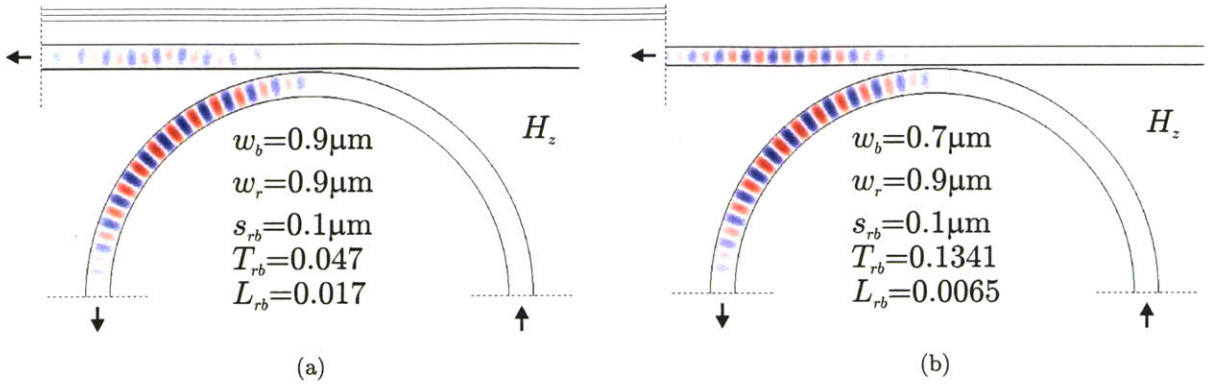

Figure 5-13: Coupler scattering for (a) ring and bus waveguides of equal widths $w_r = w_b =$ 900 nm and (b) for a bus wavegide narrowed down to $w_b = 700$ nm.

modes of the ring induced by the presence of the bus waveguide) the loss relative to the coupling is reduced. What is not answered in this explanation is the reason for the significant absolute reduction in the losses achieved by a simple reduction in the bus waveguide width (Fig. 5-13). One possible explanation for this effect is that the confinement of the TE_{21} mode is enhanced by the added external dielectric of the wider bus waveguide. In a sense the TE_{21} mode of the ring becomes a mode of the combined structure. Evidence for this explanation is provided by the bouncing back and forth of the field in the bus waveguide in Fig. 5-13a. This bouncing is a result of mode beating and cannot occur without the interaction of at least a pair of modes. Irrespective of the justification, this is a highly useful result because it demonstrates that losses in the coupler regions can be minimized without reducing the width of the ring waveguide which would degrade the radiation Q of the ring-mode. Based on the results of Fig. 5-13, a bus waveguide width of $w_b = 700$ nm was chosen and the ring-bus and ring-ring couplings were calculated from FDTD simulations as a function of separation. The results including the loss and coupling induced frequency shifts are provided in Fig. 5-14.

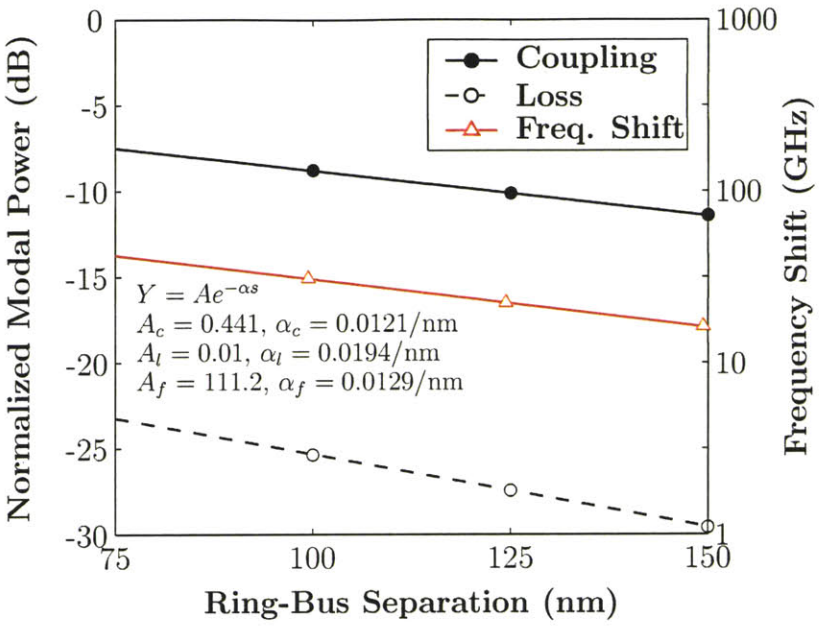

(a)

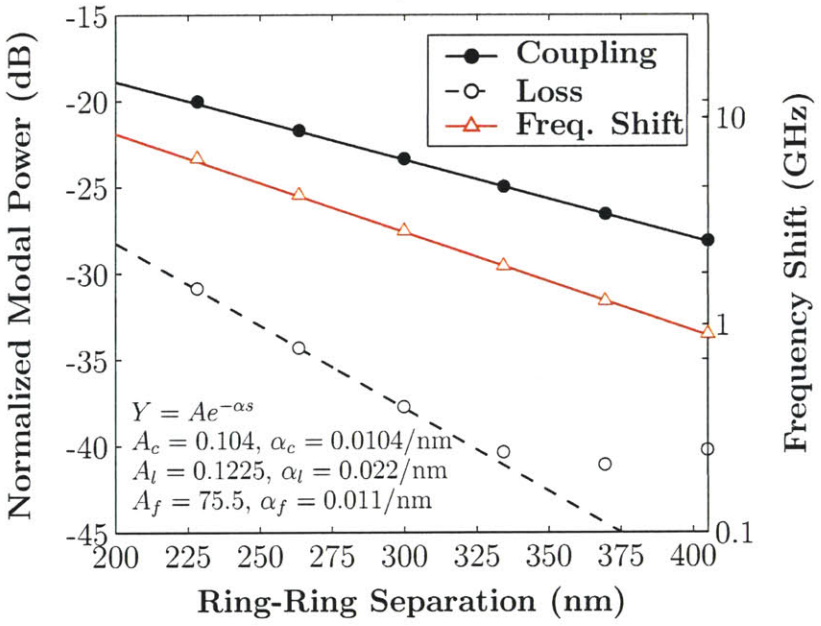

(b)

Figure 5-14: 3D FDTD determined (a) ring-bus and (b) ring-ring coupling, loss, and coupling induced frequency shifts for Design III.

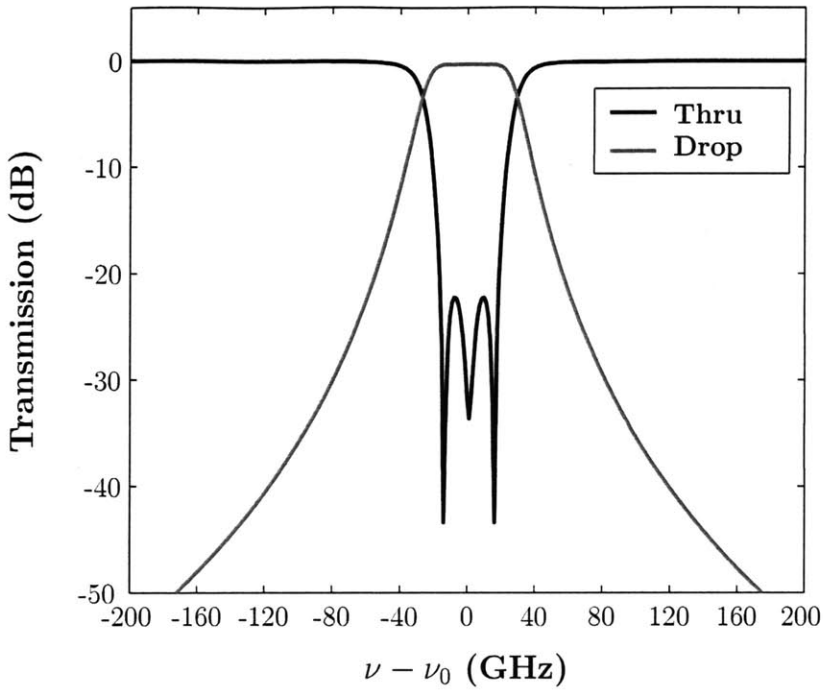

Figure 5-15: Theoretical thru and drop port responses for the CIFS compensated 3^{rd} order microring-resonator of Design III.

Generally, it was desired to improve the filter response over what was obtained in the previous fabrication run. In the prior fabrication run, excess propagation loss contributed heavily to the losses in the filter. Also, the filter response was narrower than necessary. By opening up the bandwidth of the response, the susceptibility to design and propagation losses can be reduced. Here again, a 3^{rd} order filter was chosen. To increase the bandwidth larger ring-bus and ring-ring coupling coefficients of $T_{rb} = 0.103$ and $T_{rr} = 0.22$, respectively, were chosen. A flat passband with a 40 GHz 1 dB filter bandwidth was obtained (Fig. 5-15). Rounded to the nearest e-beam pixel, the chosen coupling coefficients correspond to ring-bus and ring-ring separations of 120 nm and 372 nm, respectively. The design response depicted in Fig. 5-15 demonstrates the improved theoretical losses of the filter design. Now, the coupler scattering based losses were reduced from 0.66 dB to 0.16 dB while the radiation losses were reduced from 0.54 dB to 0.18 dB giving a total theoretical loss of 0.35 dB. The resulting coupling induced frequency shift is $\Delta\nu_{CIFS} = 22.4$ GHz.

5.5.2 Fabrication and Characterization of Design III

The fabrication of the redesigned filter was quite similar to that of Design II. The main differences are the deeper over-etch and characterization of the refractive index and layer thickness prior to design. An e-beam dose matrix was again applied to the center ring of a series of identical filters in order to compensate for the coupling and e-beam proximity effect induced frequency shifts of the rings.

Fig. 5-16 shows measured drop and thru port responses of the frequency-compensated filters. The theoretical response with an added 10 dB/cm loss (extracted from uncompensated filters) is plotted on the same scale of Fig. 5-16b. The only fitted parameters were the center wavelength of 1540.5 nm, and the middle-to-outer ring resonance frequency mismatch of 1.8 GHz. The figure shows close agreement between the intended design and measured result. The only major disprepency appears to be the loss in the drop port which could be due to differences in end facets or measurement uncertainty. With the additional difference in levels subtracted from the theoretical results, the two curves overlap almost perfectly validating the design and demonstrating the accuracy of the fabrication. Improving on design II, the filter has a 40 GHz 1 dB passband with $\sim$ 3 dB drop loss, 30 dB extinction 80 GHz from the center of the passband, and 17.5 dB thru port extinction which represents the highest reported in a high-order microring filter.

The critical parameters affecting the performance of the filter were again measured by Tymon Barwicz using the e-beam lithography system in measure mode for the lateral dimensions, an ellipsometer for the indices and thicknesses, and a profilometer for the etch depth. This time, however, the core layer thickness and index were the same for the design and measurement because they were measured pre-fabrication. While the lateral dimensions show some minor discrepencies when compared to the design, the remarkably close design and measured filter shape are undoubtedly the result of the use of the measured core index and thickness to design the filter.

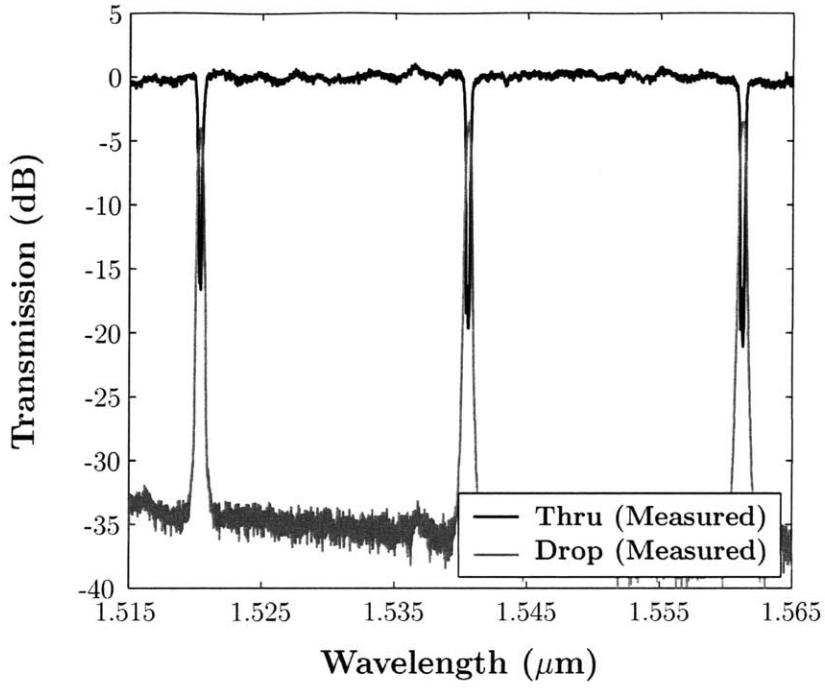

(a)

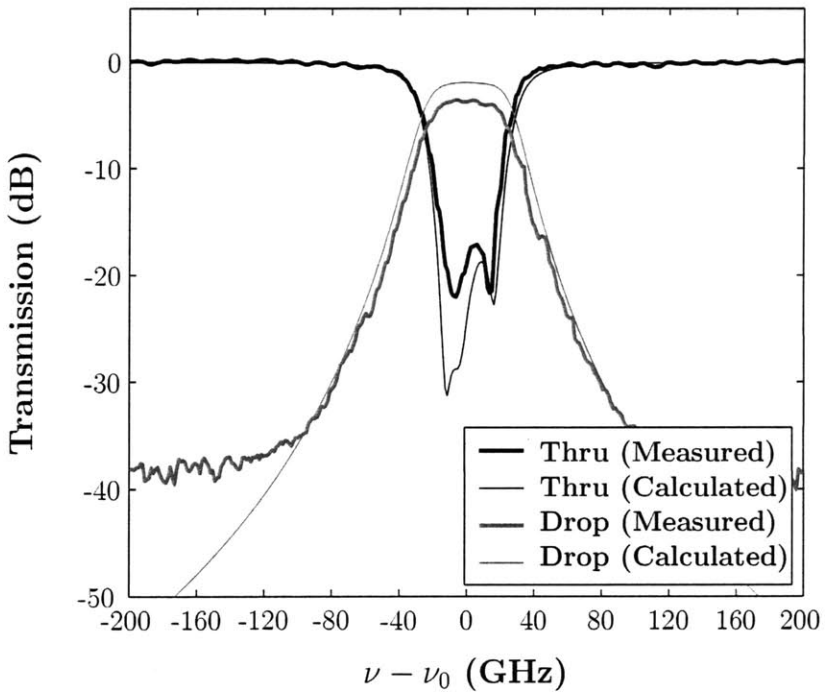

(b)

Figure 5-16: (a) Measured wide-band filter response revealing a 20 nm FSR and (b) measured filter response with calculated filter response superimposed. Calculated response was obtained using device dimensions and indices measured post-fabrication with the transfer matrix approach described in Section 5.2.

Parameter	Designed	Measured
n_c	2.181	2.181
n_{cl}	1.455	1.455
h_{cl}	2530	2530
h_c	400	398
h_{oe}	200	192
w_r	900	920
w_b	700	704
s_{rb}	102	108
s_{rr}	372	362
R	8000	NM

Table 5.4: The dimensions/indices of the fabricated Design III microring resonator filters. Dimensions measured by Tymon Barwicz using the Raith 150 e-beam lithography system in measure mode.

5.6 FSR Doubling through Two-Point Coupling

In the previous three sections, we demonstrated high performance coupled-microring filters. In particular, the measured results of Design III meet nearly all of the requirements listed in Table 5.1. While the required thru port extinction was not met directly, my colleague Milos Popovic demonstrated $> 30\,\text{dB}$ extinction in the thru port by cascading these filters in series [37]. Thus, with the exception of the dispersion which has yet to be designed in or measured, and the free spectral range (FSR), the results of Design III meet all of the passive filter specifications for the R-OADM. The FSR ($\sim 20.4\,\text{nm}$) in fact falls short of the requirements by a factor of ~ 2. And, increasing the index contrast to obtain the required FSR directly would require switching material systems and much tighter tolerances. Vernier schemes have been proposed for extending the FSR [9], however, most of these schemes produce intolerable dispersion into the thru port, or alternatively, make the thru port inaccessible. Here, we consider an approach first proposed by Barbarossa et al. [32] whereby two-point coupling is used to double the FSR of a ring-resonator filter while contributing only a minute amount of dispersion to the thru port at the suppressed resonance. We implement the two-point ring-bus coupling in a second-order microring-resonator filter thereby doubling the FSR and revealing a reasonable path to achieving the required FSR in the silicon nitride material system.

5.6.1 FSR Doubled Filter Design

The basic approach is depicted in Fig. 5-17. A Mach-Zehnder interferometer is formed by coupling to each ring at two points. By setting the differential optical path length of the Mach-Zehnder to $\pi R n_{eff}$, where n_{eff} is the effective index of the ring-mode, the zeros in the transmission response of the Mach-Zehnder fall at every other ring resonance. With no power coupled into the ring, every other resonance is suppressed. Simple geometric consid-

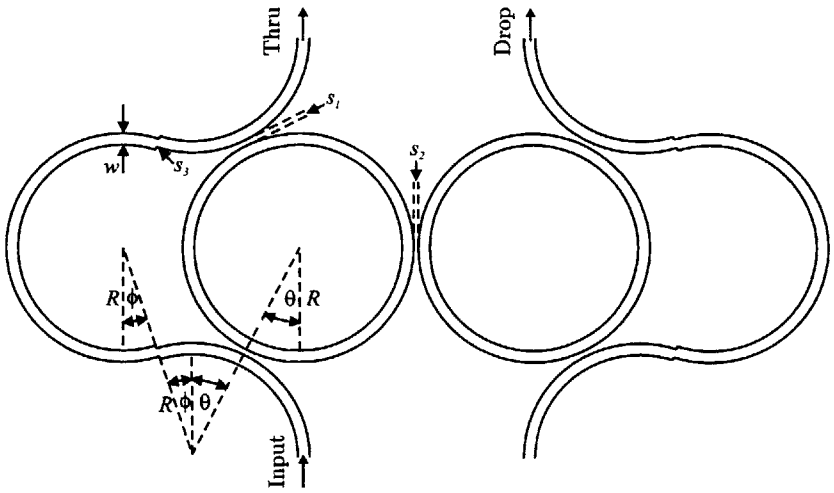

Figure 5-17: Diagram of a second order FSR doubled filter.

erations indicate that the correct path length is arrived at from the following constraints:

$$\theta + \phi = \frac{\pi}{4} \tag{5.12}$$

and

$$\frac{\cos(\theta)}{\cos(\phi)} = \frac{2R + w + s_3}{2(R + w) + s_1} \tag{5.13}$$

where θ and ϕ are the arcs depicted in Fig 5-17, R is the ring radius, w is the waveguide width, s_1 is the separation between the rings and s_3 is a jog placed between the arcs to improve mode-matching. Combining (5.12) and (5.13) we arrive at the following solution for the angle ϕ (5.14).

$$\phi = \tan^{-1}\left[\sqrt{2}\left(\frac{2R + w + s_3}{2(R + w) + s_1}\right) - 1\right] \tag{5.14}$$

A 2^{nd} order filter was chosen because the inherent symmetry of the structure ensures that the rings will have identical frequencies if CIFS and e-beam proximity effects are the only external contributors to resonant frequency shifts of the rings. And, the symmetry of the coupling (i.e. using two-point coupling for both rings) enhances the suppression of the unwanted resonance. On account of the two coupling points, the required ring-bus power coupling per coupling point is approximately 1/4 of its normal value. The total power coupled from the ring to the bus T_{rb} or, by reciprocity, the bus to the ring is

$$T_{rb} = \left| t\sqrt{1-|t|^2} - t \right|^2 \tag{5.15}$$

where $|t|^2$ is the power transmission of a single ring-bus coupler region. Ring-bus and ring-ring power coupling coefficients of $T_{rb} = 0.107$ (i.e. $|t|^2 = 0.027$) and $T_{rr} = 0.004$ were chosen to provide a 40 GHz 1 dB bandwidth and sufficient extinction in both the thru and drop ports when pairs of filters are cascaded in series in both ports (i.e. enabling a squaring of the response curves).

The FDTD results generated for the 3^{rd} order filter design presented in Section 5.5 were used to calculate the ring-bus and ring-ring coupler losses and separations for the FSR doubled 2^{nd} order filter as both of these devices were fabricated on the same wafer. Since the same waveguide width $w_r = w_b = 900\,\text{nm}$ and $R = 8\,\mu\text{m}$ ring radius were chosen and the bus waveguides were formed out of semi-circular arcs, the simulations of the ring-ring couplings presented in Fig. 5-14b provide the necessary data for determining the spacings. Using this data and rounding to the nearest 6 nm pixel on the $x-y$ e-beam grid, ring-bus and ring-ring separations of $s_{rb} = 146\,\text{nm}$ and $s_{rr} = 312\,\text{nm}$ were chosen corresponding to the aforementioned couplings. Based on cylindrical waveguide mode overlaps the offset s_3 in the bus waveguides used to improve the mode overlaps between the oppositely curved bus waveguide sections was chosen to be $s_3 = 52\,\text{nm}$. At this separation, the mode overlap is greater than 99 %.

The theoretical filter responses for the unsuppressed and suppressed resonances, assembled using the transfer matrix method are shown in Fig. 5-18. The ideal case ($\Delta\phi = 0$), exhibits a flat low loss passband in the drop port and more than 18 dB extinction in the thru port of the desired resonance (Fig. 5-18a) while greater than 53 dB suppression is achieved in the unwanted resonance (Fig. 5-18b). In fabrication, the ability to perfectly match the

path lengths of the two arms is limited as a result of variations in the guide geometries due to e-beam proximity effects and discretization errors. To determine just how sensitive the device is to fabrication errors of this sort, responses for filters with differential path lengths were calculated. We can see from Fig. 5-18a that path length variations of upto one-tenth of a wavelength can be tolerated with little impact on either the thru or drop responses of the desired resonance. In contrast, the effect on the suppressed resonance is rather severe (Fig. 5-18b). A change in the path length of 1/40 of a wavelength reduces the suppression from $-53\,\mathrm{dB}$ to as little as $-23\,\mathrm{dB}$. In addition to unwanted phase shifts, differential losses could result due to fabrication errors and thereby hinder the performance of the device. Fortunately, the calculations indicate that differential loss seems to have only a minimal impact on both the desired and suppressed responses (Fig. 5-19). A differential loss of $\sim 1\,\mathrm{dB}$ is needed to significantly impact either resonance. Such a large differential loss is highly unlikely to result from fabrication.

As a final design note, the group delay τ_d and group velocity dispersion D were calculated according to

$$\tau_d = \frac{\partial \phi}{\partial \omega} \tag{5.16}$$

and

$$D = \frac{\partial \tau_d}{\partial \lambda} \tag{5.17}$$

and the results are presented in Fig. 5-20 for both the drop port of the desired resonance and the thru port of the suppressed resonance. For the unsuppressed resonance, the group velocity dispersion and group delay for an equivalent filter employing only a single coupling point to the ring are shown for the drop port resonance. The plot indicates that nearly all of the dispersion in the drop port is a result of the filter itself and not the manner in which it is being coupled to. In the thru port at the suppressed resonance, the dispersion is somewhat affected by the imperfect extinction in the Mach-Zehnder filter slightly off resonance. However, this minor added dispersion is too small to significantly impact the performance of the device.

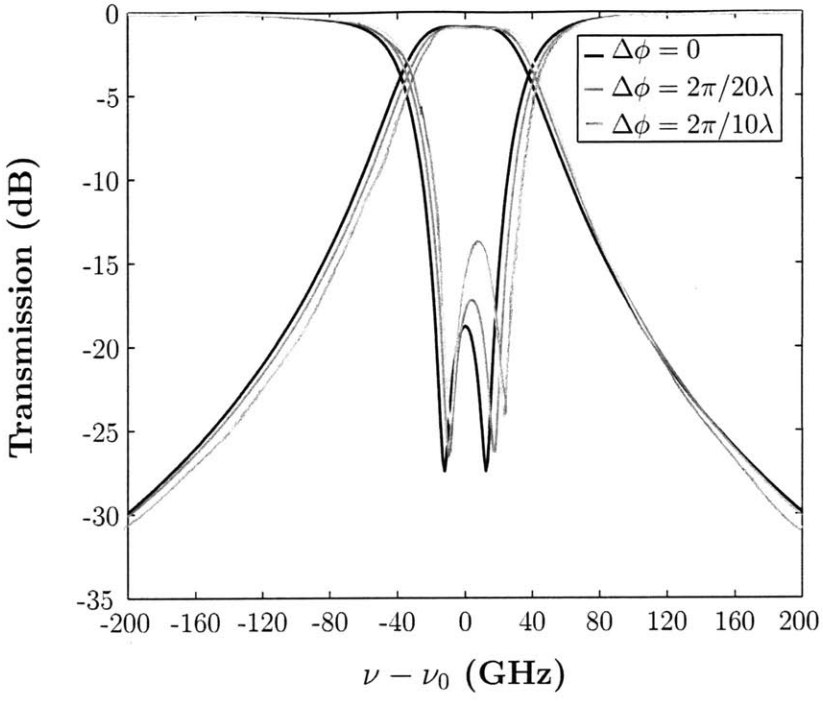

(a)

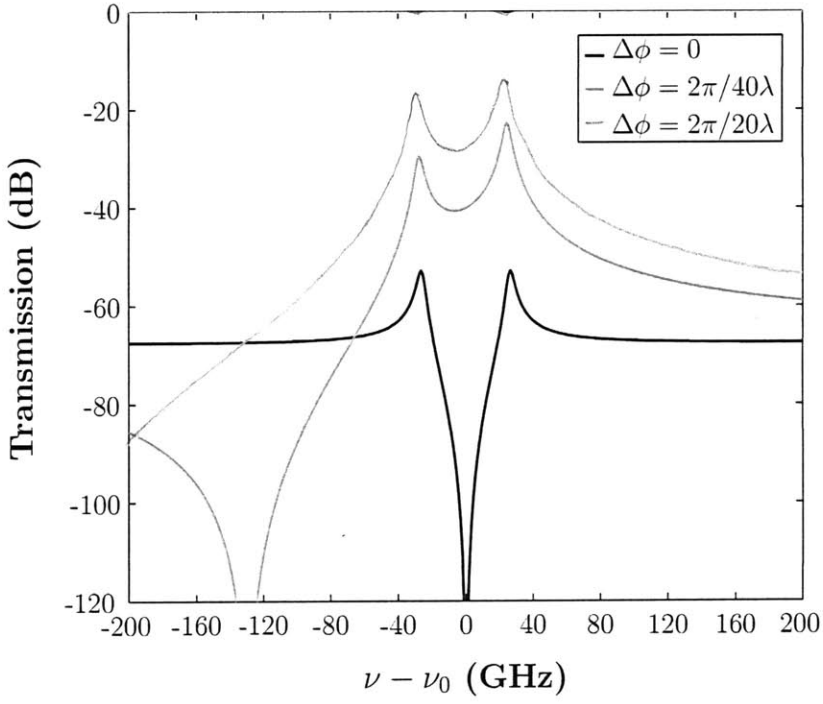

(b)

Figure 5-18: The theoretical filter responses for the (a) unsuppressed and (b) suppressed resonances of the FSR doubled filter depicted in Fig. 5-17 as a function of frequency and error in the differential phase shift $\Delta\phi$ between the arms of the Mach-Zehnder coupler. Note: the unsuppressed and suppressed resonant wavelengths are 1530 nm and 1550.8 nm.

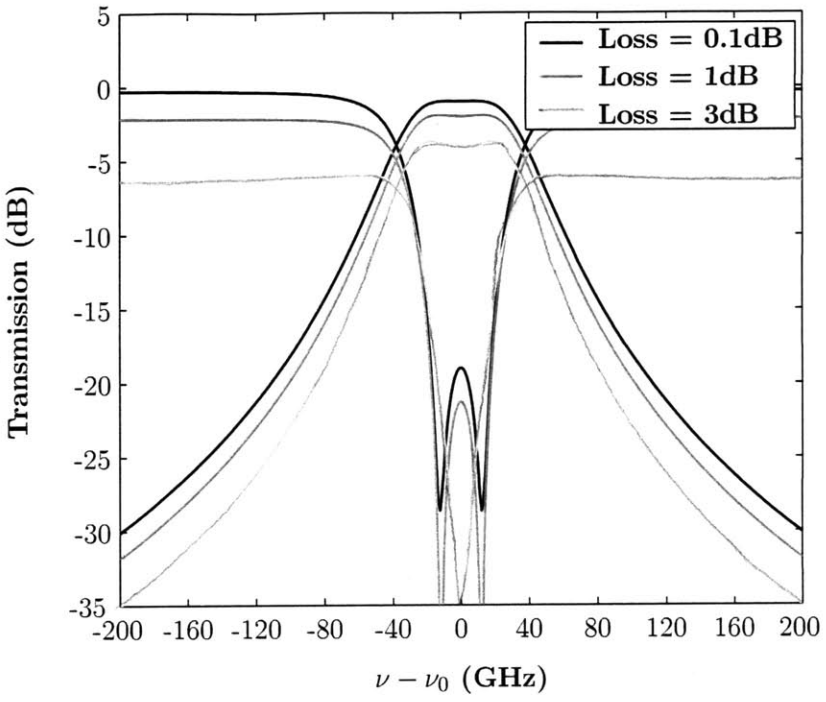

(a)

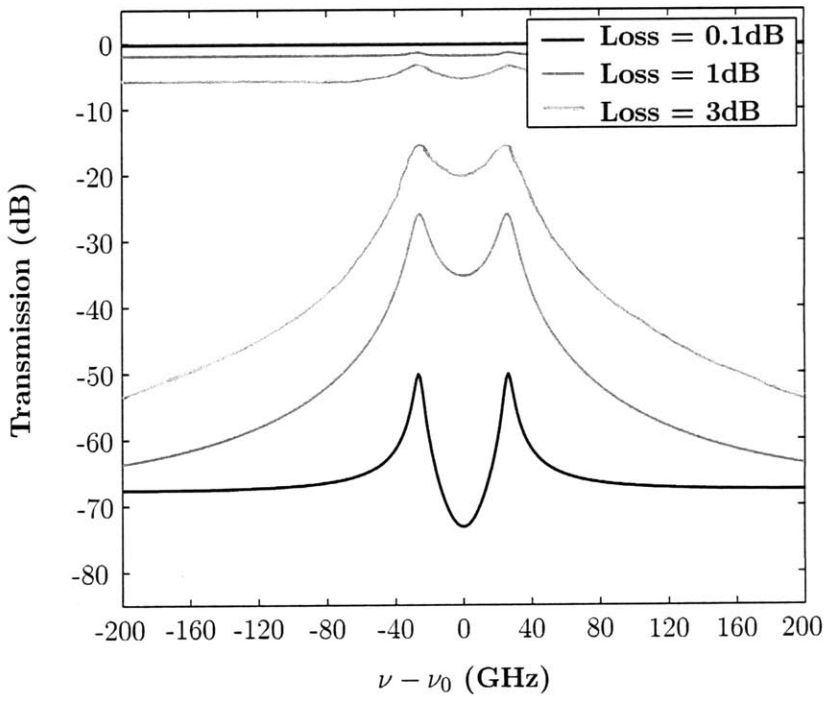

(b)

Figure 5-19: The theoretical filter responses for the (a) unsuppressed and (b) suppressed resonances of the FSR doubled filter depicted in Fig. 5-17 as a function of wavelength and differential loss between the arms of the Mach-Zehnder coupler. Note: the unsuppressed and suppressed resonant wavelengths are 1530 nm and 1550.8 nm.

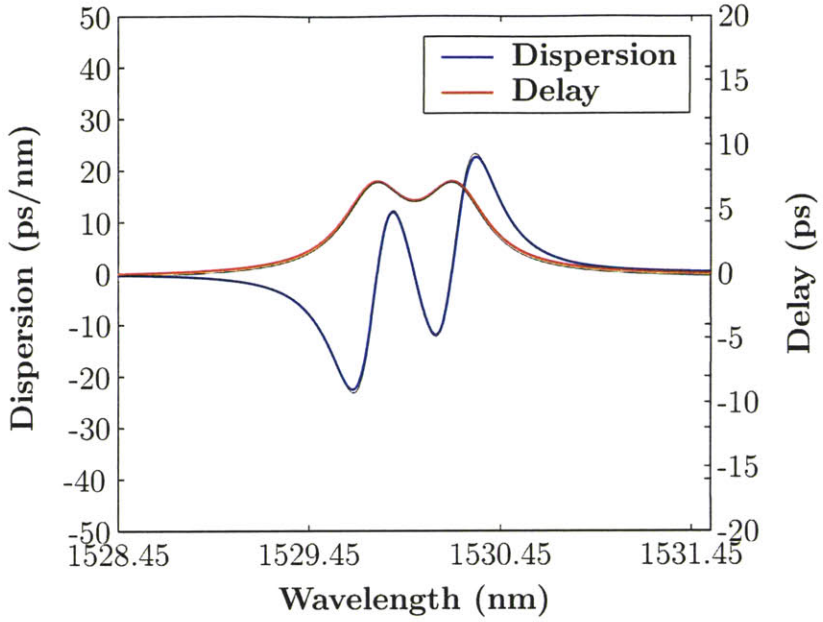

(a)

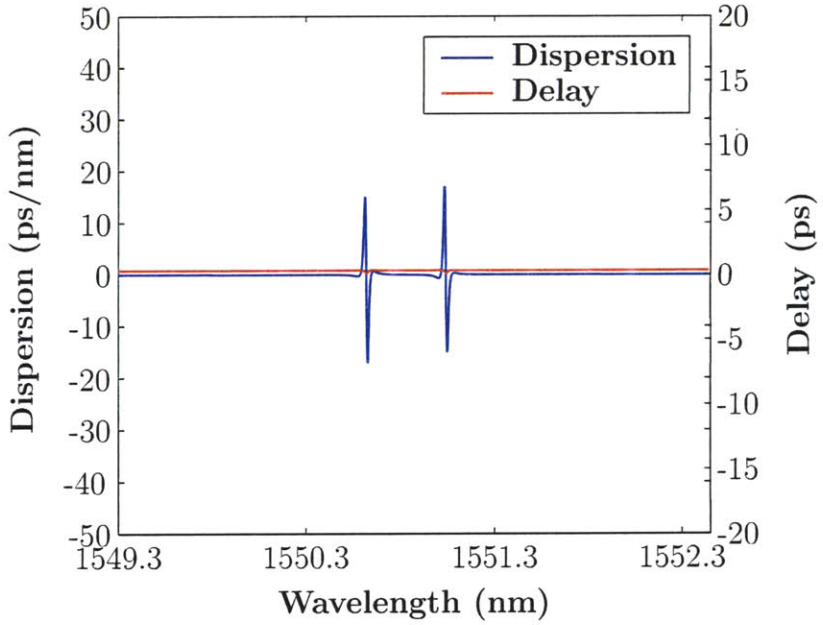

(b)

Figure 5-20: The dispersion and group delay for the (a) unsuppressed drop port response and (b) suppressed thru port response of the FSR doubled filter depicted in Fig. 5-17. The dispersion and group delay for the corresponding filter with a single coupling point is included for the unsuppressed drop port resonance (shown in black).

5.7 Fabrication and Characterization of FSR Doubled Filter

The structures were fabricated in the same fabrication run as the Design III 3^{rd} order filters. In order to compensate for possible differential path length variations, a dose matrix was applied to the bus waveguide arm of the Mach-Zehnder.

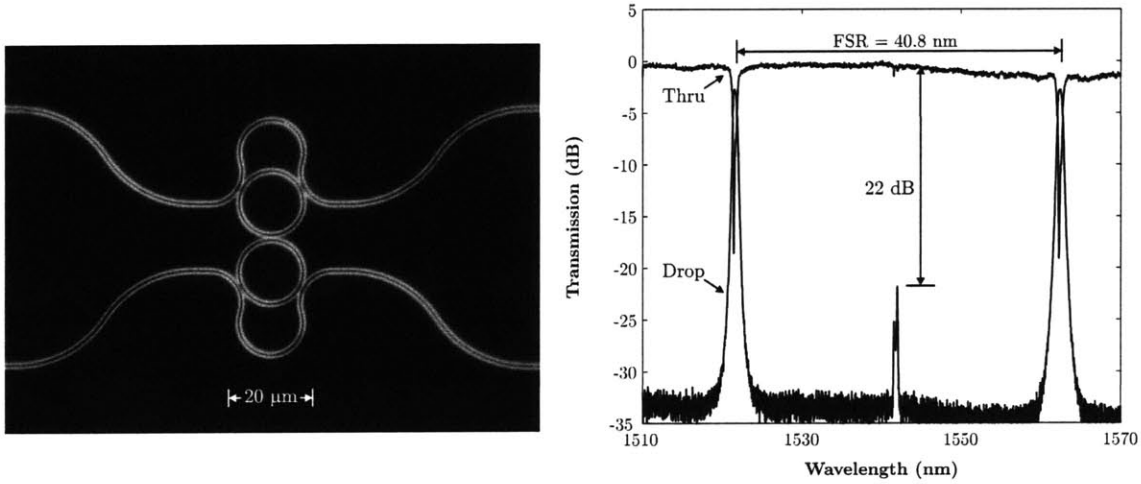

Figure 5-21: (a) A Nomarski optical micrograph of FSR doubled filter. Each bright line represents an edge of the waveguide and (b) the wideband response of the filter demonstrating the achieved 40.8 nm FSR.

A Nomarski optical mircrograph of a fabricated FSR doubled filter is shown in Fig. 5-21a. The measured filter response (shown in Fig. 5-21b) demonstrates an effective 40.8 nm FSR. A close-up of the measured unsuppressed resonance at 1521.6 nm is depicted in Fig. 5-22a. The drop response is similar in both bandwidth and shape to the design with the primary difference being 0.8 dB excess loss (2.5 dB total loss). The thru response exhibits an asymmetry that points to different resonant frequencies for the two rings. This same asymmetry was observed in all fabricated 2^{nd} order filters irrespective of whether one or two coupling points were used. As this asymmetry is highly repeatable and does not appear in third-order filters, it is likely the result of an digital-to-analog-converter error in the Raith 150 e-beam lithography system or some other systematic e-beam write error. A fit to the response using the design couplings with 10 dB/cm loss added in indicates that the asymmetry is due to a frequency mismatch of 23 GHz between the two rings of the filter.

A close-up of the measured suppressed response is depicted in Fig. 5-22b. The drop response was reduced to $\sim$ 22 dB below the thru response or 19.5 dB suppression compared

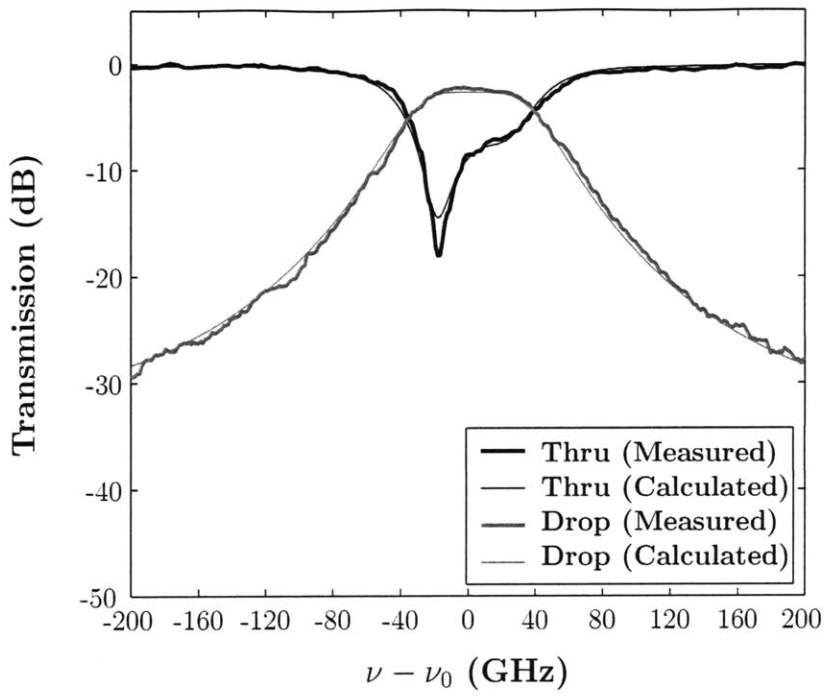

(a)

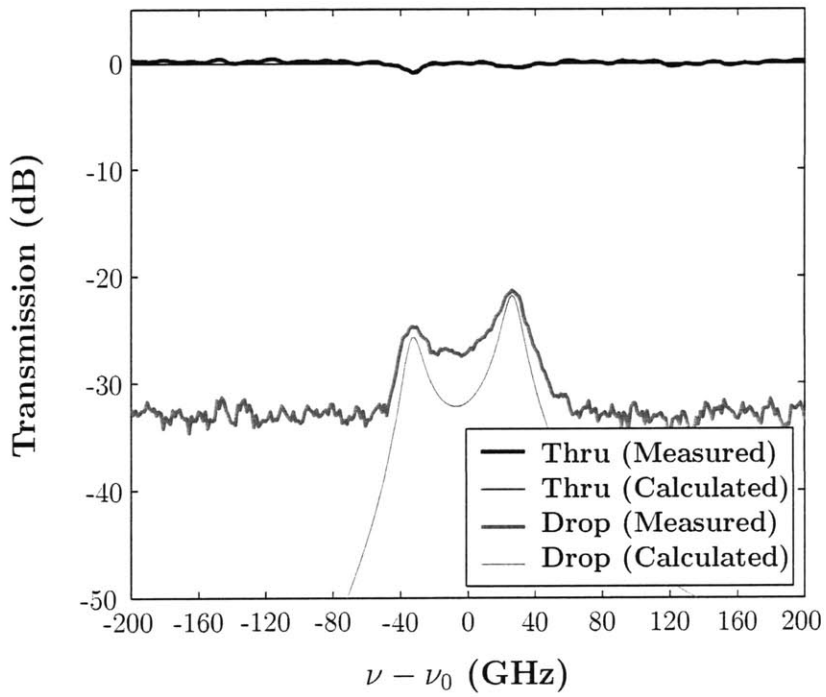

(b)

Figure 5-22: (a) Close-up of desired and (b) suppressed resonances with fitted responses superimposed. Here, 10 dB/cm loss and differential frequency shifts of 23 GHz and 30 GHz between the rings were added to the fitted responses. All other parameters were according to the design.

to the unsuppressed drop response. While short of the 53 dB exhibited by the design response, 22 dB is close to the 28 dB required by the add/drop application. A fitted response using the design couplings is superimposed on the measured response in Fig. 5-22b. The fit indicates that the imperfect extinction is likely the result of a $\sim \lambda/20$ imbalance in the Mach-Zehnder path length. The results of Fig. 5-18 suggest that the suppression might be further reduced by the presence of such a large differential phase shift, however, it turns out that the additional loss in the ring serves to further suppress the unwanted resonance. Fortunately, the imbalance in the path length is systematic and can be easily compensated in fabrication to achieve higher suppressed resonance extinction.

The free spectral range of second-order ring resonator filters was effectively doubled by using two-point coupling to induce a frequency dependence on the filter coupling mechanism. The fabricated devices exhibit a measured extinction in the suppressed resonance of 22 dB. The measured extinction is close to the $\sim$ 30 dB required for the OADM application and represents a major step towards achieving wide FSR ring-resonator-based filters. Moreover, it can easily be improved by more closely matching the path lengths in fabrication.

5.8 Summary

Rigorous three-dimensional electromagnetic simulations were used to calculate the resonant mode, and coupling coefficients for coupled microring resonators filters. A transfer matrix approach using the calculated propagation constants and coupling coefficients was then used to assemble the filter responses. Strong agreement between the measured and design responses, using measured dimensions and indices of an early filter, confirmed the design approach. Using this rigorous approach, a pair of 3^{rd} order filter designs were submitted for fabrication. The first rigorous design/fabrication (Design II) exhibited $\sim$ 6 dB drop loss, 14 dB thru port extinction, and a $\sim$ 20 nm FSR. In the second rigorous design/fabrication (Design III), the drop losses were reduced to $\sim$ 3 dB by reducing losses caused by coupler scattering and radiation and the thru port extinction was improved to $\sim$ 17 dB, yet the FSR was still limited to $\sim$ 20.4 nm. In order to increase the FSR, two-point coupling to the ring was used to suppress every other resonance of a 2^{nd} order microring resonator filter. The approach doubles the realized FSR while introducing little additional dispersion. The fabricated device demonstrated a 40.8 nm FSR with 22 dB suppression of the unwanted

resonances. Combining the results of the 3^{rd} order with the 2^{nd} FSR doubled filter, nearly all the passive OADM specifications have been met. The only remaining specification is achieving a thru port extinction of $\sim 28\,\mathrm{dB}$, which has recently been demonstrated by my colleague, Milos Popovic, using cascaded 3^{rd} order filters [37].

Chapter 6

Integration, Reconfigurability, and Final Remarks

The goal of this reserch was (and still is) to implement a polarization independent optical add / drop multiplexer microphotonic circuit. Thus far, we have reported on the design, fabrication, and demonstration of integrated polarization rotators, splitters, and splitter-rotators along with microring-resonator-based filters. The devices were designed using rigorous electromagnetic simulations and fabricated in the Nanostructures Laboratory using direct write e-beam lithography. All of these devices exhibited very high levels of performance. The polarization splitters and rotators achieved among the highest reported levels of extinction across a 100 nm bandwidth, and the integrated polarization splitter-rotators represent the first demonstrations of a device of this kind. The microring-resonator filters exhibited best-in-class performance achieving 17 dB extinction in the thru port, the largest FSR of a working high-order microring-resonator filter, and a filter shape that closely matched the design. In addition, to achieve the ~ 37 nm FSR required for the OADM application, the FSR of a 2^{nd} order filter was effectively doubled using two-point coupling.

To implement a passive OADM what remains is integration of the demonstrated components. Since both the polarization splitter-rotator and the microring resonator filters were designed to have the same waveguide core layer thicknesses, from a conceptual standpoint, the integration is a relatively straightforward task. Only waveguide crossings need to be designed and the circuit layed out. Doing so will complete our demonstration of a polarization

independent microphotonic circuit. While at the time of this publication, the micropotonic circuit has yet to be implemented, the full circuit design has been completed and submitted for fabrication. The details of the circuit are included herein for completeness.

As a final note, the ultimate goal of this work is to demonstrate a reconfigurable optical add/drop multiplexer (R-OADM). While much work remains in the development of a reconfigurable solution, some initial thoughts about what can and cannot be achieved have been developed. We touch upon these ideas in the hope that a future student will pick up where we have left off.

6.1 Polarization Independent OADM Microphotonic Circuit

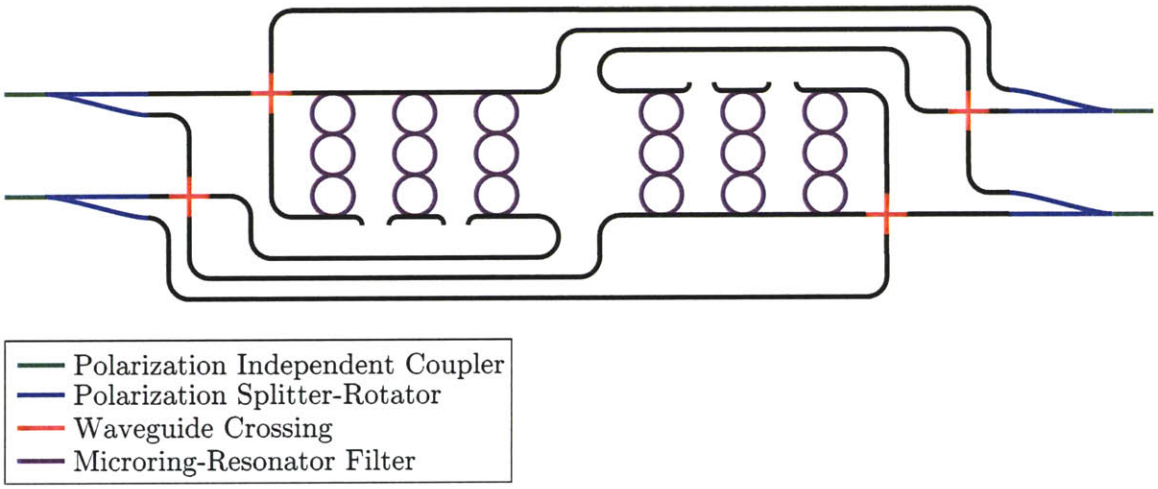

Figure 6-1: A schematic of the polarization independent microphotonic circuit currently being fabricated. Note: the circuit is not drawn to scale and minor details have been omitted to enable the circuit to be fit in the available space.

A schematic of the polarization independent OADM microphotonic circuit, developed in conjunction with Tymon Barwicz and Milos Popovic, is depicted in Fig. 6-1. An important feature of the circuit is that both paths of the circuit see identical sets of devices and path lengths which ensures minimal polarization dependent loss (PDL) and polarization mode dispersion (PMD). Another obvious concern is whether the filter banks will possess overlapping filter functions. However, recent results on multistage filters clearly indicate that if the filters are in close proximity, their resonances will be very closely aligned [37]. Most concerns along these lines have been well thought out and so we feel quite confident

that the circuit will perform at or near the specifications set out by our sponsor with the exception of the free spectral range. In order to minimize the complexity of the circuit for the first fabrication run, we have opted to hold off on implementing the two-point coupling in these 3^{rd} order filters. As it is, the circuit includes integrated polarization splitter-rotators, cascaded microring-resonator filters, waveguide crossings, and polarization independent couplers. The details of these components are included herein for completeness.

The layer thickness of the silicon nitride layer on the wafer chosen for the fabrication is $h_{c1}+h_{c2} = 840\,\text{nm}$ with a goal of obtaining equal upper and lower core layer thicknesses (i.e. $h_{c1} = h_{c2} = 420\,\text{nm}$). The refractive index of the core layer was measured to be $n_c = 2.193$ and that of the cladding to be $n_{cl} = 1.455$. The design of the polariztion splitter-rotator was left largely unchanged with the only differences being the lengths of the polarization splitters and rotators were set to $L_R = L_S = 300\,\mu\text{m}$ and an additional splitter arm was added to the output of the rotator on the input polarization splitter-rotator to improve the extinction of the polarization rotator arm of the device.

The filters are very similar to those of Design III presented in Chapter 5. A $Q \sim 285,000$ was achieved for the 53^{rd} resonance at a wavelength of $\lambda_{53} = 1550\,\text{nm}$ with a free spectral range of FSR $= 20.8\,\text{nm}$ using an outer ring radius of $R = 8\,\mu\text{m}$ and ring guide width of $w_r = 880\,\text{nm}$. Initial test structures fabricated by Tymon Barwicz indicated that a separation of less than 150 nm would be difficult to achieve with the two-layer process. So, in order to increase the ring-bus separation, the bus waveguide was narrowed down to $w_b = 600\,\text{nm}$. FDTD simulations of the ring-bus coupling region revealed that a separation of $s_{rb} = 160\,\text{nm}$ was sufficient to produce a coupling of $T_{rb} = 0.107$ with a coupling loss of only $L_{rb} = 0.0015$. A ring-ring coupling of $T_{rr} = 0.0021$ was achieved with a separation of $s_{rr} = 396\,\text{nm}$. The filter response was assembled using the transfer matrix approach. The results are presented in Fig. 6-2. With less coupler scattering, the theoretical losses have been reduced to $< 0.15\,\text{dB}$.

Waveguide crossings are necessary in order to recombine the outputs of the two sets of filters. Simple crossings were formed from the intersection of orthogonally oriented waveguides, by adiabatically widening the waveguides prior to the point of intersection in order to limit the adverse effects of diffraction (Fig. 6-3a). Simple two-dimensional simulations (Fig. 6-3b) of a waveguide with similar effective index contrast indicates that a waveguide width of $3\,\mu\text{m}$ limits the induced cross-talk and loss to $< -54\,\text{dB}$ and $< -0.25\,\text{dB}$. A

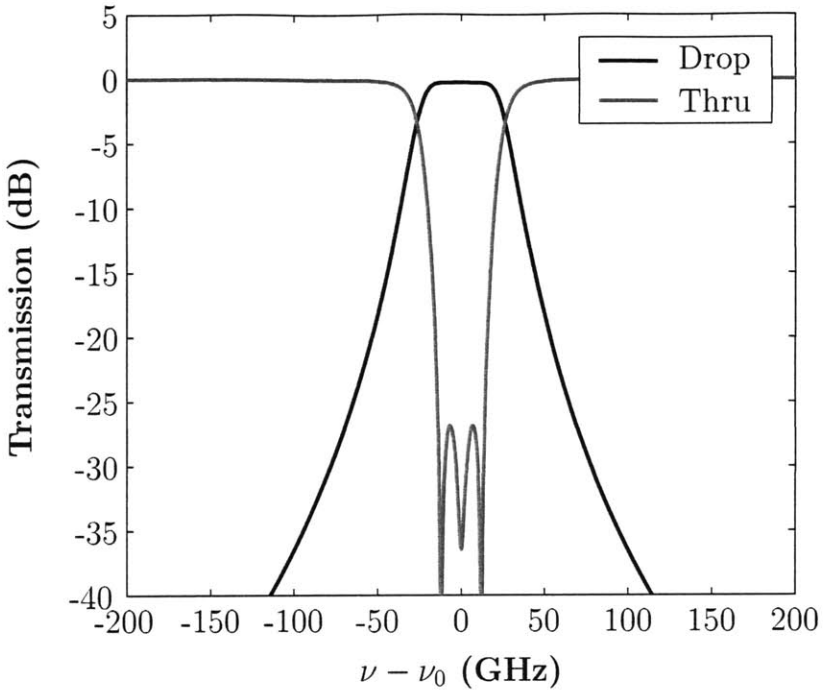

Figure 6-2: The theoretical response for the filter being used in the polarization independent microphotonic circuit. Note: The response is only for a single filter stage.

three-dimensional simulation using the actual guide dimensions and indices indicates that cross-talk and loss levels of $< -48\,\mathrm{dB}$ and $< -0.29\,\mathrm{dB}$, respectively, should be achieved. And, EME simulations indicate that a transition length of $150\,\mu\mathrm{m}$ is sufficient to ensure a nearly lossless transition. As a final point, polarization independent couplers were added to the chip inputs and outputs so as to limit polarization dependent effects of the coupling and collection apparatus. The couplers start with waveguides that exhibit little to no polarization dependence when coupled to circularly symmetric waveguides. A simple taper of the upper core material is then made to transition to the polarization splitter input waveguide. The basic structure is depicted in Fig. 6-4. EME simulations indicate that a taper length of only $\sim 25\,\mu\mathrm{m}$ is needed to ensure a nearly lossless transition.

The OADM formed from the polarization independent microphotonic circuit is currently being fabricated and we eagerly anticipate the results. If all goes well, we expect this circuit will represent the first fully integrated polarization diversity scheme.

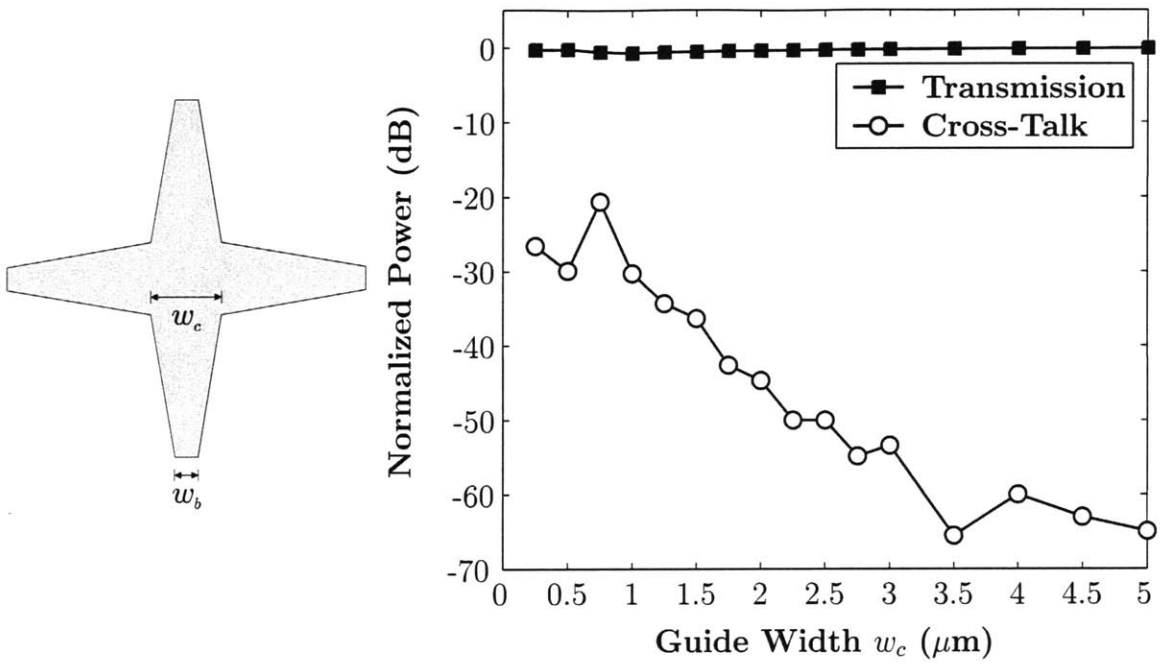

Figure 6-3: (a) A schematic of the simple waveguide crossing used in the microphotonic circuit and results of (b) two-dimensional FDTD simulations of a waveguide crossing as a function of guide width. For the simulations, the core and cladding indices were set to $n_c = 1.8$ and $n_{cl} = 1.0$.

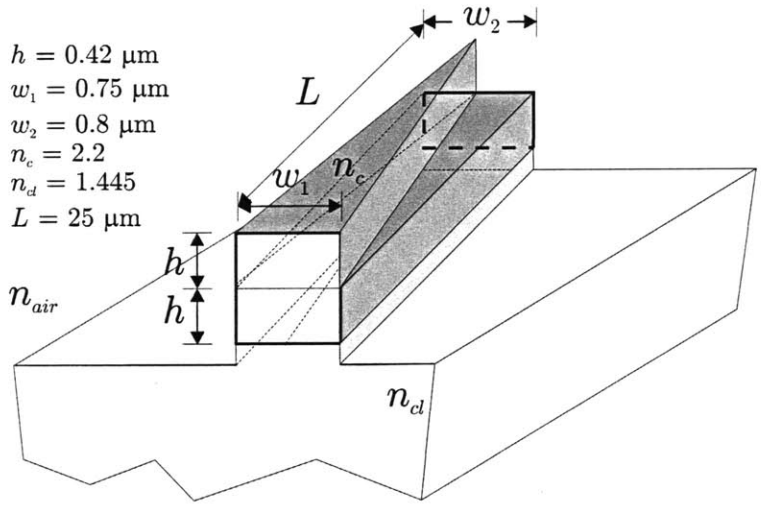

Figure 6-4: The polarization independent coupler used to couple to the circularly symmetric Gaussian mode of the lensed fiber.

6.2 Reconfiguring the OADM

Thus far, we have presented work that has already been, or is about to be fabricated. And, in its current state, the passive OADM is nearly complete. However, the ultimate goal of this project is to implement a reconfigurable OADM or R-OADM. While designs for implementing a R-OADM are far from complete, some initial thoughts have been developed. Here, we finish with some of these ideas in the hope that a future student will pick up where we left off.

As was pointed out to us by our collaborators at Pirelli Labs, one of the most fundamental concerns for reconfiguring an OADM is to ensure that no bits are lost during the transient. That is, the reconfiguration of an OADM must occur in a manner that is transparent to the rest of the signal channels transmitted along the signal path. Doing so is often referred to as "hitless" reconfiguration.

Prof. Hermann Haus (principally), Milos Popovic and I came up with a method for implementing a switch to enable the reconfiguration of the OADM in a hitless manner. A diagram of the switch is shown in Fig. 6-5. The switch works by using a bypass arm to allow for the power to be transferred from one arm of a Mach-Zehnder interferometer to the other. By placing a tunable filter in one arm, and leaving the other as a bypass, the power can be transferred from one arm to the other, allowing the filter to be tuned while no power propagates in the filter arm. After reconfiguration, the power can then be transferred back to the filter arm. However, it is essential that no outages occur during the transient. To do so, a pair of oppositely actuated $\Delta\beta$ couplers can be used to turn the bypass arm on and off. By oppositely actuating the $\Delta\beta$ couplers the phase shift imparted to each arm remains constant at π independent of the state of the $\Delta\beta$ couplers. To ensure that all of the power ends up in the thru port of the switch, an additional π phase shift is needed in the bypass arm. Doing so ensures that all of the thru port power emanates from the thru port of the hitless switch independent of its state.

Alternatively, hitless switching may be accomplished with the two-point coupling approach demonstrated in Chapter 5. Essentially, a π phase shift can be introduced into the bypass arm to switch the state of the coupling. With the coupling turned off, none of the channels see the filter enabling the resonant frequency of the ring to be freely altered. However, it is important to note that FSR doubling and hitless switching cannot both be

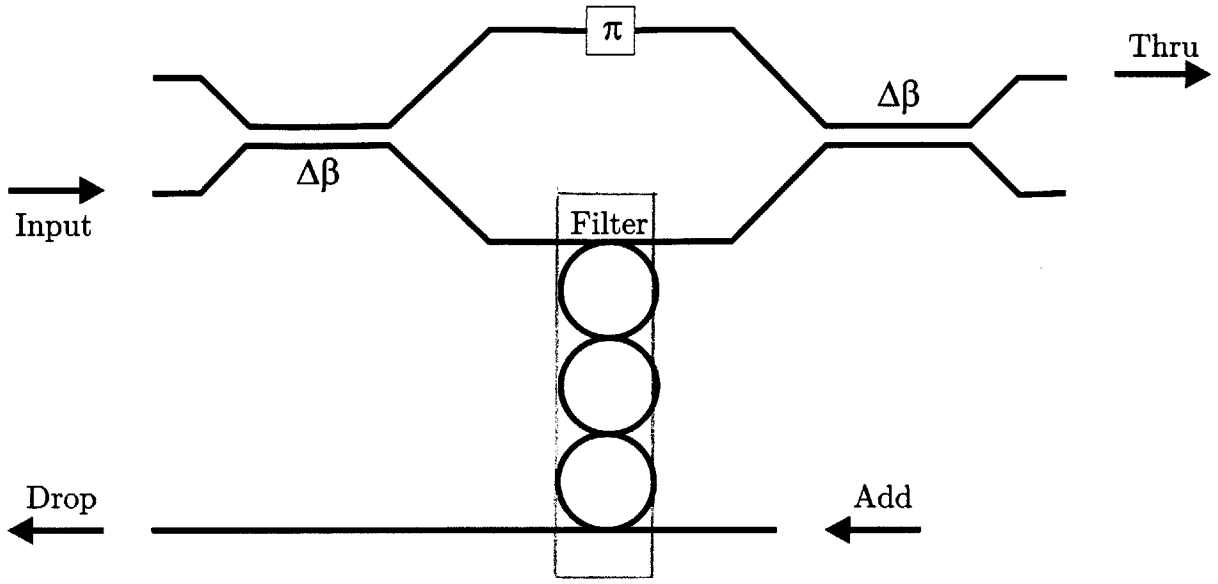

Figure 6-5: The hitless switch proposed by Hermann Haus

achieved with this approach as turning one resonance off inevitably means turning another one on.

While we have come up with a pair of high level approaches for implementing hitless reconfigurable switches, we have yet to address how these switches can be implemented. The bypass switch in either configuration requires substantial changes in the effective index of one of the guides. In either case, reaching the 1^{st} null requires a π phase shift or $\Delta\beta L = \pi$ in one of the guides. Since $\beta = 2\pi n_{eff}/\lambda$, this is equivalent to requiring $\Delta n_{eff} = \lambda/2L$. For a device with a path length $L = 50\lambda$, a $\Delta n_{eff} = 0.01$ is required. This is a change of 1% of the refractive. Few nonlinear effects in any material system can provide such a large change. In addition, while switching a series of cascaded resonators with different resonant frequencies is one possible approach for achieving reconfigurability, it is not the most elegant. Ideally, a single filter could be tuned over the entire 4.5 THz band. Yet, doing so requires a change in the group index of the propagating mode in proportion to the change in the resonant frequency (i.e. $\Delta n_g/n_g \propto \Delta\nu/\nu$) or roughly 2.5%. Non-linear optical materials generally do not afford changes to the refractive index on the order of 1% and even 0.1% is difficult to achieve. More importantly, the materials which offer these relatively large changes in index are often costly to grow and are not directly integratable with silicon electronics.

Alternatively, large changes in the refractive index may be obtained through interaction with the evanescent field of a guided wave. Micro-electromechanical systems (MEMS) make such interactions realizable in integrated structures. However, the perturbed mode must be sufficiently well confined to withstand the strong perturbation offered by evanescent interaction. For this reason, only high index contrast devices can be effectively perturbed in this manner. An example that demonstrates just how large these perturbations can be is presented in Fig. 6-6. The structure uses a waveguide identical to the filter guide (i.e. $h_c = 420\,\text{nm}$, $w = 880\,\text{nm}$, $h_{oe} = 100\,\text{nm}$, $n_c = 2.193$ and $n_{cl} = 1.455$) while the perturbing slab has an index of $n_s = 1.8$ and thickness $h_s = h_c$.

As the slab is moved into and out of the evanescent field of the mode, we find that the modal effective index changes by over 4%, an amount sufficient for both the $\Delta\beta$ and two-point coupling based bypass hitless switch approaches. Additionally, since the group index scales in a manner similar to the effective index, MEMS evanescent interaction is also sufficient for tuning the filter over the required range. The only other mechanism that is capable of achieving such large changes in the effective or group indices is the thermo-optic effect. However, materials with large thermo-optic coefficients ($\sim 10^{-4}/C\circ$) are needed in order for this effect to be useful and even then very large changes in temperature are required ($> 100C^\circ$). Fortunately, such large temperature changes are conceivable in microphotonics due to their small size.

6.3 Summary and Final Remarks

Microphotonic circuits have yet to find their way into applications, in large measure because of the inherent polarization dependence of the high index contrast waveguides required to implement micron-scale optical components. Overcoming this dependence directly in high fidelity applications, although theoretically possible, is often unrealistic. The optical add/drop multiplexer (OADM) is one such application. In this thesis, we considered the implementation of an OADM using high index contrast components, but rather than attempt to achieve polarization independence directly we proposed circumventing the polarization using an integrated polarization diversity scheme.

To implement the polarization diversity scheme, integrated polarization rotators, splitters, and splitter-rotators were developed and their designs verified using rigorous electro-

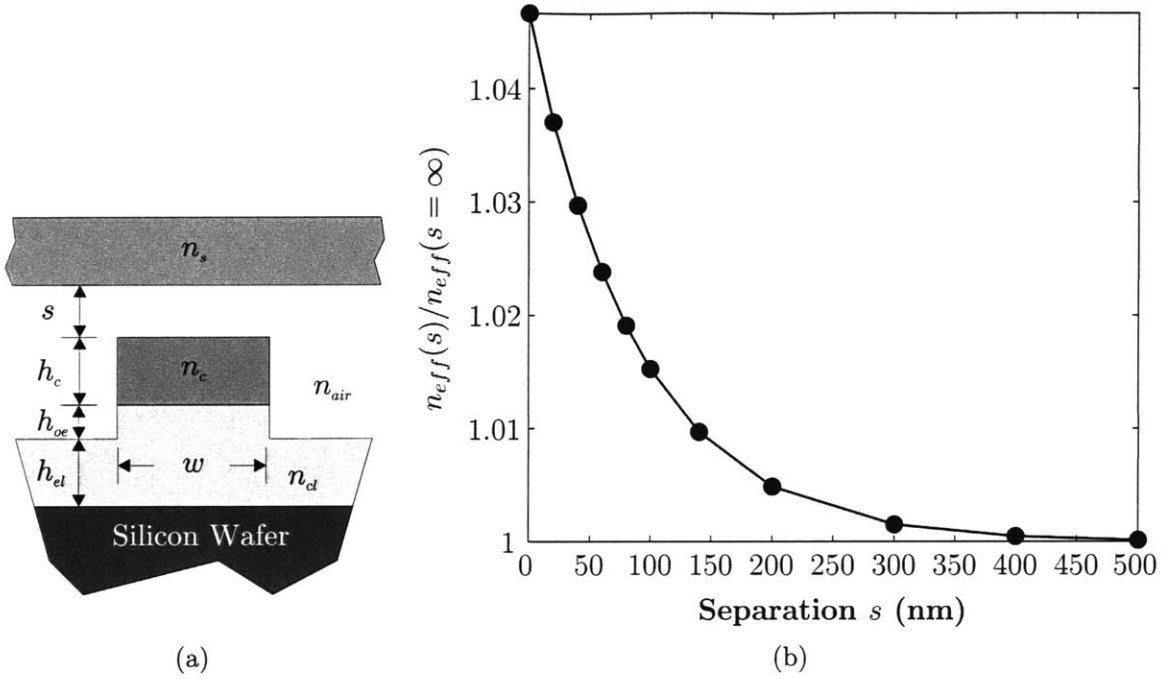

Figure 6-6: Impact on the effective index of a propagating mode as a function of the separation of a MEMS actuated dielectric slab.

magnetic simulations. The structures were then demonstrated in the silicon nitride / silica material system. Both the simulated and measured performance show low loss and low cross-talk over very large bandwidths. The high measured performance was despite substantial variations in the structure geometry and dimensions resulting from e-beam stage drift clearly demonstrating the fabrication tolerance of the mode-evolution approach taken for splitting and rotating polarization on-chip.

In addition, microring-resonator filters were designed using a similarly rigorous approach and the same materials and layer thickness so as to be directly integratable with the polarization splitter-rotator. The devices were subsequently fabricated and the measured performance was shown to closely match the design in terms of both bandwidth and filter response shape. The filters achieved the highest reported levels of thru port extinction and the largest FSR in a high order microring-resonator filter. Augmenting this achievement, the FSR of a second order filter was effectively doubled to 40.8 nm by using two-point coupling to the ring.

To complete this effort, a chip layout for implementing a polarization independent

OADM has been created and passed on for fabrication. The layout includes all necessary components, including variants of the polarization splitter-rotators reported on in Chapter 4 and microring-resonator filters presented in Chapter 5. In addition, the waveguide crossings necessary to recombine the outputs of the parrallel ports of the integrated polarization diversity scheme have been designed. Finally, some basic condsiderations for reconfiguring the OADM have been presented.

Four years ago I presented the integrated polarization diversity scheme as a solution for achieving polarization independence with coupled microring-resonator filters. At the time, we did not have an integrated polarization splitter-rotator solution nor did we know whether high order microring-resonator filters formed from high index contrast materials would work, even from a theoretical standpoint. Through the collaboration of a strong team of students we were able to demonstrate all of the components necessary to implement the circuit. Without this collaboration, the results would only be a shadow of what was ultimately accomplished.

Appendix A

Standing-Wave Resonators of Arbitrary Q

Prior to the work on developing a reconfigurable optical add / drop multiplexer (R-OADM), I spent some time working on standing-wave resonators. High-Q standing-wave resonantors have many possible applications from lasers to filters to nonlinear switches. And often a small modal volume V and high-Q are desired. However, these goals often seem to be diametrically opposed. To minimize radiation in a standing-wave resonator formed from holes in the core of a two-dimensional waveguide, Johnson et al. [42] proposed using careful phasing of radiators to cancel radiation in the far field. In reviewing this work, I asked a different question, that is, does the structure need to radiate at all? Certainly, it seemed difficult to imagine eliminating radiation in a resonator formed from a linear array of holes in a waveguide. However, I thought it might be possible to mode-match alternating high and low effective index layers of a resonator formed from high index contrast waveguides, thereby obtaining a high-Q with a small modal volume V.

Herein, we describe an analytical mode-matching mechanism in two and three dimensions that, in principle, eliminates radiation allowing *arbitrarily* high-Q to be achieved with a bounded modal area/volume on the order of the wavelength squared/cubed. Our mechanism does *not* employ a complete photonic bandgap [43], which, at the expense of complex structures in three dimensions, was the only previously known route to such results [44]. Unlike other designs to improve cavity Q in the absence of a complete bandgap [45, 46, 47, 42, 48, 49], we need not increase the modal volume V as a tradeoff for arbitrarily

high Q. Our V is roughly independent of Q. Rather, scattering and radiation are prohibited by a perfect mode-match of the TE polarized modes in each subsection of a Bragg resonator. Q's in excess of 10^5 are demonstrated through FDTD simulations of two/three-dimensional structures with modal areas/volumes on the order of the wavelength squared/cubed. In the first part of this appendix, we present work that has previously been published [7] and then extend these results to a new three-dimensional geometery that demonstrates these properties.

A.1 Bragg Axially Confined Cavities

When a waveguide mode encounters an interface, there are normally radiation losses. However, if the guided mode in one section can be expressed purely as a linear combination of the forward and backward guided modes of the other section, there will be reflections *without scattering or radiation.* A quarter-wave stack and Fabry-Perot cavity (as in Fig. A-2) can then be constructed through a series of such junctions to trap a mode that decays *exponentially* in all directions. The operating characteristics of the cavity are then completely described by an equivalent one-dimensional system. We demonstrate how to achieve such mode matching with a simple analytic condition on the dielectric constants, and present examples of such high-Q cavities in two and three dimensions. (A similar mode-matching proof, in two dimensions only and without application to cavities, was given in [50] to eliminate losses from index-confined Bragg mirrors.)

A.1.1 Theory

To demonstrate this result, we begin by using the wave equation to develop necessary conditions on both the materials and the modes in order that the junction of two step-index waveguides (depicted in Fig. A-1) be radiation-free. We then show that a superposition of forward- and backward-propagating guided modes entirely satisfies the boundary conditions, precluding any coupling to radiation modes. For guided modes propagating along $\hat{\mathbf{z}}$, the electric field $\mathbf{E}$ in a waveguide has z dependence $e^{-j\beta z}$ and obeys the wave equation:

$$\left(\nabla_T^2 + \mu_0 \epsilon_i \omega^2 - \beta^2\right) \mathbf{E} = 0 \tag{A.1}$$

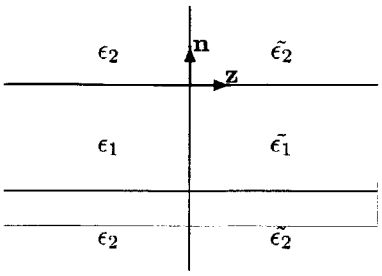

Figure A-1: Schematic junction of two step-index waveguides.

in the piecewise-uniform regions i, where $\nabla_T^2 \equiv \nabla^2 - \partial_z^2$ denotes the transverse Laplacian. Similarly for $\tilde{\mathbf{E}}, \tilde{\beta}, \tilde{\epsilon}_i$ in the second waveguide. Since the magnetic and transverse electric fields must be continuous across the junction, the transverse mode profiles $\mathbf{E}_T$ and $\tilde{\mathbf{E}}_T$ must be *at least* component-wise proportional if the field solutions are to be composed solely of guided modes—so, we require that Eq. (A.1) be the same, and thus $\epsilon_i\omega^2 - \beta^2/\mu_0 = \tilde{\epsilon}_i\omega^2 - \tilde{\beta}^2/\mu_0$. This implies:

$$\epsilon_1 - \epsilon_2 = \tilde{\epsilon}_1 - \tilde{\epsilon}_2 \tag{A.2}$$

Equation (A.2), however, is incompatible with the condition of continuity on $\hat{\mathbf{n}} \cdot (\epsilon_i \mathbf{E}_i)$, except in the trivial case of $\epsilon_i = \tilde{\epsilon}_i$ or when the normal component of the $\mathbf{E}_i$ is *zero*. Therefore, we immediately restrict our attention to the case where (A.2) is satisfied and the electric field is TE (transverse electric, *i.e.* purely parallel to the waveguide walls).

Under these conditions, the transverse electric fields in the two waveguides satisfy the same differential equations and have the same boundary conditions, and therefore permit identical (or proportional) solutions. It remains to be shown that a superposition of only these guided modes satisfies *all* the boundary conditions at the junction. For this, we must include the magnetic field, whose transverse components are given by Faraday's Law in the TE case:

$$\hat{\mathbf{z}} \frac{\partial}{\partial z} \times \mathbf{E}_T = -j\omega\mu_0 \mathbf{H}_T = -j\beta \hat{\mathbf{z}} \times \mathbf{E}_T. \tag{A.3}$$

Now, we take as a trial solution a superposition of a forward and a backward propagating mode in the left-hand waveguide and a single forward propagating mode in the right-hand waveguide. At the boundary, it is necessary and sufficient that the transverse field profiles be continuous, and thus:

$$\mathbf{E}_T(1 + r) = t \cdot \mathbf{E}_T \tag{A.4}$$

$$\mathbf{H}_T(1-r) = t \cdot \mathbf{H}_T \tag{A.5}$$

where $|r|^2$ and $|t|^2$ are the reflection and transmission coefficients. By applying Eq. (A.3) to Eq. (A.5) and solving for r, given from above that the transverse electric-field profiles are proportional, we find that all boundary conditions are satisfied with the usual reflection coefficient [45]:

$$r = \frac{n_{eff} - \tilde{n}_{eff}}{n_{eff} + \tilde{n}_{eff}}, \tag{A.6}$$

for the effective indices $n_{eff} \equiv \frac{\beta c}{\omega}$. That is, the *unique* solution of Maxwell's equations consists of forward- and backward-propagating modes of normalized amplitudes 1 and r, respectively, in the left-hand guide; and a single forward-propagating mode in the right-hand guide of normalized amplitude $t = 1 + r$.

In summary, we have shown that if Eq. (A.2) is satisfied and the excited mode is purely TE, all boundary conditions at the junction are necessarily satisfied by guided-mode solutions and the junction is radiation-free. In two dimensions, one can always choose the electric field to be TE polarized (polarization everywhere out of the plane in Fig. 1). In three dimensions, for *cylindrical* waveguides, the "azimuthally polarized" $\mathrm{TE}_{0\ell}$ modes are purely TE: their polarization is everywhere directed along $\widehat{\phi}$ (parallel to the walls). Because there are only reflections, the system is effectively one-dimensional and so a quarter-wave stack (thicknesses $\pi/2\beta$ and $\pi/2\tilde{\beta}$) with a quarter-wave defect [51] can be used to optimally confine light in the axial direction without sacrificing lateral confinement or Q. In fact, the only limitations on the cavity Q will result from the limited number of Bragg layers and the finite extent of the cladding, as well as fabrication imperfections.

A.1.2 Numerical Results

The above theory is *exact*, but we also present numerical results to illustrate the theory and the effects of finite system size. We first consider the two-dimensional structure, depicted in Fig. A-2, comprising a quarter-wave stack of waveguides with a quarter-wave Fabry-Perot defect in the center of the structure, with N Bragg bilayers on either side. The core width a is arbitrary, but here it was chosen to ensure single-mode guidance and satisfies $a/\lambda = 0.2839$. The indices were chosen to satisfy Eq. (A.2), with indices $n_1 = 3$, $n_2 = \sqrt{6}$, $\tilde{n}_1 = 2$, and $\tilde{n}_2 = 1$; the associated effective indices of the guide sections were calculated to be $n_{eff} \cong 2.8141$ and $\tilde{n}_{eff} \cong 1.7086$. The field (Fig. A-2) and its Q were computed by

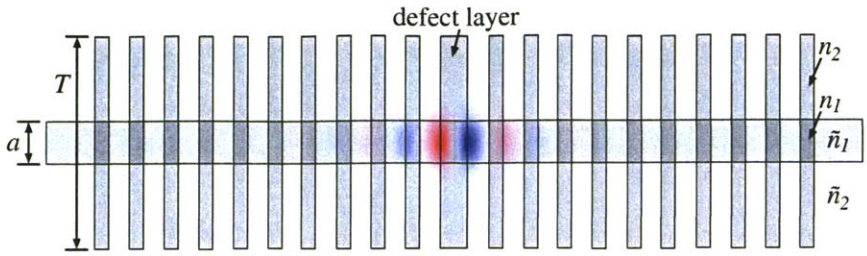

Figure A-2: A two dimensional $(x - z)$ Fabry-Perot cavity, with ϵ in grayscale, confining a TE mode whose field E_y is shown as blue/red for negative/positive. The cavity consists of alternating index-guided waveguides with core/cladding indices n_1/n_2 and $\tilde{n}_1/\tilde{n}_2$, where the core has width a and the n_2 regions have finite width T. The indices satisfy Eq. (A.2), which ensures zero radiation losses at the waveguide interfaces.

finite-difference time-domain (FDTD) simulation [21]. Two variations of the structure were considered: one with $N = 10$ bilayers and the other with $N = 15$ bilayers. In each case, the cladding width T was varied and the cavity Q was determined from the energy decay in the cavity. The Q's increase nearly exponentially with the cladding width (Fig. A-3) until maxima are reached. Comparisons with the Q's of one-dimensional stacks with the same effective indices reveal that the maximum Q's obtained in the simulations are precisely those of the equivalent one-dimensional structures, thereby demonstrating that the Q's are limited only by N when the lateral extent of the structure is sufficient. In addition to the Q, the modal area of this structure $A \sim (0.31\lambda)^2$ was calculated according to the definition $A = \int \epsilon |\mathbf{E}|^2 dA / \max(\epsilon |\mathbf{E}|^2)$ [52, 53].

Similar results are possible in three dimensions by employing *e.g.* the TE_{01} mode of a cylindrical structure. A schematic of such a structure is depicted in Fig. A-4. Here, again, we consider a quarter-wave stack with a quarter-wavelength defect and the same indices as in our two-dimensional example. In this case, we employ a shorter wavelength (or a larger core diameter a) with $a/\lambda = 0.5182$ in order to support a TE_{01} mode, since this mode is not fundamental. The effective indices of the TE_{01} mode are then $n_{\mathrm{eff}} \cong 2.518$ and $\tilde{n}_{\mathrm{eff}} \cong 1.158$. We again measure the cavity Q as a function of N and T via FDTD simulations and the results are shown in Fig. A-3. On account of the higher effective-index contrast, only $N = 10$ is required to achieve a Q of over 10^5 (with a cladding diameter $T = 6a$). The modal volume V [52, 53] of the structure was calculated and found to be $V \sim (0.406\lambda)^3$.

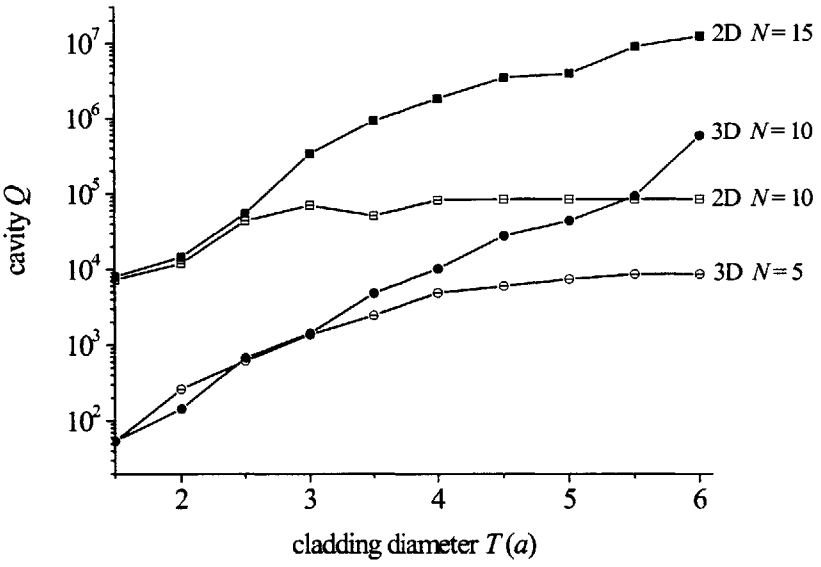

Figure A-3: Q as a function of cladding thickness T for the two-dimensional cavity of Fig. A-2 and the three-dimensional cavity of Fig. A-5, for different numbers N of Bragg periods on either side of the cavity. Q increases exponentially with T or N, depending upon which one is limiting the Q.

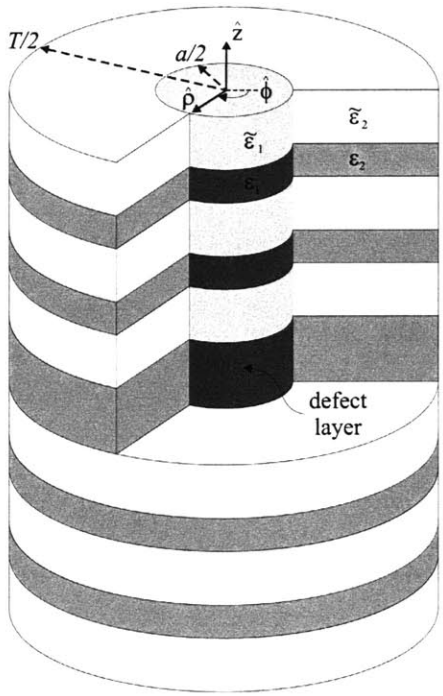

Figure A-4: Schematic of a three-dimensional Fabry-Perot cavity consisting of alternating index-guided cylindrical waveguides stacked in the z direction with core/cladding indices n_1/n_2 and $\tilde{n}_1/\tilde{n}_2$, where the core (seen in cutaway at top) has diameter a and the cladding has diameter T. When the indices satisfy Eq. (A.2), the TE_{01} mode does not radiate at the waveguide interfaces.

A.2 Bragg Radially Confined Cavities

It turns out that the three dimensional cavity depicted in Fig. A-4 is not the only three-dimensional geometry that is radiation-free. Cylindrical Bragg cavities extending radially outward can be used to confine an electromagnetic field in the radial direction while index guiding is used to confine the field in the axial direction. However this again requires the electric field be purely TE, and the layers forming the Bragg stack again satisfy (A.2). Radiation is again eliminated at the interface by virtue of mode-matched fields amongst the layers. This second three-dimensional geometry is depicted in Fig. A-5.

A.2.1 Theory

The proof that this approach remains valid is analogous to that presented in Section A.1. We begin by considering the scalar wave equation for the H_z field in cylindrical coordinates (A.7).

$$\left(\frac{\partial^2}{\partial\rho^2}+\frac{1}{\rho}\frac{\partial}{\partial\rho}+\frac{1}{\rho^2}\frac{\partial^2}{\partial\phi^2}+\frac{\partial^2}{\partial z^2}+\omega^2\mu\epsilon_i\right)H_z=0 \tag{A.7}$$

The derivatives in z and ϕ must be the same because the fields must be at least component-wise proportional for the boundary conditions to be matched by guided modes. This leads to the following requirement

$$\left(\frac{\partial^2}{\partial\rho^2}+\frac{1}{\rho}\frac{\partial}{\partial\rho}+\omega^2\mu\epsilon_i\right)=\left(\frac{\partial^2}{\partial\rho^2}+\frac{1}{\rho}\frac{\partial}{\partial\rho}+\omega^2\mu\tilde{\epsilon}_i\right) \tag{A.8}$$

which again implies that (A.2) must hold for the boundary to be radiation-free. Here again, equation (A.2), is incompatible with the condition of continuity on $\widehat{\mathbf{n}}\cdot(\epsilon_i\mathbf{E}_i)$, except in the trivial case of $\epsilon_i=\tilde{\epsilon}_i$ or when the normal component of the $\mathbf{E}_i$ is *zero*. Therefore, we again immediately restrict our attention to the case where (A.2) is satisfied and the electric field is TE or purely ϕ-directed. Under these conditions, the transverse electric fields in the respective Bragg layers satisfy the same differential equations and have the same boundary conditions, and therefore permit identical (or proportional) solutions. It again remains to be shown that a superposition of only these guided modes satisfies *all* the boundary conditions at the junction. For this, we must again include the magnetic field, whose transverse components are given by Faraday's Law in the TE case for a radially

propagating field:

$$\hat{\mathbf{z}}\frac{1}{\rho}\frac{\partial}{\partial\rho}\rho\times\mathbf{E}_T=-j\omega\mu_0\mathbf{H}_T=-j\beta_\rho(\rho)\hat{\rho}\times\mathbf{E}_T \tag{A.9}$$

where we have denoted $\beta_\rho(\rho)=\left(\frac{j}{\hat{\rho}\times\mathbf{E}_T}\frac{\partial\hat{\rho}\times\mathbf{E}_T}{\partial\rho}+\frac{1}{\rho}\right)$. We find that the transverse components of the electric and magnetic fields again satisfy (A.4) and (A.5) with a reflection coefficient given by (A.6) with n_{eff} replaced by $n_{eff}(\rho)=\frac{\beta_\rho(\rho)c}{\omega}$.

As a final point, it is necessary to consider the solutions for the electric and magnetic fields in order to properly design the cavity. With no ϕ dependence, the cylindrical wave equation (A.7) simplifies to

$$\left(\frac{\partial^2}{\partial\rho^2}+\frac{1}{\rho}\frac{\partial}{\partial\rho}+\frac{\partial^2}{\partial z^2}+\omega^2\mu\epsilon_i\right)H_z=0 \tag{A.10}$$

which is seperable and takes the form $H_z=\psi(r)e^{-jk_{z_i}z}$ with general solutions given by

$$\psi(\rho)=AJ_0(h\rho)+BY_0(h\rho) \tag{A.11}$$

where $J_0(h\rho)$ and $Y_0(h\rho)$ are Bessel functions of the first and second kind of order zero, respectively, and $h^2=\omega^2\mu\epsilon_i-k_{z_i}^2$. Since Y_0 blows up at $\rho=0$, B must be zero in the cavity defect leaving the field solutions to be simply of the form $\psi(\rho)=AJ_0(h\rho)$. To maximally confine the field, an analogy is made with the axially confined cavity. Interfaces are placed at electric field maxima, which in the case of all but the first maxima of the Bessel function J_0 correspond closely to a $\lambda/4$ spacing. Since the electric field must be continous at $\rho=0$, it must in fact be zero because of the 180° change in direction across the $\hat{\phi}$ boundary. Meeting this condition with a high index contrast central defect requires placing the first boundary ρ_0 at the 1^{st} zero of the Bessel function (i.e. $h\rho_0=2.4048$).

A.2.2 Numerical Results

To use Bragg layers to radially confine the field to form a resonant cavity with arbitrary Q in two-dimensions only requires a proper choice of the layer thicknesses and a sufficient number of layer pairs. The condition (A.2) on the dielectric constants need not be followed as two dimensional confinement is provided by the Bragg layers alone. While somewhat trivial for comparision with the three dimensional case it is worthwhile to construct such a two dimensional cavity. To make an exact analogy with the three dimensional resonator

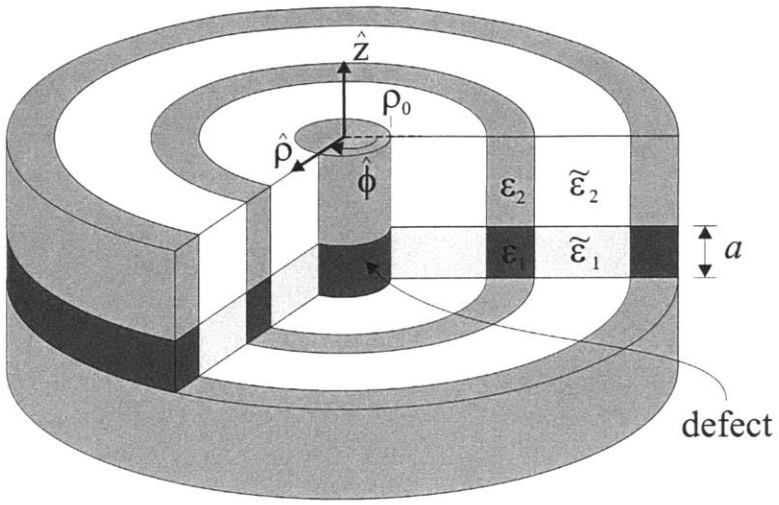

Figure A-5: Schematic of a three-dimensional Fabry-Perot cavity consisting of alternating index-guided slab waveguides stacked in the r direction with core/cladding indices n_1/n_2 and $\tilde{n}_1/\tilde{n}_2$, where the core (seen in cutaway at top) has thickness a. When the indices satisfy Eq. (A.2), the TE_{01} mode does not radiate at the waveguide interfaces.

of the same type, we use indices of $n_{\text{eff}} \cong 2.8141$ and $\tilde{n}_{\text{eff}} \cong 1.7086$ to form our Bragg layer pairs. Doing so, ensures that if we again choose a layer thickness corresponding to $a/\lambda = 0.2839$ and indices of $n_1 = 3$, $n_2 = \sqrt{6}$, $\tilde{n}_1 = 2$, and $\tilde{n}_2$ which satisfy Eq. (A.2) to form our three-dimensional resonator, we should obtain the same field distributions and $Q's$ for each, confirming the absence of radiation in the three-dimensional structure.

Top and cross-sectional views of the H_z field of an $N = 8$ three-dimensional cavity are depicted in Fig. A-6. The figure clearly demonstrates the ability of the cavity to confine the field. The only radiation emanates from the sides of the cavity as a result of the finite number of radial layers. In Fig. A-7 the cavity Q of two and three dimensional cavities are compared as a function of the number of layer pairs. The agreement between the two cases is remarkable with both exhibiting overlapping exponentially increasing $Q's$ with the number of layer pairs N.

A.3 Summary

We have shown that by satisfying a simple condition on the dielectric and by employing pure TE modes, resonant cavities with *arbitrary* Q and small (bounded) modal volume can be constructed in both two and three dimensions without a complete photonic bandgap.

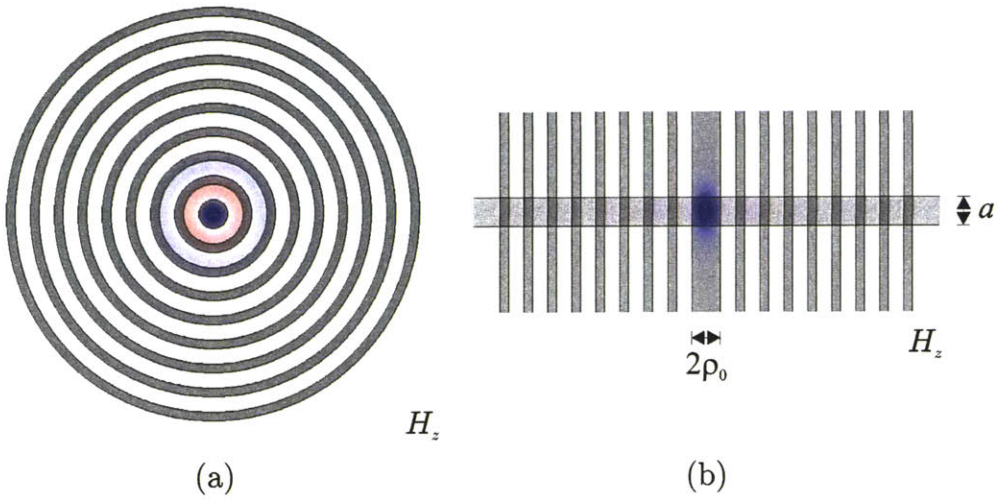

Figure A-6: (a) Horizontal and (b) vertical slices of the H_z field of the TE resonant mode shown in blue/red for negative/positive of a resonator of the type depicted in Fig. A-5. The dielectric ϵ is shown in grayscale and the cavity consists of alternating index-guided waveguides with core/cladding indices n_1/n_2 and $\tilde{n}_1/\tilde{n}_2$, where the core has width a and the indices satisfy Eq. (A.2), which ensures zero radiation losses at the waveguide interfaces.

Moreover, we have demonstrated both axial and radial cavity designs based on a standard quarter-wave stacks with a central quarter-wave defect, exhibiting Q's of over 10^5 with modest system sizes. The Q's of such cavities are limited by the system size (*e.g.* N and T, above), the degree to which Eq. (A.2) on ϵ can be satisfied, material absorption, surface roughness, and other disorder.

More complicated mirror structures (*e.g.* non-quarter wave shifted) and/or multiple defect sites may be used to tailor the transmission and dispersion characteristics of a cavity. In practice, in order to relax the material constraints, one may combine our mode-matching technique with some other strategy for increasing Q, such as one based on mode delocalization, or perhaps by using mode-matching in one dimension and two-dimensional photonic bandgap confinement in the others.

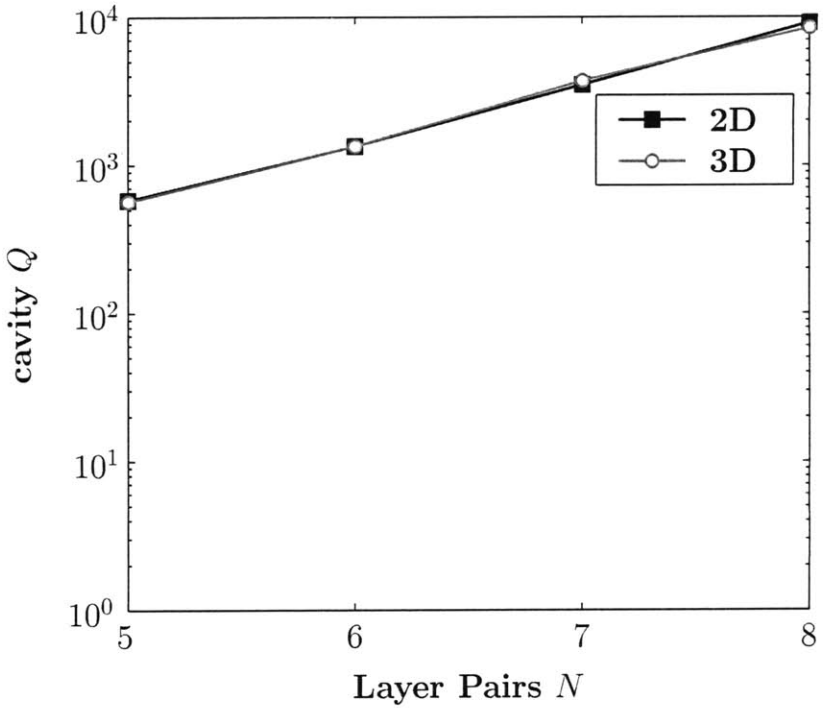

Figure A-7: Comparison of the cavity Q vs. the number of layer pairs N for two and three dimensional radially confining cavities. The two-dimensional structure was carefully chosen to have the same layer indices as the effective indices in the 3D structure.

Appendix B

Simulation Techniques

In this thesis, three simulation techniques, Finite-difference time-domain (FDTD), eigenmode expansion (EME), and finite-difference modesolvers (FDMS), were used to design optical components. Herein, we present a brief overview of each of these techniques and provide references for more detailed explanations.

B.1 The Finite Difference Time Domain Technique

A complete description of the FDTD technique is presented in the book by A. Taflove [21]. The bare essentials of the approach are reviewed here for completeness. The FDTD technique represents a discretized implementation of Maxwell's equations with no inherent accuracy limitations or need for root searching algorithms. The fields are updated in time rather than space and N-dimensional grids are required for N-dimensional problems. The computational grid is arranged such that the divergence operations $\nabla \cdot \mathbf{D} = \rho$ and $\nabla \cdot \mathbf{B} = 0$ are naturally maintained. Additionally, the electric and magnetic field components are offset from one another by 1/2 a grid point so as to enable second order accuracy in the derivatives of Maxwell's equations. As an example of how the Maxwell's equations are discretized, consider Maxwell's equation for the E_z field component in a dielectric.

$$\frac{\partial}{\partial t} E_z = \frac{1}{\varepsilon} \left[\frac{\partial}{\partial x} H_y - \frac{\partial}{\partial y} H_x \right] \tag{B.1}$$

For use in FDTD, equation (B.1) is discretized by central differences in both time and space.

$$\frac{E_z|_{i,j,k}^{n+1} - E_z|_{i,j,k}^{n}}{\Delta t} = \frac{1}{\varepsilon_{i,j,k}} \left(\begin{array}{l} \frac{H_x|_{i,j+1/2,k}^{n+1/2} - H_x|_{i,j-1/2,k}^{n+1/2}}{\Delta y} \\ + \frac{H_y|_{i+1/2,j,k}^{n+1/2} - H_y|_{i-1/2,j,k}^{n+1/2}}{\Delta x} \end{array} \right) \tag{B.2}$$

The rest of the field components are found similarly, such that the updated fields become

$$H_x|_{i,j,k}^{n+1/2} = H_x|_{i,j,k}^{n-1/2} + \frac{\Delta t}{\mu_{i,j,k}} \left(\begin{array}{l} \frac{E_y|_{i,j,k+1/2}^{n} - E_y|_{i,j,k-1/2}^{n}}{\Delta z} \\ + \frac{E_z|_{i,j+1/2,k}^{n} - E_z|_{i,j-1/2,k}^{n}}{\Delta y} \end{array} \right) \tag{B.3a}$$

$$H_y|_{i,j,k}^{n+1/2} = H_y|_{i,j,k}^{n-1/2} + \frac{\Delta t}{\mu_{i,j,k}} \left(\begin{array}{l} \frac{E_x|_{i,j,k+1/2}^{n} - E_x|_{i,j,k-1/2}^{n}}{\Delta z} \\ + \frac{E_z|_{i+1/2,j,k}^{n} - E_z|_{i-1/2,j,k}^{n}}{\Delta x} \end{array} \right) \tag{B.3b}$$

$$H_z|_{i,j,k}^{n+1/2} = H_z|_{i,j,k}^{n-1/2} + \frac{\Delta t}{\mu_{i,j,k}} \left(\begin{array}{l} \frac{E_x|_{i,j+1/2,k}^{n} - E_x|_{i,j-1/2,k}^{n}}{\Delta y} \\ + \frac{E_y|_{i+1/2,j,k}^{n} - E_y|_{i-1/2,j,k}^{n}}{\Delta x} \end{array} \right) \tag{B.3c}$$

$$E_x|_{i,j,k}^{n+1} = E_x|_{i,j,k}^{n} + \frac{\Delta t}{\varepsilon_{i,j,k}} \left(\begin{array}{l} \frac{H_y|_{i,j,k+1/2}^{n+1/2} - H_y|_{i,j,k-1/2}^{n+1/2}}{\Delta z} \\ + \frac{H_z|_{i,j+1/2,k}^{n+1/2} - H_z|_{i,j-1/2,k}^{n+1/2}}{\Delta y} \end{array} \right) \tag{B.3d}$$

$$E_y|_{i,j,k}^{n+1} = E_y|_{i,j,k}^{n} + \frac{\Delta t}{\varepsilon_{i,j,k}} \left(\begin{array}{l} \frac{H_x|_{i,j,k+1/2}^{n+1/2} - H_x|_{i,j,k-1/2}^{n}}{\Delta z} \\ + \frac{H_z|_{i+1/2,j,k}^{n+1/2} - H_z|_{i-1/2,j,k}^{n+1/2}}{\Delta x} \end{array} \right) \tag{B.3e}$$

$$E_z|_{i,j,k}^{n+1} = E_z|_{i,j,k}^{n} + \frac{\Delta t}{\varepsilon_{i,j,k}} \left(\begin{array}{l} \frac{H_x|_{i,j+1/2,k}^{n+1/2} - H_x|_{i,j-1/2,k}^{n+1/2}}{\Delta y} \\ + \frac{H_y|_{i+1/2,j,k}^{n+1/2} - H_y|_{i-1/2,j,k}^{n+1/2}}{\Delta x} \end{array} \right) \tag{B.3f}$$

where i, j, and k refer to the x, y and z grid points and n refers to the current time step.

As might be expected, as the discretizations in space and time approach zero, the algorithm becomes exact. However, clearly the use of finely spaced grid points increases the number of calculations required to update the field. Therefore, it is important to choose a fine, but not overly fine grid spacing. Taflove demonstrates that accurate results can be obtained with a spatial discretization of $\lambda/20$. The time step is then chosen to be close to $\Delta t = \Delta x/\left(c\sqrt{3}\right)$, which Taflove refers to as the *magic time step* because numerical dispersion goes to zero for this value of Δt. Yet, this value of Δt also represents the upper bound for stable operation of the algorithm. For time steps greater than the magic time step, the field grows without bound. And, for time steps less than the magic time step, numerical dispersion creeps into the propagating field. It is therefore desirable to choose

a time step that is close to, but slightly less than the magic time step. A time step of $\Delta t = \Delta x/(2c)$ is generally sufficient.

The purpose of a FDTD simulation is often to determine the coupling from a given input mode to a given output mode of interest. The coupling is also generally a function of frequency. To determine this frequency dependent coupling, a discrete Fourier transform (B.4) is taken across both the input and output cross-sections

$$\mathbf{E}(x,y,z,\omega) = \frac{1}{T}\sum_{n}\mathbf{E}(x,y,z)\exp\left(-j\omega t_n\right)\delta t \tag{B.4}$$

where $\mathbf{E}$ is the vector electric field, δt is the time discretization, t_n is time step n, and T is the period of integration. Although only the electric field is shown, the DFT is applied to both the electric and magnetic fields. To isolate the modes, the full electric and magnetic field distributions can be written in terms of a summation over the guided and radiation modes of the guide cross-section. Doing so, we write the electric and magnetic fields as

$$\mathbf{E}(x,y,z,\omega) = \sum_{m}\left(a_m(z,\omega) + b_m(z,\omega)\right)\mathbf{e}_m(x,y,\omega) \tag{B.5a}$$

$$\mathbf{H}(x,y,z,\omega) = \sum_{m}\left(a_m(z,\omega) - b_m(z,\omega)\right)\mathbf{h}_m(x,y,\omega) \tag{B.5b}$$

where a_m and b_m are the forward and backward mode amplitude coefficients and the $\mathbf{e}_m$ and $\mathbf{h}_m$ are the vector modal electric and magnetic fields, respectively, of mode m. Applying the well know orthogonality relation for power normalized modes (B.6)

$$\delta_{mn} = \frac{1}{2}\int \mathbf{e}_m \times \mathbf{h}_n \cdot \hat{\mathbf{z}}dA \tag{B.6}$$

to (B.5) and (B.5) we arrive at the following set of equations

$$j_n = \frac{1}{2}\int \mathbf{E}\times\mathbf{h}_n\cdot\hat{\mathbf{z}}dA = a_n(z,\omega) + b_n(z,\omega) \tag{B.7a}$$

$$v_n = \frac{1}{2}\int \mathbf{e}_n\times\mathbf{H}\cdot\hat{\mathbf{z}}dA = a_n(z,\omega) - b_n(z,\omega) \tag{B.7b}$$

which can be added and subtracted to obtain the transmission T_{kl}

$$T_{kl}(\omega) = \left| \frac{j_l(L,\omega) + v_l(L,\omega)}{j_k(0,\omega) + v_k(0,\omega)} \right|^2 \tag{B.8}$$

and reflection coefficients R_{kl}

$$R_{kl}(\omega) = \left| \frac{j_l(0,\omega) - v_l(0,\omega)}{j_k(0,\omega) + v_k(0,\omega)} \right|^2 \tag{B.9}$$

as a function of frequency. As a matter of practical concern, to obtain a sufficiently broadband response, a short pulse must be launched at the input. As a check for of the validaty of this approach, we compared the results of a problem with an exact solution to the results obtained from this FDTD approach. It turns out that the results of Appendix A are useful for this purpose. In Appendix A, we showed that a junction formed from cylindrical waveguide sections satisfying (A.2) and excited by pure TE modes have field solutions completely described by the input and output guided modes. As a result their transmission and reflection coefficients are determined entirely from their effective indices. Thus, we consider a junction formed from a pair of such waveguide sections (Fig. B-1), with $a = 0.5\,\mu$m, $n_1 = 2$, $n_2 = 1$, $\tilde{n}_1 = \sqrt{6}$, and $\tilde{n}_2 = \sqrt{3}$. The effective indices of the modes were calculated using a finite-difference modesolver to be $n_{eff} = 1.401$ and $\tilde{n}_{eff} = 1.995$ at $\lambda = 1.55\,\mu$m and so the power reflection coefficient should be $R = 0.0297$. From the FDTD simulation, we also find a reflection coefficients of $R_{FDTD} = 0.0297$.

B.2 Eigenmode Expansion

While FDTD provides extremely reliable results, the large grid sizes often required, can make FDTD impractical for a large class of devices. This is particularly true for adiabatic or slowly varying structures. Alternatively, optical waveguides can be modeled in the frequency domain. Eigenmode expansion (EME) represents one frequency domain approach that can, in some cases, provide highly accurate results. EME uses modal decomposition to represent the electromagnetic fields. Here we provide just a brief overview of the technique noting that a complete description of the EME approach is provided by P. Bienstman in his doctoral thesis [22].

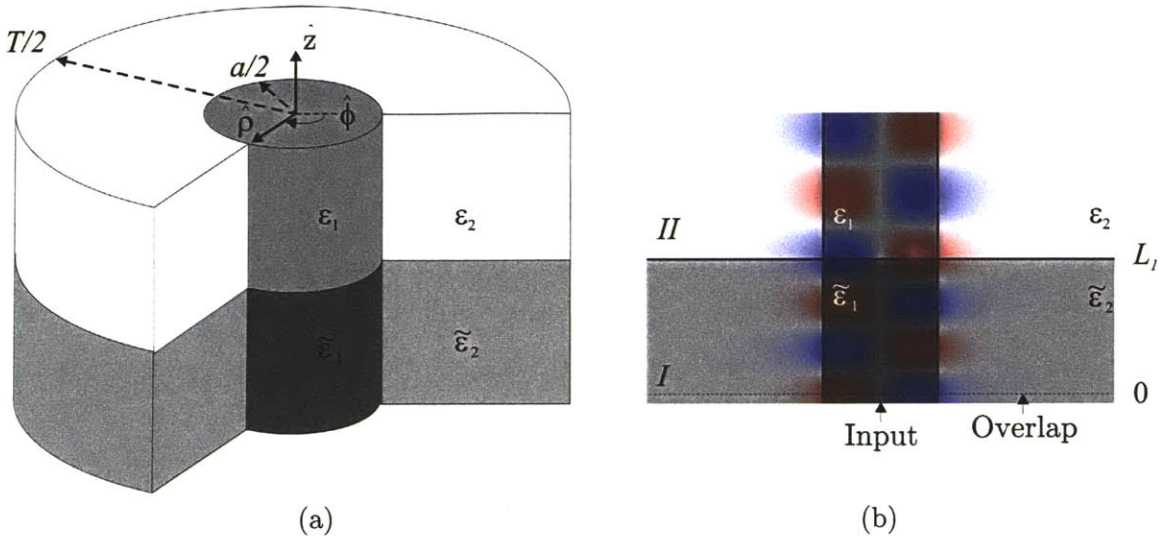

Figure B-1: (a) Radiation-free junction formed by a pair of cylindrical waveguide sections and (b) E_y field obtained from the FDTD simulation used to determine the reflection and transmission coefficients for a TE_{01} mode incident on the boundary formed by the cylindrical waveguide sections shown in (a).

In general the fields are represented as follows,

$$\mathbf{E}(x,y,z,\omega) = \sum_m a_m e^{j\beta_m z}\mathbf{e}_m(x,y,\omega) \tag{B.10a}$$

$$\mathbf{H}(x,y,z,\omega) = \sum_m a_m e^{j\beta_m z}\mathbf{h}_m(x,y,\omega) \tag{B.10b}$$

where the a_m are the amplitude coefficients, β_m the propagation constant, and $\mathbf{e}_m$ and $\mathbf{h}_m$ the modal vector electric and magnetic fields of mode m. Eigenmode expansion propagates the modes from one boundary to another. As an example, consider the following input field with one initially excited mode.

$$\mathbf{E}(x,y,z,\omega) = \sum_m a_m e^{j\beta_m z}\mathbf{e}_m^I(x,y,\omega) \tag{B.11a}$$

$$\mathbf{H}(x,y,z,\omega) = \sum_m a_m e^{j\beta_m z}\mathbf{h}_m^I(x,y,\omega) \tag{B.11b}$$

where the superscript I is used to indicate the fields being in Region I. If we suppose the field has propagated a distance L_1 where it is now incident upon an interface, as in Fig. B-1, the transmitted and reflected fields are then determined by matching boundary conditions

to get

$$a_m \mathbf{e}_{m,t}^{(I)} e^{j\beta_m L_1} + \sum_n R_{mn} a_m e^{j\beta_m L_1} \mathbf{e}_{n,t}^{(I)} = \sum_n T_{mn} a_m e^{j\beta_m L_1} \mathbf{e}_{n,t}^{(II)} \tag{B.12a}$$

$$a_m \mathbf{h}_{m,t}^{(I)} e^{j\beta_m L_1} - \sum_n R_{mn} a_m e^{j\beta_m L_1} \mathbf{h}_{n,t}^{(I)} = \sum_n T_{mn} a_m e^{j\beta_m L_1} \mathbf{h}_{n,t}^{(II)} \tag{B.12b}$$

Taking the cross products $\times \mathbf{h}_p^{(I)}$ and $\mathbf{e}_p^{(I)} \times$, respectively and using orthogonality (B.6), we get

$$\delta_{mp} + R_{mp} e^{j\beta_p L_1} = \sum_n T_{mn} \int \mathbf{e}_n^{(II)} \times \mathbf{h}_p^{(I)} \cdot \hat{\mathbf{z}} dA \tag{B.13a}$$

$$\delta_{mp} - R_{mp} e^{j\beta_p L_1} = \sum_n T_{mn} \int \mathbf{e}_p^{(I)} \times \mathbf{h}_n^{(II)} \cdot \hat{\mathbf{z}} dA \tag{B.13b}$$

Adding and subtracting the above equations yields the system of $N \times N$ linear equations (B.2)

$$\delta_{mp} = \frac{1}{2} \sum_n T_{mn} \left[\int \mathbf{e}_n^{(II)} \times \mathbf{h}_p^{(I)} \cdot \hat{\mathbf{z}} dA + \int \mathbf{e}_p^{(I)} \times \mathbf{h}_n^{(II)} \cdot \mathbf{z} dA \right] \tag{B.14a}$$

$$R_{mp} = \frac{1}{2} \sum_n T_{mn} \left[\int \mathbf{e}_n^{(II)} \times \mathbf{h}_p^{(I)} \cdot \hat{\mathbf{z}} dA - \int \mathbf{e}_p^{(I)} \times \mathbf{h}_n^{(II)} \cdot \hat{\mathbf{z}} dA \right] \tag{B.14b}$$

which can be solved using standard numerical root finding algorithms.

B.3 Finite-Difference Modesolver

Finite-difference modesolvers are especially convenient as they are easy to implement, reasonably fast, and very stable. Much work has been done in this area [11, 20]. Here, we provide just a basic overview of the problem. The eigenmodes of a waveguide are the solutions to the vector wave equation (B.3) for the waveguide geometry.

$$\nabla \times \nabla \times \mathbf{E} - \omega^2 \mu \epsilon \mathbf{E} = \nabla(\nabla \cdot \mathbf{E}) - \nabla^2 \mathbf{E} - \omega^2 \mu \epsilon \mathbf{E} = 0 \tag{B.15}$$

Generally, the solutions consist of the eigenvalue, namely the propagation constant β_m and the field distributions $\mathbf{e}_m$ and $\mathbf{h}_m$ where m denotes the mode number. The transverse electric field components are sufficient to fully define the field solution since the longitudinal electric field component can be derived from Gauss' Law ($\nabla \cdot \epsilon \mathbf{E} = 0$). The transverse wave

equation can be extracted from (B.3) and written with only the transverse components by using Gauss' Law to re-express the longitudinal component in terms of the transverse field. Doing so,

$$\frac{\partial}{\partial_z} E_z = -\frac{1}{\epsilon} \nabla_T \cdot \mathbf{E} \tag{B.16}$$

and inserting the result (B.16) into (B.3) we arrive at

$$\nabla_T (\nabla_T \cdot \mathbf{E}_T - \frac{1}{\epsilon} \nabla_T \cdot \epsilon \mathbf{E}_T) - \nabla_T^2 \mathbf{E_T} - \omega^2 \mu \epsilon \mathbf{E_T} = -\beta^2 \mathbf{E_T} \tag{B.17}$$

Since analytic solutions to (B.17) do not generally exist, (B.17) is applied using central differences across the computational domain. The result is a matrix eigenvalue problem of the form $\mathbf{E}_T \beta^2 = \mathbf{M E_T}$where β^2 is the eigenvalue and $\mathbf{M}$, the matrix operator applied to the field. This type of problem can be solved in a variety of ways using, for example, using the Arnoldi process in a software distribution called ARPACK. As a practical matter, the boundary conditions of the computational domain are most easily defined to be perfect conductors.

Bibliography

[1] B. E. Little, "A vlsi photonics platform," *Optical Fiber Comm. Conf. on CD-ROM (Optical Society of America, Washington, DC)*, vol. 2, pp. 444–445, 2004.

[2] C. K. Madsen, "Optical all-pass filters for polarization mode dispersion compensation," *Opt. Lett.*, vol. 25, pp. 878–880, 2000.

[3] M. R. Watts, *MS Thesis, Wavelength switching and routing through evanescently induced absorption.* Cambridge, MA: Massachusetts Institute of Technology, 2001.

[4] E. Snitzer, H. Po, F. Hakimi, R. Tumminelli, and B. C. McCollum, "Ultimate low-loss single mode fiber at 1.55μm," *Technol. Digest of OFC'88*, pp. 447–450, 1988.

[5] G. Charlet, E. Corbel, J. Lazaro, A. Klekamp, R. Dischler, P. Tran, W. Idler, H. Mardoyan, A. Konczykowska, F. Jorge, and S. Bigo, "Wdm transmission at 6-tbit/s capacity over transatlantic distance, using 42.7-gb/s differential phase-shift keying without pulse carver," *J. Lightwave Tech.*, vol. 23, pp. 104–107, 2005.

[6] M. P. Earnshaw, A. Griffin, C. Bolle, and J. B. D. Soole, "Reconfigurable optical add-drop multiplexer (roadm) with integrated sub-band optical cross-connect," *Optical Fiber Comm. Conf. on CD-ROM (Optical Society of America, Washington, DC)*, 2005.

[7] M. R. Watts, S. G. Johnson, H. A. Haus, and J. D. Joannopoulos, "Electromagnetic cavity with arbitrary q and small modal volume without a complete photonic bandgap," *Opt. Lett.*, vol. 27, pp. 1785–1787, 2002.

[8] M. J. Khan, M. Lim, C. Joyner, T. Murphy, H. A. Haus, and H. I. Smith, "Integrated bragg grating structures," *Digest of the LEOS Summer Topical Meetings*, pp. 7–8, 2001.

[9] T. Yanagase, S. Suzuki, Y. Kokubun, and S. T. Chu, "Box-like filter response and expansion of fsr by a vertically triple coupled microring resonator filter," *J. Lightwave Tech.*, vol. 20, pp. 1525–1529, 2002.

[10] P. P. Absil, S. T. Chu, D. Gill, J. V. Hryniewicz, F. Johnson, O. King, B. E. Little, F. Seiferth, and V. Van, "Very high order integrated optical filters," *Optical Fiber Comm. Conf. on CD-ROM (Optical Society of America, Washington, DC)*, 2004.

[11] M. Popovic, "Complex-frequency leaky mode computations using pml boundary layers," *Integrated Photonics Research (Trends in Optics and Photonics Series)*, vol. 91, pp. 143–145, 2003.

[12] J. Z. Huang, R. Scarmozzino, G. Nagy, M. J. Steel, and R. M. Osgood, "Realization of a compact and single-mode optica passive polarization converter," *IEEE Photon. Technol. Lett.*, vol. 12, pp. 317–319, 2000.

[13] V. P. Tzolov and M. Fontaine, "Passive polarization converter free of longitudinally periodic structure," *Opt. Commun.*, vol. 127, pp. 7–13, 1996.

[14] W. W. Lui, T. Hirono, K. Yokayama, and W. P. Huang., "Polarization rotation in semiconductor bending waveguides," *J. Lightwave Tech.*, vol. 16, pp. 929–936, 1998.

[15] M. R. Watts, H. A. Haus, G. Gorni, and M. Cherchi, "Integrated mode-evolution-based polariztion rotators," *Proc. Integrated Photonics Research Conference 2003*, pp. 26–28, 2003.

[16] M. R. Watts and H. A. Haus, "Integrated mode-evolution-based polarization rotators," *Opt. Lett.*, vol. 30, pp. 138–140, 2005.

[17] L. Pavesi and D. J. Lockwood, Eds., *Silicon Photonics.* Heidelberg, Germany: Springer-Verlag, 2004.

[18] K. Vahala, Ed., *Optical Microcavities.* Hackensack, NJ: World Scientific, 2004.

[19] A. W. Snyder, *Optical Waveguide Theory.* New York, NY: Chapman and Hall, 1983.

[20] W. C. Chew, "Electromagnetic theory on a lattice," *J. Appl. Phys.*, vol. 75, pp. 4843–4850, 1994.

[21] A. Taflove, *Computational Electromagnetics: The Finite-Difference Time-Domain Method.* Norwood, MA: Artech House, 1995.

[22] P. Bienstman, *PhD Thesis, Rigorous and efficient modelling of wavelength scale photonic components.* Ghent, Belgium: University of Ghent, 2001.

[23] Fimmwave by Photon Design.

[24] N. Goto and G. L. Yip, "A te-tm mode splitter in linbo$_3$ by proton exchange and ti diffusion," *J. Lightwave Tech.*, vol. 7, pp. 1567–1574, 1989.

[25] Y. Shani, C. H. Henry, R. C. Kistler, and K. J. Kazarinov, R. F.and Orlowsky, "Integrated optic adiabatic polarization splitter on silicon," *Appl. Phys. Lett.*, vol. 56, pp. 120–121, 1990.

[26] J. J. G. M. van der Tol and J. H. Laarhuis, "A polarization splitter on linbo$_3$ using only titanium diffusion," *J. Lightwave Tech.*, vol. 9, pp. 879–886, 1991.

[27] R. M. de Ridder, A. F. M. Sander, A. Driessen, and J. H. J. Fluitman, "An integrated optic adiabatic te/tm mode splitter on silicon," *J. Lightwave Tech.*, vol. 11, pp. 1806–1811, 1993.

[28] S. M. Garner, V. Chuyanov, S.-S. Lee, A. Chen, W. H. Steier, and L. R. Dalton, "Vertically integrated waveguide polarization splitters using polmers," *IEEE Photon. Technol. Lett.*, vol. 11, pp. 842–844, 1999.

[29] M. R. Watts, H. A. Haus, and E. P. Ippen, "Integrated mode-evolution-based polarization splitters," *Opt. Lett.*, vol. 30, pp. 967–969, 2005.

[30] K. Kasaya, O. Mitomi, M. Naganuma, Y. Kondo, and Y. Noguchi, "A simple laterally tapered waveguide for low-loss coupling to single-mode fibers," *IEEE Photon. Technol. Lett.*, 1993.

[31] M. R. Watts, M. Qi, T. Barwicz, P. T. Socci, L. Rakich, E. P. Ippen, H. I. Smith, and H. A. Haus, "Towards integrated polarization diversity: design, fabrication, and characterization of integrated polarization splitters and rotators," *Optical Fiber Comm. Conf. on CD-ROM (Optical Society of America, Washington, DC)*, 2005.

[32] G. Barbarossa and A. M. Matteo, "Novel double-ring optical-guided-wave vernier resonator," *IEE Proc.-Optoelectron*, vol. 144, pp. 203–208, 1997.

[33] S. I. Hidayat, Y. Toyota, O. Torigoe, O. Wada, and R. Koga, "Multipath structure for fsr expansion in waveguide-based optical ring resonator," *Electronics Letters*, vol. 39, pp. 366–367, 2003.

[34] T. Barwicz, M. Popovic, P. T. Rakich, M. R. Watts, H. A. Haus, E. P. Ippen, and H. I. Smith, "Fabrication and analysis of add/drop filters based on microring resonators in sin," *Optical Fiber Comm. Conf. on CD-ROM (Optical Society of America, Washington, DC)*, 2004.

[35] T. Barwicz, M. A. Popovic, P. T. Rakich, M. R. Watts, H. A. Haus, E. P. Ippen, and H. I. Smith, "Microring-resonator-based add-drop filters in sin: fabrication and analysis," *Opt. Express*, vol. 12, pp. 1437–1442, 2004.

[36] M. A. Popovic, M. R. Watts, T. Barwicz, P. T. Rakich, L. Socci, E. P. Ippen, F. X. Krtner, and H. I. Smith, "High-index-contrast, wide-fsr microring-resonator filter design and realization with frequency-shift compensation," *Optical Fiber Comm. Conf. on CD-ROM (Optical Society of America, Washington, DC)*, 2004.

[37] M. A. Popovic, T. Barwicz, M. R. Watts, P. T. Rakich, L. Socci, E. P. Ippen, F. X. Kaertner, and H. I. Smith, "Multistage high-order microring-resonator filters with relaxed tolerances for high through-port extinction," *Conference on Lasers and Electro-Optics (CLEO)*, 2005.

[38] M. R. Watts, T. Barwicz, M. Popovic, P. T. Rakich, L. Socci, E. P. Ippen, H. I. Smith, and F. X. Kaertner, "Microring-resonator filter with doubled free-spectral-range by two-point coupling," *Conference on Lasers and Electro-Optics (CLEO)*, 2005.

[39] H. A. Haus, *Waves and fields in optoelectronics.* Englewood Cliffs, NJ: Prentice-Hall, 1984.

[40] B. E. Little, S. T. Chu, H. A. Haus, J. Foresi, and J. P. Laine, "Microring resonator channel dropping filters," *J. Lightwave Tech.*, vol. 15, pp. 998–1005, 1997.

[41] C. Manolatou, M. A. Popovic, P. T. Rakich, T. Barwicz, H. A. Haus, and E. P. Ippen, "Spectral anomalies due to coupling-induced frequency shifts in dielectric coupled-resonator filters," *Optical Fiber Comm. Conf. on CD-ROM (Optical Society of America, Washington, DC)*, 2004.

[42] S. G. Johnson, S. Fan, A. Mekis, and J. D. Joannopoulos, "Multipole-cancellation mechanism for high-q cavities in the absence of a complete photonic band gap," *Appl. Phys. Lett.*, vol. 78, no. 22, pp. 3388–3390, 2001.

[43] J. D. Joannopoulos, R. D. Meade, and J. N. Winn, *Photonic Crystals: Molding the Flow of Light.* Princeton, 1995.

[44] P. R. Villeneuve, S. Fan, and J. D. Joannopoulos, "Microcavities in photonic crystals: Mode symmetry, tunability, and coupling efficiency," *Phys. Rev. B*, vol. 54, pp. 7837–7842, 1996.

[45] B. E. A. Saleh and M. C. Teich, *Fundamentals of Photonics.* Wiley, New York 1991.

[46] P. R. Villeneuve, S. Fan, S. G. Johnson, and J. D. Joannopoulos, "Three-dimensional photon confinement in photonic crystals of low-dimensional periodicity," *IEE Proc. Optoelec.*, vol. 145, no. 6, pp. 384–390, 1998.

[47] H. Benisty, D. Labilloy, C. Weisbuch, C. J. M. Smith, T. F. Krauss, D. Cassagne, A. Béraud, and C. Jouanin, "Radiation losses of waveguide-based two-dimensional photonic crystals: Positive role of the substrate," *Appl. Phys. Lett.*, vol. 76, no. 5, pp. 532–534, 2000.

[48] S. G. Johnson, A. Mekis, S. Fan, and J. D. Joannopoulos, "Molding the flow of light," *Computing Sci. Eng.*, vol. 3, no. 6, pp. 38–47, 2001.

[49] J. Vučković, M. Lončar, H. Mabuchi, and A. Scherer, "Design of photonic crystal microcavities for cavity qed," *Phys. Rev. E*, vol. 65, p. 016608, 2002.

[50] J. Čtyroký, "Photonic bandgap structures in planar waveguides," *J. Opt. Soc. Am. A*, vol. 18, no. 2, pp. 435–441, 2001.

[51] P. Yeh, *Optical Waves in Layered Media.* New York: Wiley, 1988.

[52] E. M. Purcell, "Spontaneous emission probabilities at radio frequencies," *Phys. Rev. B*, vol. 69, pp. 681–686, 1946.

[53] R. Coccioli, M. Boroditsky, K. W. Kim, Y. Rahmat-Samii, and E. Yablonovitch, "Smallest possible electromagnetic mode volume in a dielectric cavity," *IEE Proc. Optoelec.*, vol. 145, no. 6, pp. 391–397, 1998.